

UNCLASSIFIED

AD NUMBER
ADB067868
NEW LIMITATION CHANGE
TO Approved for public release, distribution unlimited
FROM Distribution authorized to U.S. Gov't. agencies only; Test and Evaluation; DEC 1981. Other requests shall be referred to Air Force Avionics Laboratory , ATTN; AFWAL?AWA, Wright-Patterson AFB. OH 45433.
AUTHORITY
AFWAL ltr, 21 Jan 1983

THIS PAGE IS UNCLASSIFIED

THIS REPORT HAS BEEN DELIMITED  
AND CLEARED FOR PUBLIC RELEASE  
UNDER DOD DIRECTIVE 5200.20 AND  
NO RESTRICTIONS ARE IMPOSED UPON  
ITS USE AND DISCLOSURE,

DISTRIBUTION STATEMENT A

APPROVED FOR PUBLIC RELEASE;  
DISTRIBUTION UNLIMITED.

2

7

AFWAL-TR-81-1280

AB067868



EXTINCTION OF CO<sub>2</sub> LASER RADIATION UNDER  
ADVERSE WEATHER CONDITIONS

Dr. Vincent Chimelis  
Electro-Optics Branch  
Mission Avionics Division

June 1982

Final Report for Period October 1978 to September 1981

SUBJECT TO EXPORT CONTROL LAWS

This document contains information for manufacturing or using munitions of war. Export of the information contained herein, or release to foreign nationals within the United States, without first obtaining an export license, is a violation of the International Traffic-in-Arms Regulations. Such violation is subject to a penalty of up to 2 years imprisonment and a fine of \$100,000 under 22 USC 2778.

Include this notice with any reproduced portion of this document.

DTIC  
SELECTED  
SEP 27 1982  
S H D

DTIC FILE COPY

Distribution limited to U.S. Government only; test and evaluation; Dec 81. Other requests for this document must be referred to the Avionics Laboratory (AFWAL/AWA), Wright-Patterson Air Force Base, Ohio 45433.

AVIONICS LABORATORY  
AIR FORCE WRIGHT AERONAUTICAL LABORATORIES  
AIR FORCE SYSTEMS COMMAND  
WRIGHT-PATTERSON AIR FORCE BASE, OHIO 45433

22 61 1280

NOTICE

When Government drawings, specifications, or other data are used for any purpose other than in connection with a definitely related Government procurement operation, the United States Government thereby incurs no responsibility nor any obligation whatsoever; and the fact that the Government may have formulated, furnished, or in any way supplied the said drawings, specifications, or other data, is not to be regarded by implication or otherwise as in any manner licensing the holder or any other person or corporation, or conveying any rights or permission to manufacturer, use, or sell any patented invention that may in any way be related thereto.

This technical report has been reviewed and is approved for publication.

*Vincent Chimelis*

Vincent Chimelis  
Project Engineer

*Harold E. Geltmacher*

Harold E. Geltmacher  
Supervisor

FOR THE COMMANDER

*Robert L. Johnson*

ROBERT L. JOHNSON Maj, USAF  
Deputy Chief, Electro-Optics Branch  
Mission Avionics Division  
Avionics Laboratory

Copies of this report should not be returned unless return is required by security considerations, contractual obligations, or notice on a specific document.

UNCLASSIFIED

SECURITY CLASSIFICATION OF THIS PAGE (When Data Entered)

REPORT DOCUMENTATION PAGE		READ INSTRUCTIONS BEFORE COMPLETING FORM
1 REPORT NUMBER AFWAL-TR-81-1280	2 GOVT ACCESSION NO <b>AD-B067 868L</b>	3 RECIPIENT'S CATALOG NUMBER
4 TITLE (and Subtitle) EXTINCTION OF CO <sub>2</sub> LASER RADIATION UNDER ADVERSE WEATHER CONDITIONS		5 TYPE OF REPORT & PERIOD COVERED FINAL Oct 78 Oct 81
		6 PERFORMING ORG NUMBER
7. AUTHOR(s) Dr. Vincent Chimelis		8 CONTRACT OR GRANT NUMBER(s)
9 PERFORMING ORGANIZATION NAME AND ADDRESS Air Force Avionics Laboratory (AARI) AF Wright Aeronautical Laboratories, AFSC Wright-Patterson Air Force Base, OH 45433		10 PROGRAM ELEMENT, PROJECT, TASK AREA & WORK UNIT NUMBERS 62204F Project 2004, Task 200405 Work Unit 20040547
11 CONTROLLING OFFICE NAME AND ADDRESS Air Force Avionics Laboratory (AARI) AF Wright Aeronautical Laboratories, AFSC Wright-Patterson Air Force Base, OH 45433		12 REPORT DATE June 1982
14 MONITORING AGENCY NAME & ADDRESS (if different from Controlling Office)		13 NUMBER OF PAGES 149
		15. SECURITY CLASS (of this report) UNCLASSIFIED
15a DECLASSIFICATION DOWNGRADING SCHEDULE		
16 DISTRIBUTION STATEMENT (of this Report) Distribution limited to U.S. Government only; test and evaluation; Dec 81. Other requests for this document must be referred to the Avionics Laboratory (AFWAL/AWA), Wright-Patterson Air Force Base, OH 45433.		
17 DISTRIBUTION STATEMENT (of the abstract entered in Block 20, if different from Report)		
18 SUPPLEMENTARY NOTES		
19 KEY WORDS (Continue on reverse side if necessary and identify by block number) Laser Propagation            Rain Laser Extinction            CO <sub>2</sub> Lasers Adverse Weather Aerosols		
20 ABSTRACT (Continue on reverse side if necessary and identify by block number) Results of extinction measurements of CO <sub>2</sub> laser radiation under adverse weather are presented. Data on eight different lines has been collected using a phase lock receiver with an aperture three times the beam diameter. The system dynamic range of 72 dBs is limited by the use of pyroelectric detectors. It was found that during dense fog measurements, the extinction encountered exceeded the dynamic range of the system more than 50% of the time. (Cont'd)		

~~UNCLASSIFIED~~

SECURITY CLASSIFICATION OF THIS PAGE (When Data Entered)

20. Reported measurements include extinction as a function of wavelength, time, and atmospheric particulates. Experimental measurements in fogs with extinction ranging from 1 to 72 dB/km, in rain with extinction ranging from 2 to 17 dB/km, and in light snow with extinction ranging from 3 to 14 dB/km are reported. Particle size data for over 150 fog size distributions have been collected. Measurements show that transmission losses in dense fog can easily be six orders of magnitude greater than losses in heavy rain. Results indicate that extinction of CO<sub>2</sub> laser radiation in adverse weather is at best, a very weak function of wavelength.

UNCLASSIFIED

SECURITY CLASSIFICATION OF THIS PAGE (When Data Entered)

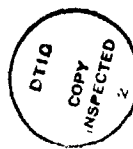
FOREWORD

This report covers an in-house research effort conducted by personnel of the Electro-Optics Branch (AARI), Mission Avionics Division (AAR), Avionics Laboratory, Air Force Wright Aeronautical Laboratories, Wright-Patterson Air Force Base, Ohio, under Project 2004, "Technology for Reconnaissance and Targeting," Task 200405, "Targeting Systems Characterization Facility," Work Unit 20040547, "Laser Atmospheric Transmission Measurements."

The work reported herein was performed during the period 1 October 1978 to 15 August 1981; Dr. Vincent Chimelis was the principal investigator. The report was released by the author 7 December 1981.

The author gratefully acknowledges the help of Mr. Jeff Sweet, Airman Russell Campbell, and Mr. Richard Norris for their help with the computer programs; Lt. Dave Rardin, and Maria Concha who operated the laser transmitter; and Sgt. Douglas Redmond who collected the raw particle size data. Finally, the author would like to acknowledge the help received from his advisor, Dr. Donald E. Lewis.

The material contained in this report is also used as a dissertation submitted to the Department of Electrical Engineering, The University of Dayton as partial fulfillment for the Degree of Philosophy.



Accession For	
NTIS GRA&I	<input checked="" type="checkbox"/>
DTIC TAB	<input type="checkbox"/>
Unannounced	
Justification	
By	
Distribution/	
Availability Codes	
Avail and/or	
Special	
Dist	
<b>B</b>	

## TABLE OF CONTENTS

SECTION	PAGE
I INTRODUCTION	1
II MOLECULAR SPECTRA	4
1. Molecular Vibrations	7
2. Molecular Rotation	12
a. Linear Molecules	13
b. Asymmetric Top Molecules	20
3. Rotation-Vibration Spectra	21
a. CO <sub>2</sub> Molecule	25
b. H <sub>2</sub> O Molecule	27
4. Spectra Perturbations	28
III MOLECULAR EXTINCTION	31
1. Introduction	31
2. Molecular Absorption	31
3. Line Shapes	33
a. Natural Linewidth	34
b. Collision Broadening	34
c. Doppler Broadening	35
4. Wing Theory	36
5. Transmission Models	38
IV AEROSOL EXTINCTION	40
1. Introduction	40
2. Aerosol Properties	44
3. Size Distribution	45
a. Continental Aerosols	45
b. Fog Particles	46
c. Precipitation	48
d. Snow	52

## TABLE OF CONTENTS (Cont'd)

SECTION		PAGE
V	SYSTEM ANALYSIS AND DESIGN	54
	1. Introduction	54
	2. Atmospheric Turbulence	54
	a. Beam Dancing	56
	b. Beam Spreading	57
	c. Scintillation	58
	d. Beam Steering	59
	e. Image Blurring	59
	3. System Design	60
	a. Gaussian Optics	60
	b. Laser Transmissometer	61
	4. Measurement Errors	68
VI	DISCUSSION OF RESULTS	69
	1. Introduction	69
	2. Clear Weather	69
	3. Fog	73
	4. Rain	94
	5. Haze	106
	6. Snow	121
VII	CONCLUSIONS	122
APPENDIX A.	CORRECTION FACTORS TO THE Van de Hulst APPROXIMATIONS TO THE MIE EXTINCTION FORMULAE	125
APPENDIX B.	CONVERSION OF EXTINCTION UNITS FROM $\text{km}^{-1}$ to dB/km	129
APPENDIX C.	TEST SITE	131
REFERENCES		133

## LIST OF ILLUSTRATIONS

FIGURE		PAGE
1	Rigid Rotator	14
2	Vibrational-Rotational Transitions with P, Q, and R Branches Illustrated	24
3	Fundamental Modes of Vibration of the CO <sub>2</sub> Molecule	26
4	Fundamental Modes of Vibration of the H <sub>2</sub> O Molecule	27
5	Doppler and Lorentz Spectral Line Shapes for Similar Intensities and Line Widths	37
6	Size Distribution for Fog Model	49
7	Comparison of the Marshall-Palmer Distribution (Solid Lines) and Observed Results of Laws and Parsons (Broken Lines) for Rain Rates of 1, 5, and 10 mm/hr. Adapted from Battan, Reference 38, p. 41	52
8	Projection of a Diffracted Laser Beam Due to Turbulent Eddies	55
9	Propagation of a Collimated Gaussian Beam	62
10	Optical Layout of Laser Transmitter	63
11	CO <sub>2</sub> Laser Transmissometer	64
12	Particle Size Distribution for Light Fog, 20 January 1981	74
13	Particle Size Distribution for Light Fog, 23 January 1981	75
14	Particle Size Distribution for Light Fog, 17 February 1981	76
15	Particle Size Distribution for Dense Fog, 18 February 1981	83
16	Particle Size Distribution for Dense Fog, 18 February 1981, 0630-0850 hrs	84
17	Particle Size Distribution for Medium Density Fog, 18 February 1981, 0715 hrs	87
18	Particle Size Distributions for Dense Fog, 19 February 1981, 0455-0510 hrs	92

## LIST OF ILLUSTRATIONS (Cont'd)

FIGURE		PAGE
19	Particle Size Distributions for Dense Fog, 19 February 1981, 0545-0605 hrs	93
20	Particle Size Distributions for Dense Fog, 19 February 1981, 0620-0640 hrs	96
21	Particle Size Distributions for Extremely Dense Fog, 19 February 1981, 0720-0750 hrs	97
22	Particle Size Distributions for Selected Fogs, 19 February 1981, 0805-0820 hrs	98
23	CO <sub>2</sub> Laser Extinction as a Function of Precipitation Rate for 10.6 $\mu$ m Laser Radiation, 22 April 1981	101
24	CO <sub>2</sub> Laser Extinction as a Function of Precipitation Rate for 10.6 $\mu$ m Laser Radiation, 28 April 1981	102
25	CO <sub>2</sub> Laser Extinction as a Function of Precipitation Rate for 10.6 $\mu$ m Laser Radiation, 29 April 1981	103
26	Extinction of CO <sub>2</sub> Laser Radiation as a Function of Precipitation Rate. Data Includes all Data Points from Figures 23, 24, and 25	105
27	Best Fit Models for Data on Figure 26, Laws and Parsons as Reported by Chen, and Measurements Conducted by Rensch	110
28	Model Size Distribution for Atmospheric Aerosols, Adapted from Reference 27, p. 124	111
29	Aerosol Size Distributions, Hazy Weather, 27 July 1981	113
30	Aerosol Size Distributions, Hazy Weather, 5 August 1981	114
31	Plot of FASCODE Output for Weather Conditions of T = 22.75°C, Dew Point = 20.8°C, and Relative Humidity = 83.8%. The markers Indicate Values Measured Under Heavy Haze Conditions	120

## LIST OF TABLES

TABLE		PAGE
1	Comparison of Measured and Calculated Transmission for Clear Weather Conditions, 25 February 1981, 1300 Hrs	70
2	Comparison of Measured and Calculated Transmission for Clear Weather Conditions, 3 March 1981, 0830 Hrs	71
3	Comparison of Measured and Calculated Transmission for Clear, Humid, Summer Weather Conditions, 20 July 1981, 1300 Hrs	72
4	Measured and Calculated Transmission for Several CO <sub>2</sub> Laser Lines Under Light Fog Conditions, 20 January 1981, 1410 Hrs	77
5	Measured and Calculated Transmission for Several CO <sub>2</sub> Laser Lines, 23 January 1981, 0920 Hrs	78
6	Measured and Computed Extinction Values for Several Wavelengths Under Light Fog Conditions, 17 February 1981, 1440 Hrs	79
7	Extinction of 10.6 $\mu\text{m}$ CO <sub>2</sub> Laser Radiation Data Taken from 0605 to 0715, 18 February 1981	82
8	Extinction of CO <sub>2</sub> Laser Radiation in Medium Density Fog for Several Lines, 18 February 1981, 0650-0659 Hrs	85
9	Extinction of CO <sub>2</sub> Laser Radiation in Light Density Fog for Several Wavelengths, 18 February 1981, 0715-0716 Hrs	86
10	Measured Transmission and Extinction During Fog Lifting Period, 18 February 1981	88
11	Extinction of CO <sub>2</sub> Laser Radiation in Heavy Fog. Data Taken 19 February 1981	89
12	Extinction of CO <sub>2</sub> Laser Radiation in Heavy Fog, 19 February 1981	90
13	Extinction of 10.6 $\mu\text{m}$ CO <sub>2</sub> Laser Radiation in Heavy Fog, 19 February 1981	91

## LIST OF TABLES (Cont'd)

TABLE		PAGE
14	Extinction of CO <sub>2</sub> Laser Radiation in Heavy Fog for Several Wavelengths, 19 February 1981, 0545-0546	95
15	Extinction of 10.26 $\mu$ m Radiation with Time, 19 February 1981	99
16	Measured Transmission and Extinction for Several CO <sub>2</sub> Laser Lines in Medium Density Fog, 19 February 1981, 0811-0812 Hrs	100
17	Extinction of CO <sub>2</sub> Laser Lines for a Constant Rain Rate of 1.82 mm/Hr, 22 April 1981, 1935 Hrs	107
18	Extinction of Several CO <sub>2</sub> Laser Lines for Constant Rain Rates of 1.8, 8.5, and 12 mm/Hr, 29 April 1981	108
19	Comparison of Aerosol Extinction Having an Assumed Complex Index of H <sub>2</sub> O and an Assumed Complex Index of NaCl (Data taken 27 July 1981)	109
20	Comparison of Aerosol Extinction Having an Assumed Complex Index of H <sub>2</sub> O and an Assumed Complex Index of NaCl (Data Taken 7 August 1981)	112
21	Computation of Extinction for Particles of Radius r(I) and Density dN(r)/dr (5 August 1981)	116
22	Measured and Computed Transmission for Several CO <sub>2</sub> Laser Lines in Hot, Humid, Hazy Weather, 27 July 1981, 0940 Hrs	117
23	Measured and Computed Transmission for Several CO <sub>2</sub> Laser Lines in Hot, Humid, Hazy Weather, 5 August 1981, 0825 Hrs	118
24	Transmission in Snow for Several CO <sub>2</sub> Lines, Missing Data Due to the Inability to Obtain Stable Lines in the Short Time Required	119

## SUMMARY

Laser propagation through the atmosphere is severely limited by atmospheric effects such as fog and rain. Because of the high power achievable and convertness, CO<sub>2</sub> lasers are finding a multitude of uses in military applications such as target designators, beam riders, moving target indicators, terrain following, weapons delivery, and imaging. CO<sub>2</sub> lasers have also grown in importance in applications such as pollution monitoring, optical communications, and earth resources remote sensing. These applications require a detailed knowledge of CO<sub>2</sub> laser atmospheric extinction and its dependency upon relevant meteorological parameters associated with adverse weather phenomena.

A tunable CO<sub>2</sub> laser transmissometer with a 72 dB dynamic range was fabricated to measure the extinction of laser radiation under adverse weather conditions. Data on eight different lines has been collected using a phase-lock receiver with an optical aperture three times the beam diameter. The system dynamic range of 72 dB is limited by the use of pyroelectric detectors. It was found that during dense fog measurements, the extinction encountered exceeded the dynamic range of the system more than 50% of the time.

Reported measurements include extinction as a function of wavelength, time, and atmospheric particulates. Experimental measurements in fogs with extinction ranging from 1 to 72 dB/km, in rain with extinction ranging from 2 to 17 dB/km and in light snow with extinction ranging from 3 to 14 dB/km are reported. Particle size data for over 150 fog size distributions have been collected. Extinction by fog in excess of 290 dB/km was obtained from computed values of extinction cross-sections and measured size distributions. An empirical model was derived for CO<sub>2</sub> laser extinction as a function of precipitation rate. Depending on the refractive index, extinction by haze particulates may exceed 1.4 dB/km. Particles below 0.3  $\mu\text{m}$  radius do not contribute significantly to extinction, and unless the aerosol size distribution contains a significant number of particles larger than this size, aerosol extinction may be neglected.

AFWAL-TR-81-1280

Measurements show that transmission losses in dense fog can easily be six orders of magnitude greater than losses in heavy rain. Results indicate that extinction of CO<sub>2</sub> laser radiation in adverse weather is at best a very weak function of wavelength.

SECTION I  
INTRODUCTION

Laser propagation through the atmosphere is severely limited by atmosphere effects such as fog and rain. Because of the high power achievable and convertness, CO<sub>2</sub> lasers are finding a multitude of uses in military applications such as target designators, beam riders, moving target indicators, terrain following, weapons delivery, and imaging. CO<sub>2</sub> lasers have also grown in importance in applications such as pollution monitoring, optical communications, and earth resources remote sensing. These applications require a detailed knowledge of CO<sub>2</sub> laser atmospheric extinction and its dependency upon relevant meteorological parameters associated with adverse weather phenomena.

The object of this study is to investigate how atmospheric particulates, especially fog and rain, affect CO<sub>2</sub> laser propagation through the atmosphere.

Atmospheric particulates below 0.3 micrometer radius add little contribution to extinction at CO<sub>2</sub> wavelengths and generally can be ignored in computations. In dealing with hazy conditions, most of the aerosol contribution to extinction comes from particles in the size range 0.3 to 1.5  $\mu\text{m}$  radius, with smaller contributions extending to particles of radius up to 4  $\mu\text{m}$ . For typical summer weather under hazy conditions, molecular extinction due to the far wings of the water vapor lines predominate, with an approximate upper bound contribution to extinction of  $.34 \text{ km}^{-1}$  due to aerosols (this locality, Dayton, Ohio).

The fog measurements presented are backed-up by an extensive particle size data base. Computation of extinction by fog has been performed by direct laser measurements and by numerical integration of the extinction cross section and particle size distributions. The liquid water content for each distribution has been computed and this is used to obtain an approximation to the extinction which is then compared with the measurements. Extinction due to rain is presented as a function of rain rates

and a mathematical relationship is derived relating extinction to rain rates without the need for knowledge of rain drop size or drop terminal velocity.

The principles of molecular spectra are presented in Section II. The derivations and formalism covered are centered around the two main contributors to molecular extinction near the 10.6  $\mu\text{m}$  - the  $\text{H}_2\text{O}$  and  $\text{CO}_2$  molecules.

Molecular extinction is treated in Section III. Line intensity profiles and wing theory are treated, and an introduction to high resolution transmission models is presented.

Section IV discusses extinction by atmospheric particulates and precipitation. Various model distributions are presented. Exact Mie extinction formulas are introduced as well as the Deirmendjian approximations.

Atmospheric turbulence effects and how they affect system design are presented in Section V. Analysis of the laser transmissometer system is presented.

Section VI describes measurements and analyzes the results obtained for  $\text{CO}_2$  laser extinction in fog, rain, and haze.

The data collected for this study stretches over a three year period. This study depended on the ability to obtain the proper weather conditions of interest. Sometimes when the weather was right, the equipment was not ready; and when the equipment was ready, the weather was not right. Several fog measurements were obtained during the winter of 1979, but the particle counter data was suspect. Fall and winter of 1980 produced only one brief but unexpected fog. The results presented in this report are based on data collected within the last year, mostly because the year 1981 provided all the necessary adverse weather conditions of interest, and calibration of the meteorological instruments needed, achieved a good level of confidence which was absent in previous years.

Several difficulties were encountered during the course of this investigation (See Appendix C). Troubles with the laser were many. The two most persistent ones were the line selection mechanism and gas leakage from the plasma tube. The mechanical design for the grating drive made it impossible to maintain calibration on the laser for more than a few days. Gas leakage of the plasma tube resulted in the laser exploding on three different occasions. Because of the unreliability of the large tunable laser, a smaller single line laser was modified and fitted with a piezoelectric mounted mirror. This arrangement provided data on approximately ten lines, all of which were not available at all times. Where data on specific lines is absent, it is because the line could not be tuned in, or because it took longer than required for under conditions of the measurement.

In this report, extinction is defined as the loss of radiant flux (or power) along the direction of propagation due to the interaction of electromagnetic radiation and matter. As defined, it is the combined contribution of molecular and aerosol extinction. No effort is made to separate scattering effects from absorption effects. The extinction coefficient is the value of extinction as measured or computed at specific frequencies (or wavelengths) per unit path length.

SECTION II  
MOLECULAR SPECTRA

The extinction of an electromagnetic beam by an absorbing medium is a result of the interaction of the electromagnetic fields of the radiation with the molecular species in the absorbing medium. If the interaction results in the molecule taking energy from the field, absorption occurs. If the interaction results in the molecule giving energy to the field, emission occurs. The molecular species emit or absorb at specific frequencies which depend on their molecular structure. At the frequency, where a molecule emits or absorbs, it is said to have an absorption line. Thus an absorption (or emission) process results in an absorption spectrum composed of discrete lines, each corresponding to an energy state as prescribed by quantum mechanical principles. The absorption of energy occurs when the atomic system makes a transition between one stationary state of energy  $E'$  and another of energy  $E''$ , where by convention the lower of the two levels involved in a transition is indicated by a (") and the upper of the two levels will be indicated by a ('). The frequency at which the transition occurs is given by

$$\nu = \frac{E' - E''}{h} \quad (1)$$

where  $h$  is Planck's constant.

The appearance of a spectrum is connected with energy alterations in the molecular species which produce the spectrum. Molecules can uptake energy in four possible ways:

1. Electronic energy ( $E_e$ )
2. Vibrational energy ( $E_v$ )
3. Rotational energy ( $E_r$ )
4. Translational energy ( $E_t$ ).

The translational energy is not quantized and does not result in or influence spectra. The total energy which produces the spectrum is given by

$$E = E_e + E_v + E_r + E_i \quad (2)$$

where  $E_i$  is the interaction energy between the different energies in the molecule. Each of the energy states is described by certain quantum numbers, an alternation of which leads to a specific spectrum. As these spectra are found in different regions, the energy changes connected with the emission or absorption of radiation can be of different orders of magnitude. The largest energy values are found for the energies of electron promotion. The allowed electronic energy states are rather widely separated in energy, so that transitions between different energy levels correspond to transition frequencies which lie generally in the visible and ultra-violet portions of the spectra. These electronic bands play a very minor role in the transfer of radiation through the atmosphere and they are of no consequence when dealing with absorption spectra associated with  $\text{CO}_2$  infrared lasers.

Interpretation of the spectrum of a molecule requires a knowledge of the allowed energy states, allowed transitions, and of the transition probabilities, and how each of these depend on the molecular structure. To understand infrared spectra, one must know how vibrational and rotational motions of a molecule produce their associated energies. A complete treatment of molecular vibrations and rotations requires the application of quantum mechanics and group theory. These methods become cumbersome and impractical even for simple molecules. Knowledge of the molecular structure makes it possible to apply symmetry properties which allow some simplification in arriving at a solution. In general, the most common approach requires the separation of the rotational effects from the vibrational effects and neglecting the cross-coupling effects. Higher order approximations necessitate the inclusion of vibration interactions and rotation-vibration interactions, where the mathematical formulation has been made to agree with observed results.

A vibrating or rotating molecule cannot interact with electromagnetic radiation unless the vibration or rotation is accompanied by a dipole moment. An oscillating dipole must be present for coupling to occur between the energy of the molecule and the electric field so that energy can be exchanged between them. This restriction precludes all homonuclear diatomic molecules such as  $O_2$ ,  $H_2$ , and  $N_2$ , from possessing an infrared spectrum. Under normal conditions, their spectra can only be obtained in connection with electronic promotion. Therefore, in the study of  $CO_2$  laser propagation, it is found that  $CO_2$  and  $H_2O$  are the primary molecular absorbers in the lower atmosphere. In the discussion that follows, the vibrational and rotational energies of these two types of molecules will be derived, showing how they give rise to their absorption spectra.

For a molecule containing  $n$  atoms, the one-dimensional Schrödinger equation can be easily extended to describe the system under consideration. For a system of  $N$  particles, the wave equation is given by

$$\frac{-h^2}{8\pi^2} \sum_{i=1}^N \frac{1}{m_i} \nabla_i^2 \psi + V\psi = E\psi \quad (3)$$

where  $m_i$  is the  $i$ -th particle mass,  $E$  is the energy operator  $(-h/2\pi i) \partial/\partial t$ ,  $\nabla_i^2$  is the Laplacian for the  $i$ -th particle, and the wave function  $\psi = \psi(x_1, y_1, z_1, \dots, x_n, y_n, z_n)$  involves all  $3N$  cartesian coordinates. In general, three cartesian coordinates are required to describe the motion of the center of mass of a molecule. These are used to describe the vibrational modes of the molecule. Three more coordinates are required to describe the rotation of the system about the principal moments of inertia axis. Wilson, Decius, and Cross (Reference 1) have shown that the system can be treated separately for each set of coordinates, so that the vibrational motion can be separated from the rotational motion. If the interaction energy terms are neglected, the total wave function can be written as the product of a vibrational wave function  $\psi_V$  and a rotational wave function  $\psi_R$ , i.e.,

$$\Psi_R \cong \psi_V \psi_R$$

A molecular system composed of  $N$  atoms having  $3N$  coordinates possesses  $3N$  degrees of freedom. Those degrees of freedom include three that describe translational motion of the system as a whole. If one chooses the molecular center of gravity as the origin of the coordinate system, then the total number of coordinates is reduced by three, since  $3N-3$  coordinates are sufficient to determine the relative position of the atoms with respect to their center of gravity. Additionally, since the vibrational and rotational wave functions are separable, the number of coordinates is reduced by 3 for either a rotational or vibrational system. Therefore  $3N-6$  coordinates are needed for a description of a purely vibrational system or a purely rotational system. Due to symmetry considerations, a linear molecule has only two degrees of rotational freedom; therefore,  $3N-5$  degrees of freedom are required to describe a linear molecular system.

#### 1. MOLECULAR VIBRATIONS

The quantum mechanical calculation of the possible vibrational frequencies for a given molecular system starts with the solution to the wave Equation 3. In cartesian coordinates, the wave equation is

$$\frac{-h}{8\pi^2} \sum_{i=1}^N \frac{1}{m_i} \left( \frac{\partial^2 \psi}{\partial x_i^2} + \frac{\partial^2 \psi}{\partial y_i^2} + \frac{\partial^2 \psi}{\partial z_i^2} \right) + V(x_i, y_i, \dots, z_i) \psi = E\psi \quad (4)$$

where the position of each atom of mass  $m_i$  is described by the triplet  $(x_i, y_i, z_i)$ . The use of cartesian coordinates is not convenient for describing molecular motions and one resorts to the use of normal coordinates  $Q_k$ ,  $k = 1, 2, \dots, 3N$ , where the normal coordinates are defined in terms of the mass-weighted cartesian coordinates  $q_i$  by the linear transformation

$$Q_k = \sum_{i=1}^N l_{ki} q_i \quad k = 1, 2, \dots, 3N$$

Normal coordinates are such that both the kinetic and potential energies of a system are expressed by the sum of terms each involving the square of a normal coordinate. Pauling and Wilson (Reference 2) have shown that in terms of these normal coordinates the kinetic and potential energies are given by

$$T = \frac{1}{2} \sum_{k=1}^{3N} \dot{Q}_k^2 \quad (6)$$

$$V = \frac{1}{2} \sum_{k=1}^{3N} \lambda_k Q_k^2 \quad (7)$$

where  $Q_k = \sqrt{M_k} q_k \quad (8)$

$Q_k$  represents a change of scale of the general coordinates  $q_k$ ,  $q_k$  designates the position of  $k$ -th nucleus with respect to its equilibrium position,  $M_k$  is the mass of  $k$ -th nucleus, and  $\lambda_k$  are the constants related to the normal frequencies  $\lambda$ . In terms of the general cartesian coordinates the first term in Equation 4 can now be expressed by

$$\sum_{i=1}^N \frac{1}{M_i} \nabla^2_i \psi = \sum_{k=1}^{3N} \frac{1}{M_k} \frac{\partial^2 \psi}{\partial q_k^2}$$

By the change of coordinates of Equation 8

$$\frac{1}{M_k} \frac{\partial^2 \psi}{\partial q_k^2} \text{ becomes } \frac{\partial^2 \psi}{\partial Q_k^2}$$

and after employing Equation 3, the wave equation (Equation 4) can be written in the form

$$-\frac{\hbar^2}{8\pi^2} \sum_{k=1}^{3N} \frac{\partial^2 \psi}{\partial Q_k^2} + \frac{1}{2} \sum_{k=1}^{3N} \lambda_k Q_k^2 \psi = E\psi \quad (9)$$

Using the fact that for a purely vibrational system, the system can be entirely described by  $3N-6$  coordinates ( $3N-5$  for a linear system of atoms) and rearranging Equation 9, the vibrational wave equation becomes

$$\sum_{k=1}^{3N-6} \frac{\partial^2 \psi}{\partial Q_k^2} + \frac{8\pi^2}{\hbar^2} \left[ E - \frac{1}{2} \sum_{k=1}^{3N-6} \lambda_k Q_k^2 \right] \psi = 0 \quad (10)$$

Letting

$$\psi = \psi_1(Q_1)\psi_2(Q_2)\dots\psi_{3N-6}(Q_{3N-6}) \quad (11)$$

Equation 10 is now separable into  $3N-6$  equations, one for each normal coordinate  $Q_k$ , each one having the form

$$\frac{\partial^2 \psi_k}{\partial Q_k^2} + \frac{8\pi^2}{\hbar^2} (E_k - \frac{1}{2}\lambda_k Q_k^2) \psi_k = 0 \quad (12)$$

This is the one-dimensional equation for the simple harmonic oscillator. The solution  $\psi$  of the vibrational problem is therefore expressible as a product of  $3N-6$  harmonic oscillator functions  $\psi(Q_k)$ , while the vibrational energy  $E$  is the sum of the energies of  $3N-6$  harmonic oscillators, and is thus given by

$$E = E_1 + E_2 + \dots + E_{3N-6} \quad (13)$$

The energy levels of a linear harmonic oscillator are given by the well known relation

$$E = (v + \frac{1}{2})h\nu \quad v = 0, 1, 2, \dots \quad (14)$$

where  $v$  is the quantum number which can take on any positive integral value, while  $\nu$  is the classical frequency of the vibrating system and is related to the wavelength by the relation

$$\nu = \frac{\lambda}{2\pi} \quad (15)$$

Using Equation 14, the vibrational energy of a molecule with several classical frequencies  $\nu_k$  corresponding to the normal modes of vibration is given by

$$E(v) = \sum_{i=1}^M (v_i + \frac{1}{2})h\nu_i \quad (16)$$

where  $M$  is equal to  $3N-6$  or  $3N-5$  for the case of linear molecules. When two or more normal vibrations are equal, Equation 16 has to be modified to account for the degree of degeneracy ( $d_i$ ) and the result is given by

$$E(v) = \sum_{i=1}^M (v_i + d_i/2)h\nu_i \quad (17)$$

Where degenerate terms occur, the energy value will depend not on the individual values of  $v_i$  and  $\nu_k$  but on their sum. If both sides of Equation 17 are divided by  $hc$ , then the energy term is given

$$G(v) = \sum_{i=1}^M \omega_i (v_i + \frac{d_i}{2}) \quad (18)$$

where both  $G(v)$  and  $\omega_i$  have the wave number units of  $\text{cm}^{-1}$ .

Equation 18 gives a first order approximation to pure vibrational spectra. In the study of pure vibrational spectra of polyatomic molecules, it is found that in addition to the bands corresponding to the normal vibrations, there are bands of lower intensity present at approximate multiples of the normal frequencies. These overtones are the result of the anharmonicity of the vibrations.

When the classical harmonic oscillator is considered, the potential energy function is treated as having the form

$$V = gr^2 \quad (19)$$

Examination of the potential function for a molecular system shows that the potential energy curve is better approximated by the inclusion of cubic and quartic terms so that Equation 19 takes the form

$$V = gr^2 - hr^3 + Rr^4 - \dots \quad (20)$$

The consequence is that the vibrations are no longer harmonic in nature and the concept of normal vibrations is no longer rigorously possible. The influence of this anharmonicity shows up in the energy term as an interaction containing two or more quantum numbers in addition to terms containing single quantum numbers. Using perturbation methods, Nielsen (reference 3) arrived at the solution

$$\begin{aligned} \omega(v_1 v_2 v_3) = & \sum_i^3 \omega_i \left( v_i + \frac{d_i}{2} \right) + \sum_i^3 \sum_{k \geq 1}^3 x_{ik} \left( v_i + \frac{d_i}{2} \right) x \\ & \left( v_k + \frac{d_k}{2} \right) + \sum_i^3 \sum_{k \geq 1}^3 g_{ik} l_i l_k \quad (21) \end{aligned}$$

for molecules of the type  $XY_2$  having a two-fold degeneracy. The last quantity in the expression accounts for the fact that some energy levels are split by the action of anharmonicity,  $l_i$  being a new quantum number having the values  $l_i = v_i, v_i-2, v_i-4, \dots$  and  $g_{ik}$  is some constant depending on the geometry of the molecule. The vibration spectrum for the  $CO_2$  linear molecule can be obtained from Equation 21. For nondegenerate

molecules such as  $H_2O$ ,  $l_i = g_{ik} = 0$  and the vibrational spectra may be obtained from

$$G(v_1, v_2, v_3) = \sum_{i=1}^3 \omega_i \left(v_i + \frac{1}{2}\right) \sum_{i=1}^3 \sum_{k \neq i}^3 x_{ik} \times \left(v_i + \frac{1}{2}\right) \left(v_k + \frac{1}{2}\right) \quad (22)$$

The values of  $x_{ik}$  and  $g_{ik}$  have been computed for the  $CO_2$  molecule by Darling and Davidson (Reference 4). Similarly, values of  $x_{ik}$  for the  $H_2O$  molecule have been computed by Dennison (Reference 5).

## 2. MOLECULAR ROTATION

Solutions to the molecular rotation problem can be obtained by setting the Schrödinger wave equation in three dimensions and using polar coordinates. The straightforward solution becomes very complicated and to simplify the solution, one has to consider special cases using symmetry properties to the molecule. This results in solving the wave equation individually for classes of molecules that fit into certain symmetry groups and several solutions to the rotational wave equations are necessary. Realizing that in absorption spectra, the expression for the rotational energy states allowed are of prime importance, it is much simpler to resort to classical mechanics to obtain the desired energy states.

The rotation spectrum of a molecule is mainly determined by the magnitude of its moment of inertia. The atoms in the molecule are treated as point masses,  $m_i$ , so that the moment of inertia of the molecule (assuming a rigid system) is

$$I = \sum_{i=1}^N m_i r_i^2, \quad (23)$$

where  $r_i$  is the perpendicular distance of the  $i$ -th mass from the rotational axis. According to classical mechanics, the inertial behavior of such a body is completely defined by the moments of inertia about three mutually perpendicular axes. The corresponding moments of inertia are called the principal moments of inertia. To determine the main inertia axes, one must have the knowledge of the symmetry properties of the molecule. Axes of symmetry are always perpendicular to main inertia axes and planes of symmetry always perpendicular to main inertia axes. When dealing with atmospheric absorption at  $\text{CO}_2$  wavelengths, only two types of molecular symmetry need be considered. One is the linear molecule ( $\text{CO}_2$ ) and the other is the asymmetric top molecule ( $\text{H}_2\text{O}$ ).

a. Linear Molecule

In a linear molecule such as  $\text{CO}_2$  the molecular axis is the line joining the nuclei of the individual atoms. The moment of inertia about this molecular axis is in almost all cases neglected, being zero or very small in comparison with the other two equally large ones. In this case the model of the rigid rotator can be used together with a correction term for nonrigidity where applicable. The nonrigidity term is used to account for possible centrifugal distortion produced by rotation. The rigid rotator is illustrated in Figure 1, where the center of gravity is labeled CG,  $m_1$  and  $m_2$  are masses of rotator, and  $r_1$  and  $r_2$  the distances from the rotational axis. From Equation 23,

$$I = m_1 r_1^2 + m_2 r_2^2 \quad (24)$$

which reduces to the more common form

$$I = \mu r^2$$

where  $\mu = \frac{m_1 m_2}{m_1 + m_2}$  is the reduced mass.

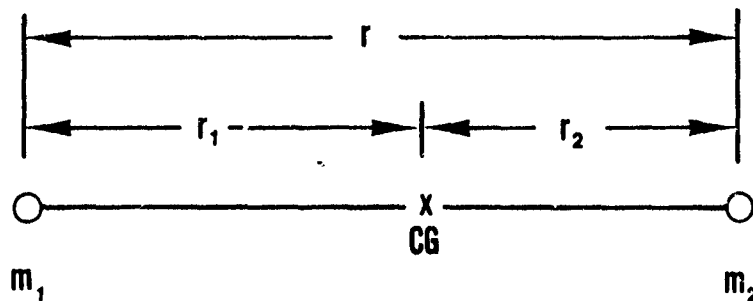


Figure 1. Rigid Rotator

The kinetic energy of a system of moving particles is given by

$$E = \frac{1}{2} \sum_i m_i v_i^2 \quad (26)$$

In terms of angular velocity  $w$ , the energy for the system of rotating particles is given by

$$\begin{aligned} E &= \frac{1}{2} \sum_{i=1}^N m_i w^2 r_i^2 \\ &= \frac{1}{2} w^2 \sum_{i=1}^N m_i r_i^2 \\ &= \frac{1}{2} I w^2 \end{aligned} \quad (27)$$

where the relationship  $v = wr$  has been used. The angular momentum of a rotating particle is given by  $mvr$ . For a system of particles the angular momentum is defined by

$$P = \sum_{i=1}^N m_i v_i r_i$$

which is easily regrouped into

$$P = \sum_{i=1}^N m_i r_i^2 \left( \frac{v_i}{r_i} \right) = I\omega \quad (28)$$

Bohr's theory requires that the quantized angular momentum be of the form

$$P = J \frac{h}{2\pi}, \quad J = 0, 1, 2, \dots \quad (29)$$

where  $J$  is the standard rotational quantum number. It has been shown in various textbooks (References 1,2) that in order to obtain results that agree with the solution of the results obtained from the Schrödinger wave equation, it is necessary to replace  $J$  by  $[J(J+1)]^{1/2}$  in Equation 29. In this case the correct quantized angular momentum is given by

$$P = \sqrt{J(J+1)}h/2\pi, \quad J = 0, 1, 2, \dots \quad (30)$$

The allowed rotational energies are obtained by substituting Equation 30 into Equation 27 and rearranging to give

$$E_R = \frac{1}{2I} J(J+1)(h/2\pi)^2 \quad (31)$$

From manipulation of Equation 1, it is seen that when energy is divided by  $hc$ , the resulting quantity has units of wave numbers ( $\text{cm}^{-1}$ ). This gives rise to the spectroscopic energy term  $F(J)$  expressed in the form

$$\begin{aligned} F(J) &= E_R/hc \\ &= (h/8\pi^2 cI) J(J+1) \\ &= BJ(J+1) \text{ cm}^{-1} \end{aligned} \quad (32)$$

where

$$B = h/8\pi^2 cI \text{ cm}^{-1} \quad (33)$$

is called the rotational constant. For absorption of radiation by a rotational energy transition to occur, the molecule must have a permanent dipole moment and there must be compliance with the selection rule  $\Delta J = +1$  ( $\Delta J = -1$  must be satisfied for emission). The wave number of the radiation absorbed by an alteration in the rotational quantum number is given by

$$\nu = F(J') - F(J'') \quad (34)$$

where  $J''$  is the quantum number corresponding to the lower energy state and  $J'$  is the quantum number corresponding to the higher energy state. Using Equation 32 one obtains

$$\begin{aligned} \nu &= B(J+1)(J+2) - BJ(J+1) \\ &= B(J^2+3J+2) - B(J^2+J) \\ &= 2B(J+1) \end{aligned} \quad (35)$$

Since the lower levels corresponding to  $J = 0, 1, 2, \dots$  are generally populated, absorption of radiation occurs at frequencies

$$\nu = 2nB, \quad n = 1, 2, 3, \dots \quad (36)$$

This equation indicates that the rotational spectrum observed for a linear molecule represented by the rigid rotator approximation is a set of lines spaced by the factor  $2B$ . In reality the molecules are not rigid but flexible and can be expected to stretch under the influence of centrifugal forces arising from their rotation. Thus, the length of the molecule and its moment of inertia  $I$ , would increase as the rotational energy increases causing  $B$  to decrease. The stretching of the molecule from a distance  $r_0$  to some new distance  $r$  from the point of rotation, gives rise to a potential energy of the form,

$$V = \frac{1}{2} kx^2 = \frac{1}{2} k(r-r_0)^2 \quad (37)$$

The rotational energy of the system is then given by the Hamiltonian for the system

$$\begin{aligned} E_R &= T + V \\ &= \frac{1}{2} I \omega^2 + \frac{1}{2} k (r - r_0)^2 \end{aligned} \quad (38)$$

Using Equations 25 and 28, the first term becomes  $P^2/2\mu r$  and Equation 38 can be expressed as

$$E_R = \frac{P^2}{2\mu r^2} + \frac{1}{2} k (r - r_0)^2 \quad (39)$$

It is now necessary to express the rotational energy  $E_r$  explicitly in terms of the distorted quantity  $r_0$ . According to basic mechanics, a rotating system of particles with reduced mass  $\mu$  and angular velocity  $\omega$ , experiences a centrifugal force  $\mu r \omega^2$  which is balanced by a restoring force  $f = kr$ , thus

$$k(r - r_0) = \mu r \omega^2 \quad (40)$$

$$r(k - \mu \omega^2) = k r_0$$

$$r^2 = \left( \frac{k r_0}{k - \mu \omega^2} \right)^2 \quad (41)$$

Substituting for  $r$  in the first term of Equation 39, one obtains

$$\begin{aligned} E_R &= \frac{P^2 (k - \mu \omega^2)^2}{2\mu k^2 r_0^2} + (k/2) (r - r_0)^2 \\ &= \frac{P^2}{2\mu r_0^2} \left( 1 - \frac{2\mu \omega^2}{k} + \frac{\mu^2 \omega^4}{k^2} \right) + (k/2) (r - r_0)^2 \end{aligned}$$

From  $(\mu w/k)^2 = (r-r_0/r)^2$ , the last term in the first parenthesis can be neglected and one has

$$\begin{aligned}
 E_R &= \frac{p^2}{2\mu r_0^2} - \frac{p^2 w^2}{kr_0^2} + (k/2)(r-r_0)^2 \\
 &= \frac{p^2}{2\mu r_0^2} - \frac{p^2 (r_0^2 w)^2}{k\mu^2 r_0^6} + (k/2)(r-r_0)^2 \\
 &= \frac{p^2}{2\mu r_0^2} - \frac{p^4}{k\mu^2 r_0^6} + (k/2)(r-r_0)^2 \quad (42)
 \end{aligned}$$

From Equation 40,

$$\begin{aligned}
 (k/2)(r-r_0)^2 &= \frac{(\mu r w^2)^2}{2k} \\
 &= \frac{(\mu^2 r^4 w^2)^2}{2k\mu^2 r^6} \\
 &= \frac{p^4}{2k\mu^2 r^6} \quad (43)
 \end{aligned}$$

Since the term  $k(r-r_0)^2/2$  is included to account for the molecular stretching it is very small in comparison to the kinetic energy term and  $r$  can be approximated by  $r_0$  in Equation 43. Thus, Equation 42 becomes

$$\begin{aligned}
 E_R &= \frac{p^2}{2\mu r_0^2} - \frac{p^4}{k\mu^2 r_0^6} + \frac{p^4}{2k\mu^2 r_0^6} \\
 &= \frac{p^2}{2\mu r_0^2} - \frac{p^4}{2k\mu^2 r_0^6} \quad (44)
 \end{aligned}$$

To convert the classical result to a quantum mechanical result, one proceeds as before using the rule that the angular momentum be quantized according to

$$P = \sqrt{J(J+1)} \quad h/2\pi$$

Substituting for P in Equation 44 results in the expression

$$E_R = \frac{h^2 J(J+1)}{8\pi^2 \mu r_0^2} - \frac{h^4 J^2 (J+1)^2}{32\pi^4 k r_0^6 \mu^2} \quad (45)$$

In terms of wave number units

$$F = \frac{E_R}{hc}$$

$$= \frac{h}{8\pi^2 I c} J(J+1) - \frac{h^3 \mu}{32\pi^4 I^3 k c} J^2 (J+1)^2 \quad (46)$$

Using Equation 33 and the relationship

$$w = (1/2\pi c) \sqrt{k/m}$$

Equation 46 becomes,

$$F(J) = BJ(J+1) - \frac{4B^3}{w^2} J^2 (J+1)^2$$

$$F(J) = BJ(J+1) - DJ^2 (J+1)^2 \quad (47)$$

where  $D = 4B^3/w^2$  is known as the rotational constant and is obtainable from spectral measurements. If one substitutes for h and c in Equation 32, B has the value

$$B = \frac{27.986}{I} \times 10^{-40}$$

Therefore, it is seen from Equation 47 that the correction term is very small and for low values of  $J$  the energy of rotation remains virtually unchanged. From Equation 34 the frequencies of the allowed transitions in wave numbers are

$$\begin{aligned}
 \nu &= F(J+1) - F(J) \\
 &= B[(J+1)(J+2) - J(J+1)] - \\
 &\quad D[(J+1)^2(J+2)^2 - J^2(J+1)^2] \\
 &= 2B(J+1) - 4D(J+1)^3 \qquad (49)
 \end{aligned}$$

This shows that the distance between successive rotational lines are no longer constant and decrease slightly with increasing values of  $J$ .

#### b. Asymmetric Top Molecules

Molecules which do not possess rotational axis higher than two-fold, are asymmetric tops and have the property of possessing three different principal moments of inertia. The total angular momentum  $P$  conforms to the basic rule that it remains constant in magnitude and direction during the rotational motion. However, there is no longer a direction in the molecule along which the total angular momentum has a constant component and there is no axis fixed to the molecule that carries out a simple rotation about  $P$ . Under these conditions, according to the laws of classical mechanics (or quantum mechanics), the energy levels of an asymmetric top molecule such as  $H_2O$  cannot be represented by explicit formulation. To arrive at a set of qualitative energy levels, one may treat the asymmetric top molecule in terms of two limiting cases of the much simpler symmetric top molecule. In this molecule, two of the principal moments of inertia are equal and denoted by  $I_B$  and the third by  $I_A$ . For an asymmetric top molecule,  $I_A \neq I_B \neq I_C$ , where  $I_A > I_B > I_C$ . By using the limiting case in which  $I_B$  is allowed to decrease gradually from  $I_B$  to  $I_C$ , and then to increase gradually to  $I_A$ , Herzberg has shown that one can obtain at best a rough approximation to the energy levels of an asymmetric top molecule. One of the more refined treatments for the energy formulation has been worked out by Wang (Reference 7). For the energy term, Wang gives

$$F(J_t) = \frac{1}{2}(B+C) J(J+1) + [A - \frac{1}{2}(B+C)]W_t \qquad (50)$$

where the subscript  $t$  is used to indicate that there are  $2J+1$  energy levels for each value of  $J$ .  $W_t$  is a quantity interrelated in a very complex way to the rotational constants  $A, B, C$  and the rotational quantum number  $J$ . Algebraic equations for the solution for  $W_t$  have been formulated and these can be found on pp. 46-47 of Reference 6.

### 3. ROTATION-VIBRATION SPECTRA

Pure vibration or pure rotation spectra for polyatomic molecules is seldom found in nature, particularly in the Earth's lower atmosphere. The spectra which occurs is the result of the simultaneous excitation of rotation and vibration commonly referred to as rotation-vibration spectra. For complicated molecules such as  $H_2O$ , no closed formulae exists as was explained in the previous section. However, mathematical relationships have been formulated to fit observed experimental results. This is particularly true of the  $H_2O$  molecule whose spectra has been measured extensively (References 3-5).

As a first approximation, the vibration-rotation energy term of a molecule is given by the sum of the individual vibrational and rotational terms,

$$\bar{\epsilon} = G(v) + F(J) \quad (51)$$

where  $G(v)$  and  $F(J)$  are given by Equations 22 and 50, respectively. The effect of the interaction can be accounted for by introducing the effects of vibration into the rotational constants  $A$  and  $D$ . The rotational constants are affected because the moment of inertia  $I$  changes during a vibration such that the average value of  $I/J$  in Equation 33 is not exactly the same as its value in the equilibrium position. For a linear molecule, the rotational constant  $B$  takes the form

$$B[v] = B_e - \sum_i \alpha_i \left( v_i + \frac{d_i}{2} \right) \quad (52)$$

where  $[v]$  denotes all the vibrational quantum numbers  $v_1, v_2, \dots$ , and  $e$  denotes the quantity at its equilibrium value.  $\alpha_i$  is a constant that accounts for the deviation of  $r$  from  $r_e$ , and the Coriolis interaction of rotation and vibration. The influence of the vibration term due to the action of the centrifugal force was accounted for in the rotational constant  $D$  introduced earlier in Equation 47. The influence of  $D$  will be different for the different vibrational levels and this is accounted for by substituting  $D[v]$  for  $D$ . Therefore, the rotational-vibrational energy for a linear molecule is given by

$$T = \sum_i w_i \left( v_i + \frac{d_i}{2} \right) + \sum_i \sum_k x_{ik} \left( v_i + \frac{d_i}{2} \right) \left( v_k + \frac{d_k}{2} \right) + g_{ii} l_i^2 + B[v] J(J+1) - D[v] J^2(J+1)^2 \quad (53)$$

For an asymmetric top molecule, the rotational constants  $A$ ,  $B$ , and  $C$  take the form

$$\begin{aligned} A[v] &= A_e - \sum_i \alpha_i^A \left( v_i + \frac{1}{2} \right) \\ B[v] &= B_e - \sum_i \alpha_i^B \left( v_i + \frac{1}{2} \right) \\ C[v] &= C_e - \sum_i \alpha_i^C \left( v_i + \frac{1}{2} \right) \end{aligned} \quad (54)$$

The complete rotational-vibrational term is then given by

$$T = G(v) + \frac{1}{2}(B[v] + C[v])J(J+1) + [A[v] - \frac{1}{2}(B[v] + C[v])]W_c \quad (55)$$

where

$$A_e = \frac{h}{8\pi^2 c I_A^e}, \quad B_e = \frac{h}{8\pi^2 c I_B^e}, \quad C_e = \frac{h}{8\pi^2 c I_C^e}$$

$G(\nu)$  is given by Equation 22, and  $e$  denotes the equilibrium value of the quantity.

The observation of infrared spectra must always be connected with an alteration of the dipole moment of the molecule undergoing a transition. This can be readily observed by taking a look at the matrix component  $M_{i,j}$  of the dipole moment given by

$$R_{i,j} = \int \psi_i \vec{M} \psi_j d\nu \quad (57)$$

where  $\psi_i$  and  $\psi_j$  are the wave functions for the indicated molecular states,  $\vec{M}$  is the dipole moment and the integration is over the entire configuration space. If  $\vec{M}$  is a constant, then Equation 11 becomes

$$R_{i,j} = \vec{M} \int \psi_i^* \psi_j d\nu \quad (58)$$

from the orthogonality conditions

$$\int \psi_i^* \psi_j d\nu = 0 \quad (i \neq j) \quad (59)$$

Equation 58 becomes

$$\vec{M} \int \psi_i^* \psi_j d\nu = 0 \quad (60)$$

which says that if the dipole moment  $M$  is constant, then the matrix component of the dipole is identically zero. If this is true, then the line intensity  $S_{i,j}$  (see Section III) will be zero and no spectra can be observed.

A vibration defines the coarse structure of the bands and a rotation defines the fine structure encountered. This can be seen from Equations 53 and 55. The term  $G(\nu)$  gives the band center and each vibrational level is seen to be accompanied by a series of rotational levels corresponding to the  $2J+1$  values of  $J$  in the equation. This is illustrated at the top of Figure 2.

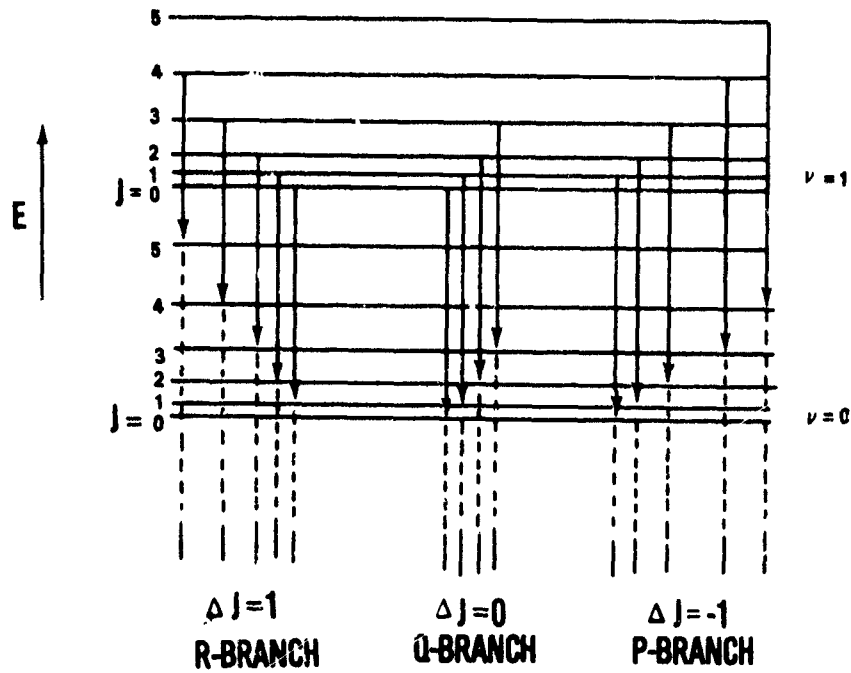
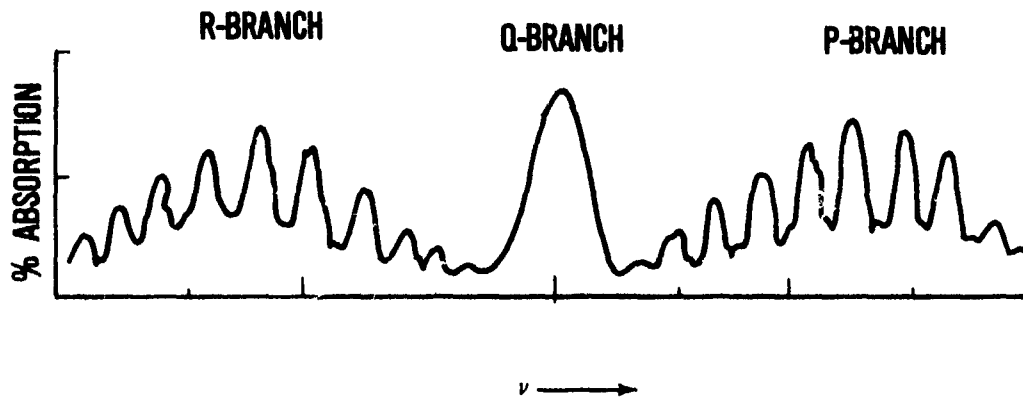


Figure 2. Vibrational-Rotational Transitions with P, Q, and R Branches Illustrated

In general, the interaction of vibration and rotation is not too large and the selection rules for the rotation-vibration spectrum are the same as for the individual vibration and rotation spectrum. Because of this interaction, the rotational selection rules are governed by the direction of change of the dipole moment during the vibration. A rigorous treatment of the selection rules involves usage of the symmetry properties and the rotational eigenfunction  $\psi_r$  for each class of molecules. Such a treatment has been performed for both the  $\text{CO}_2$  and  $\text{H}_2\text{O}$  molecules by Dennison (Reference 5) also see Herzberg (Reference 6 pp. 50-59 and pp. 468-487). A rotational level is called positive (+) or negative (-) depending on whether the rotational eigenfunction  $\psi_r$  remains unaltered (symmetric) or changes its sign (antisymmetric) by a reflection of all sets of particles at the origin. By convention, the symbol  $\leftrightarrow$  is used to indicate allowed combinations and  $\nleftrightarrow$  to indicate the contrary. Transitions between levels have to obey the selection rules

$$\text{a: } \Delta J = 0, \pm 1, \quad J = 0 \nleftrightarrow J = 0$$

$$\text{b: } + \leftrightarrow -, + \nleftrightarrow +, - \nleftrightarrow -$$

$$\text{c: } l = 0, \pm 1$$

Transitions for  $\Delta J = 0, +1$ , and  $-1$  correspond to Q, R, and P branches, respectively. The top of Figure 2 shows a simplified illustration of a vibrational-rotational transition band along with the appearance of the P, Q, and R branches. The Q branch lies at the band center with the P branch above the band center, and the R branch below the band center.

a.  $\text{CO}_2$  Molecule

Due to its linear symmetry, the  $\text{CO}_2$  molecule has four fundamental modes of vibration, two of which are degenerate. This is shown in Figure 3.

The first mode corresponding to  $\nu_1$  is classified as a symmetric stretching since the two oxygen atoms move away symmetrically from the carbon atom. Such a motion does not result in a change of the dipole moment and is not infrared active. The second motion resulting in  $\nu_2$  is classified as a bending mode and is infrared active. However, it is also

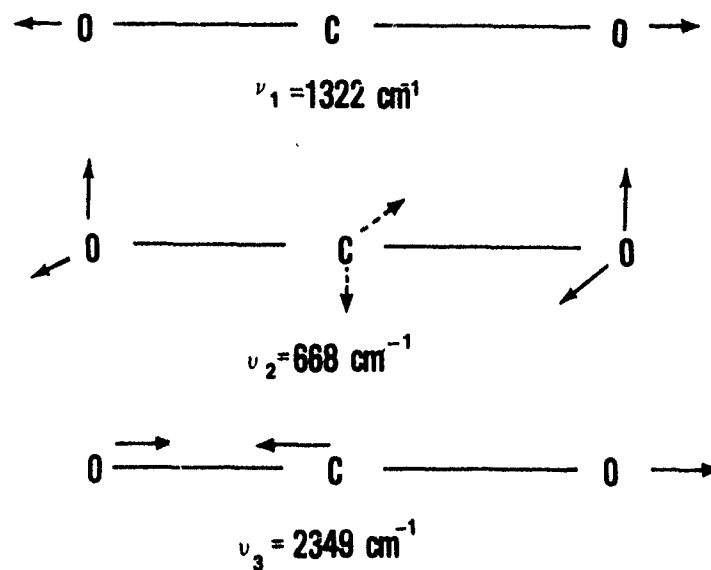


Figure 3. Fundamental Modes of Vibration of the  $\text{CO}_2$  Molecule

a degenerate mode since the molecule can vibrate with the same frequency in a plane perpendicular to the plane represented by the solid arrows. The third motion resulting in  $\nu_3$  is classified as a symmetric stretch which results in a change of the dipole moment and is infrared active. By convention, the asymmetric and symmetric stretching vibrations are described as parallel vibrations, where the change in dipole moment is parallel to the axis of symmetry of the molecule. The bending vibration is described as a perpendicular vibration since the change of dipole moment during the vibration is perpendicular to the major axis of symmetry.

The infrared spectrum of the  $\text{CO}_2$  molecule consists principally of two intense bands, one centering at  $667.38 \text{ cm}^{-1}$  and the other at  $2349.15 \text{ cm}^{-1}$ . In addition to these strong bands there exists a large number of weaker bands which are the result of overtones of the fundamentals and combinations of overtones and fundamentals. It is the overtone

$$2\nu_2 (\nu = 1388.18 \text{ cm}^{-1})$$

which combines with  $\nu_3$  to give the combination band ( $\nu_3 - 2\nu_2$ ). This band is centered at  $960.97 \text{ cm}^{-1}$  ( $10.41 \mu\text{m}$ ) and contains the  $\text{CO}_2$  laser lines of interest for the  $\text{C}^{12}\text{O}_2^{16}$  isotope.

b.  $\text{H}_2\text{O}$  Molecule

The  $\text{H}_2\text{O}$  molecule has three fundamental modes of vibration which are illustrated in Figure 4. The vibrational energy levels belong to one of two symmetry classes, depending on whether the upper energy state  $\nu_3$  is odd or even. Because of the closeness of  $\nu_1$  and  $\nu_3$ , vibration resonances do occur, but they are of different symmetry class and cannot interact directly; consequently, interaction is very weak. Infrared spectra has only been observed for  $\nu_2$  and  $\nu_3$ , thus the strong water vapor bands have centers at  $1595 \text{ cm}^{-1}$ ,  $3755.8 \text{ cm}^{-1}$ , and several of the overtones and combinations.

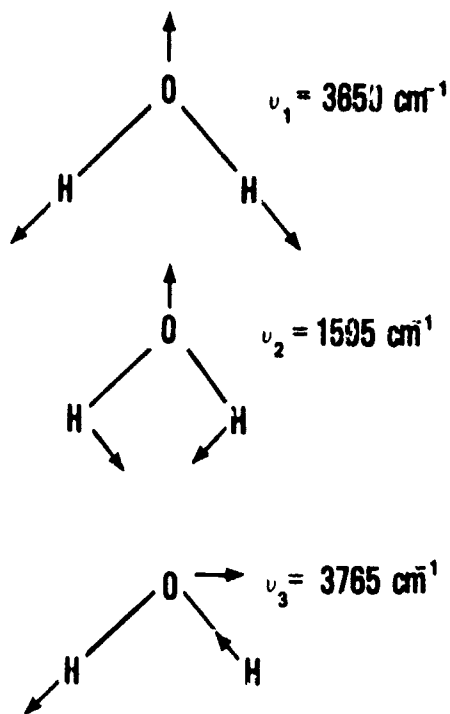


Figure 4. Fundamental Modes of Vibration of the  $\text{H}_2\text{O}$  Molecule

As was previously discussed, the asymmetric top molecule is characterized by the three unequal moments of inertia  $I_A$ ,  $I_B$ ,  $I_C$  where  $I_A < I_B < I_C$ . The three principal axis about which the moments  $I_A$ ,  $I_B$ , and  $I_C$  act are denoted a,b,c, respectively. The rotational eigenfunction  $\psi_R$  is a function of the orientation of this system of axis with respect to a fixed coordinate system. A condition imposed is that  $\psi_R$  must remain unchanged or only change sign for such a rotation. The rotations are labeled  $C_2^a$ ,  $C_2^b$ ,  $C_2^c$  where the subscript 2 denotes that the molecule belongs to the point group having a two-fold axis of symmetry and the superscript indicates the principal axis for the rotation operation. Accordingly, molecules belonging to this point group have three types of band contours called A, B, or C bands depending on whether the change in dipole moment is along the direction of least, intermediate, or largest principal moments of inertia. The  $H_2O$  molecule has its permanent dipole moment along the intermediate axis of the principal moment of inertia giving rise to spectra of type B bands. This band is characterized by the lack of a strong central branch, with the gap filled by weak lines and surrounded on both sides by strong groups of lines

For the frequencies of interest to  $CO_2$  laser propagation, the vibration bands do not contain the frequencies of  $CO_2$  laser emission. The extinction due to  $H_2O$  is directly attributable (except for the R 20 line at  $10.25 \mu m$ ) to the absorption of the water vapor continuum around  $10 \mu m$ . This continuum is attributed to be the result of the accumulated wings of the water vapor lines of the  $6.3 \mu m$  fundamental band and from the pure rotational lines above  $14 \mu m$ .

#### 4. SPECTRA PERTURBATIONS

There are two important factors which have an effect on the observed spectra. These are termed Coriolis interaction and Fermi resonance. The degree of interaction is a function of the frequency of the interacting levels, with the interaction being more pronounced for energy levels lying closely together.

The Coriolis interaction comes from the Coriolis force experienced by a rotating particle. When a Coriolis force component happens to line-up with the direction of vibration of the nuclei in the molecule, Coriolis interaction will result with some coupling of energy between the modes. The closer in frequency the vibrating modes, the higher the interaction between the energy levels.

The Coriolis effect is accounted for in the energy equation by the constant  $\alpha$  found in the rotational constant B of Equation 52, where  $\alpha$  is the sum of the harmonic and anharmonic components, and of the Coriolis interaction. The interaction is then accounted for by replacing  $\alpha$  in Equation 52 with

$$\alpha = \alpha^{\text{har}} + \alpha^{\text{anhar}} + \alpha^{\text{cor}}. \quad (61)$$

It is seen from the energy equation that the Coriolis interaction increases quadratically with J, such that for high values of J, the perturbation of the vibration levels become more significant where the frequency of the levels involved are spaced closely together. An example of the significance of this interaction is given by Meredith, et al. (Reference 8) in which they give results for line strengths measured in the  $10580 \text{ cm}^{-1}$  and  $10570 \text{ cm}^{-1}$  region. They found some line strengths which are 25 times stronger than predicted by line model calculations.

Fermi resonance may occur when two vibrational levels belonging to different vibrations (or combination of vibrations) have nearly the same energy. The occurrence of such a resonance interacts to cause a perturbation of the energy levels. For example, such a perturbation arises in the  $\text{CO}_2$  molecule for the state  $\nu_1 = 1337 \text{ cm}^{-1}$  and  $2\nu_3 = 1334 \text{ cm}^{-1}$ . The interaction causes one of the levels to be shifted up and the other down so that the separation of the levels is larger than predicted, and Equation 53 no longer allows for an accurate prediction of the energy in this case.

For the rotating-vibrating molecule, the Fermi resonance will, in general, produce a change in the effective rotational constants  $B$  of the two interacting levels. Correction to the energy term can be accomplished by introducing a correction to the rotational constant. Adel and Dennison (Reference 9) have formulated such a correction. In terms of the unperturbed rotational constants  $B_{v_j}^0$  and  $B_{v_i}^0$  for the levels  $v_i$  and  $v_j$ , the effective rotational constants  $B_{v_j}$  are

$$\begin{aligned} B_{v_j} &= a^2 B_{v_j}^0 + b^2 B_{v_i}^0 \\ B_{v_i} &= b^2 B_{v_j}^0 + a^2 B_{v_i}^0 \end{aligned} \quad (62)$$

where  $a$  and  $b$  are fractional constants obeying the rule  $a^2 + b^2 = 1$ . A different technique in use to account for the Fermi interaction is given in Reference 10. This is based on the addition of the extra term  $H_v J^3(J+1)^3$  to the energy equation, where  $H_v$  is a constant determined from the rotational constants.

SECTION III  
MOLECULAR EXTINCTION

1. INTRODUCTION

The amount of radiation propagated between any two points in the atmosphere is determined by the two principle types of constituents, namely gaseous molecules and aerosols. For a homogeneous optical path of length  $R$  having an attenuation coefficient  $\sigma_\lambda$  for monochromatic radiation of wavelength  $\lambda$ , the atmospheric transmittance is given by

$$T_\lambda = \exp(-\sigma_\lambda R) \quad (63)$$

where the attenuation coefficient  $\sigma_\lambda$  is the sum of the absorption ( $k$ ) and scattering ( $\alpha$ ) coefficients of the molecules and aerosols encountered in the propagation path. Thus, the extinction coefficient is the sum of the four components,

$$\sigma_\lambda = k_m + \alpha_m + k_a + \alpha_a \quad (64)$$

where the subscript  $m$  refers to molecular and  $a$  refers to aerosols. Each of these coefficients is wavelength dependent. In addition, the scattering coefficient is highly dependent on the size of the scatterer in relation to the wavelength. For the  $\text{CO}_2$  infrared wavelengths of interest, the molecular contribution to the scattering coefficient is of no consequence and may be neglected.

This section deals with the aspects of molecular extinction only. The aspects of aerosol extinction are treated in the following section.

2. MOLECULAR ABSORPTION

Molecular absorption of the  $\text{CO}_2$  laser wavelengths is primarily caused by the  $\text{CO}_2$  and  $\text{H}_2\text{O}$  molecules. At higher elevations, the  $\text{O}_3$  molecule with a band centered around  $9.7 \mu\text{m}$  becomes important.  $\text{CO}_2$  laser propagation is significantly affected by the atmospheric  $\text{CO}_2$  absorption band which contains the same frequencies produced by  $\text{CO}_2$  laser emission.

Thus, there is the unusual situation that the frequencies of a properly adjusted laser are exactly coincident with the center of the absorption lines. Absorption due to  $H_2O$  is caused by the accumulated wings of water vapor lines of the  $6.3 \mu m$  fundamental band and the pure rotational lines in the far infrared.

The molecular contribution to absorption of radiation by the atmosphere is most readily described in terms of the molecular extinction coefficient  $k_m(\nu)$  which gives the fractional energy lost per unit length in the direction of propagation. The extinction coefficient depends not only on the frequency but also on the temperature and pressure of the atmospheric constituents along the propagation path. To investigate the functional dependence of  $k_m(\nu)$  on  $\nu$ ,  $T$ , and  $P$ , it is convenient to define the absorption coefficient as the product of the line shape factor  $f(\nu-\nu_0)$  and the line strength  $S$  as

$$k_m(\nu) = \sum_{i=1}^n S_i f_i(\nu-\nu_{0i}), \quad (65)$$

where the summation is used to indicate that the determination of the absorption coefficient  $k$  at some frequency  $\nu$  requires the contributions from several absorption lines  $f_i$  with line strengths  $S_i$ . The line strength provides a measure of the transition probability at the center frequency. It provides a quantum mechanical description giving the probability that a photon of frequency  $\nu_0$  will be absorbed at the center frequency  $\nu_0$  of the particular transition

$$E''_i + h \nu_{0i} \rightarrow E'_i \quad (66)$$

The line shape  $f(\nu-\nu_0)$  relates the probability  $S_i$  of the transition at line center  $\nu_0$ , to that of any other frequency  $\nu'$  which is removed from line center.

For a transition from state  $i$  to state  $j$ , the line strength is given by (Reference 11)

$$S_{i,j} = \frac{N_j}{g_i N} \frac{8\pi^3 \nu_{i,j} |R_{i,j}|^2}{3hc} (1 - e^{-h\nu_{i,j}/kT}), \quad (67)$$

where

$N_j$  = the molecular concentration in the lower state

$N$  = total molecular concentration

$g_i$  = the statistical weight

$\nu_{i,j}$  = transition frequency

$T$  = absolute temperature

$|R_{i,j}|$  = matrix component of the dipole moment.

The temperature and pressure dependence of the line strength is given by (Reference 12)

$$S = S_0 \left(\frac{T_0}{T}\right)^m \exp \left[ \frac{-E''}{k} \left(\frac{T_0 - T}{T_0 T}\right) \right], \quad (68)$$

where  $S_0$  is the line strength at standard temperature and pressure (STP) in units of  $\text{cm}^{-2} \text{atm}^{-1}$ ,  $P$  is the absorber pressure in atm, and  $T_0$  is the reference temperature. The value of  $m$  depends on the molecular species.

### 3. LINE SHAPES

In examining transitions between discrete molecular energy levels, it was assumed that the resulting spectra consisted of individual monochromatic lines. In reality, this is not the case and the line shape is dependent on the conditions under which absorption (or emission) by molecules occur. In the Earth's atmosphere, the spectral profile is influenced by the processes of natural broadening, collision broadening, and Doppler effect. Natural broadening sets the minimum width of the

spectral line and, as will be shown, it can be neglected in comparison to the other two processes.

a. Natural Broadening

Natural linewidth is produced by the interaction of the molecule with a radiation field. Transition of a molecule from one quantum energy state to another occurs over a finite time interval. It follows from Heisenberg's uncertainty principle, that the vibration process accompanying this transition represents an infinite set of frequencies over a specific spectral range. The width of the interval depends on the time  $\Delta t$  that the molecule remains in the excited state E. The uncertainty in the energy is given by

$$\Delta E \approx \frac{h}{2\pi\Delta t} \quad (69)$$

with the incremental energy involved having the value

$$\Delta E = hc\Delta\nu \quad (70)$$

Comparing Equations 69 and 70 one gets the result

$$\Delta\nu_N \approx \frac{1}{2\pi c\Delta t} \text{ cm}^{-1} \quad (71)$$

Using the accepted value of 0.1 second for the lifetime for vibrational energy states in the mid-infrared, Equation 71 yields a value of  $\Delta\nu_N \approx 5 \times 10^{-11} \text{ cm}^{-1}$  which is insignificant when one considers  $\text{CO}_2$  laser frequencies around  $944 \text{ cm}^{-1}$ .

b. Collision Broadening

This type of interaction is also referred to as pressure broadening. It is the result of the interaction between an absorbing molecule with neighboring molecules resulting in deformation of the energy levels with the consequent spectral line broadening. The solution to this problem requires the treatment of very large numbers of mutually interacting systems all of which must be treated simultaneously. A rigorous solution to this problem does not exist. Suppose that while a molecule is in the process of absorbing or emitting radiation, a collision

with another molecule takes place perturbing the radiation process. After the collision which is assumed to take place in a time that is much less than the time required to emit the radiation, the radiation process proceeds as before the collision. The result is that instead of observing a single simple harmonic wave train that is infinite in duration, one observes a wave train that is modulated in frequency and amplitude. Thus, if one calculates the intensity as a function of frequency for many wave trains which have been interrupted by collisions, it is found that the frequency of the emitted radiation is spread out over a small region centered at the frequency of the original uninterrupted wave train. A solution to the collision broadening problem is given by the Lorentz line profile (Reference 12)

$$f(\nu - \nu_0) = \frac{1}{\pi} \frac{\alpha_L}{(\nu - \nu_0)^2 + \alpha_L^2} \quad (72)$$

where  $\nu_0$  is the frequency at the center of the spectral line, and  $\alpha_L$  is the Lorentz half-width of the spectral line which is given by (Reference 12)

$$\alpha_L = \alpha_{L0} \left[ \frac{P}{P_0} \right] \left[ \frac{T_0}{T} \right]^n \quad (73)$$

P and T are the effective pressure and temperature of the specimen, and n is a constant which is different for each of the molecular species involved. For the  $\text{CO}_2$  molecule n has a value of 0.58 and for the  $\text{H}_2\text{O}$  molecule n has a value of 0.62. The subscript o is used to designate the value of the quantity at standard temperature and pressure.

#### c. Doppler Broadening

Doppler broadening is produced by the relative motion of the molecules while undergoing an absorption (or emission) process. Consider all the molecules in a gas which are absorbing radiation during a given transition. Because of thermal motions of the molecules, some will be moving toward the observer's reference frame and some will be moving away. The radiation received from molecules moving away from the observer

will appear to be of lower frequency. Conversely, the molecules moving toward the observer will appear to emit higher frequencies. The result is that the apparent width of the emission is broadened. The shape of a Doppler broadened line is given by (Reference 11)

$$f(\nu - \nu_0) = (\ln 2 / \pi)^{1/2} (1/\alpha_D) \exp \left[ \frac{-(\nu - \nu_0)^2 \ln 2}{\alpha_D^2} \right] \quad (74)$$

where  $\alpha_D$  is the Doppler half-width given by

$$\alpha_D = 3.58 \times 10^{-7} \nu_0 (T/M)^{1/2} \quad (75)$$

T is the temperature at which the process takes place, and M is the molecular weight of the gas.

At sea level, pressure broadening attains a maximum and decreases with altitude in proportion to the reduction in pressure encountered. Near sea level the Doppler line width is negligible in comparison to the half-width arising from pressure broadening. At some altitude the width of a pressure broadened line will equal the Doppler width. Above this point, the Doppler width becomes increasingly larger and is the dominant mechanism for line broadening. For altitudes above 15 kilometers, both Doppler and pressure broadening have to be accounted for simultaneously. This leads to the Voigt line profile (Reference 12) given by

$$f(\nu) = \frac{\alpha_1}{\pi^{3/2}} \int_0^{\infty} \frac{e^{-x^2} dx}{\left[ (\nu - \nu_0) - \frac{2\alpha_D x}{\ln 2} \right]^2 + \alpha_L^2} \quad (76)$$

#### 4. WING THEORY

A comparison of the Doppler and Lorentz line profiles with similar strengths and line widths is shown in Figure 5. An important observation is that the Gaussian shape of the Doppler profile allows only a small absorption in the wings and thus the wings of a molecular absorption line is mainly the result of Lorentz broadening. Since the Voigt profile is

a convolution of the two curves shown, this means that the resulting line profile should be dispersed. The degree of exactness in regards as to how well the far wings are described by this dispersion profile has not been resolved, and line wing theory awaits more experimental data before an exact model can find general acceptance. As a result, several shape models have been proposed. The most prominent one is the Van Vleck-Weisskopf model given by Reference 13

$$f(\nu-\nu_0) = \frac{1}{\pi} \left(\frac{\nu}{\nu_0}\right) \left[ \frac{\alpha_L}{(\nu-\nu_0)^2 + \alpha_L^2} + \frac{\alpha_L}{(\nu+\nu_0)^2 + \alpha_L^2} \right] \quad (77)$$

where  $\nu_0$  is the resonant frequency of the molecule and  $\alpha_L$  is the half-width of the line at half-maximum intensity. In the infrared, absorption is significant only in the region  $|\nu-\nu_0| \ll \nu_0$ . Thus, in this region  $(\nu+\nu_0) > (\nu-\nu_0)$  and  $\nu/\nu_0 \approx 1$ . Under these conditions Equation 77 reduces to Equation 72.

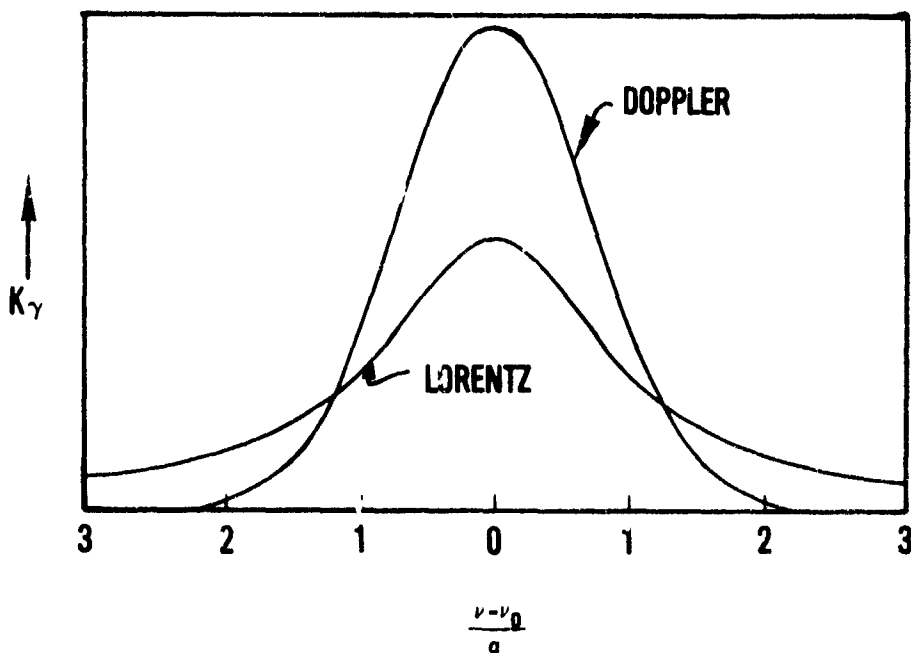


Figure 5. Doppler and Lorentz Spectral Line Shapes for Similar Intensities and Line Widths

The water vapor continuum has been and still is a source of controversy. The most accepted theory is that the continuum absorption is due to the influence of the remote wings of the 6.3  $\mu\text{m}$  absorption band and the rotational lines above 14  $\mu\text{m}$  of the water molecule. Recent workers (References 14, 15) have hypothesized a second absorption mechanism in the continuum and have advanced the dimer  $(\text{H}_2\text{O})_2$  theory. Measurements by Arefev (Reference 16) of the attenuation of  $\text{CO}_2$  laser radiation by water vapor at different temperatures and concentrations point in favor of the dimer theory. The dimer theory is still not accepted by the community and continuum models in use are based solely on contributions from the wings of the water vapor lines. Several workers have investigated the contributions from the far wings in the continuum (References 17-20).

A study by Roberts, Selby, and Bieberman (Reference 20) of attenuation in the 8-14  $\mu\text{m}$  region, has led them to postulate the empirically derived line shape factor

$$f(\nu-\nu_0) = \frac{a}{2\pi} \sin\left(\frac{\pi}{a}\right) \frac{a^{a-1}}{(\nu-\nu_0)^a + a^a} \quad (78)$$

where  $a$  is a constant obeying the rule  $1 < a < 2$ ... Roberts et al. have shown that Equation 78 models the contribution from the line wings much more precisely than the Lorentz model.

## 5. TRANSMISSION MODELS

Several atmospheric transmission models have evolved during the years. Most of these are based on the band model concept in which computed spectral lines are averaged into spectral bands. A spectral band is assumed to contain an array of spectral lines of a certain shape, intensity, half-width, and spacing according to some simple statistical model. In real spectra, this is not the case and this is the major source of discrepancy between real and computed spectra.

For the computation of laser atmospheric extinction, line models are used. The extinction coefficient is given by Equation 65 where  $f(\nu-\nu_0)$  is the line shape factor. For a single line where the Lorentz line profile is applicable, the extinction is given by

$$k(\nu) = \frac{S}{\pi} \frac{\alpha_L}{(\nu-\nu_0)^2 + \alpha_L^2} \quad (79)$$

In general a large number of absorption lines belonging to different molecules contribute to the attenuation at any specific laser frequency. In this case the total optical depth (O.D.) requires evaluation and is given by

$$\begin{aligned} \text{O.D.} &= k(\nu)W \\ &= \frac{1}{\pi} \sum_{j=1}^m \sum_{i=1}^n \frac{S_{i,j} \alpha_{i,j} m_j}{[(\nu-\nu_{i,j})^2 + \alpha_{i,j}^2]} \quad (80) \end{aligned}$$

where  $m_j$  is the amount of the  $j$ -th absorbing gas,  $W$  is the total absorber amount expressed in reciprocal units, and  $S_{i,j}$  is the line strength given in Equations 67 and 68. The double summation accounts for the fact that there are  $m$  separate absorbing species each having  $n$  lines with significant absorption at frequency  $\nu$ . This is the form of equation on which the high resolution transmission model HITRAN (Reference 19) is based. Clough (Reference 21) et al. have developed an accelerated version of HITRAN called FASCODE, which cuts the computer time required by a factor of approximately 100. They have achieved this by developing an algorithm which accelerates the convolution of the line shape function with the spectral line data used. The contribution of continuum absorption for self and foreign broadened components are included in the model. A layered atmosphere is assumed. The Voigt line profile is utilized for all layers with a bound of  $25 \text{ cm}^{-1}$  except at the higher altitudes where the Doppler line profile is used. The accuracy for the model is given as nominally  $\pm 0.5\%$  except in the wings of Voigt lines for which the error may reach  $\pm 3\%$ . FASCODE does well in calculating the contribution due to molecular extinction, but as of this writing, this model does not account for aerosol attenuation in the middle infrared.

SECTION IV  
AEROSOL EXTINCTION

1. INTRODUCTION

The attenuation of radiation by scattering is caused by discrete variations in the refractive index due to the presence of particles in the medium. The main scatterers are water droplets, dust, smoke, and haze particles. If the incident radiation has a wavelength much smaller than the size of the scattering particles, the interaction of the radiation with the scatterers results in Rayleigh scattering. If the dimensions of the scattering particles are comparable to wavelength of the incident radiation, the interaction of the radiation with the scatterers results in Mie scattering. At the infrared wavelengths of interest, Rayleigh scattering is not applicable in describing the process and one has to use Mie scattering theory. The exact solution to the Mie scattering problem is extremely difficult with the main difficulty being that one cannot express the angular scattering by a simple analytical expression. The phase function can only be described as a series of Legendre polynomials and this makes the numerical solution very laborious. Basically, Mie theory relates the scattering and absorption of electromagnetic energy by spherical particles having complex index of refraction  $m = n_1 - jn_2$ . From Mie theory, Deirmendjian (Reference 22) has shown that the extinction efficiency factors  $Q(\lambda)$  are given by

$$Q_s = 2x^{-2} \sum_{n=1}^{\infty} (2n+1) (|a_n|^2 + |b_n|^2) \quad (81)$$

$$Q_{\text{ext}} = 2x^{-2} \sum_{n=1}^{\infty} (2n+1) R_e (a_n + b_n) \quad (82)$$

$$Q_a = Q_{\text{ext}} - Q_s \quad (83)$$

where the subscripts a and s refer to absorption and scattering respectively, and  $Q_{\text{ext}}$  is the extinction (or attenuation) efficiency of the attenuating particles. The quantity  $x$  is shown as the size parameter

$$x = 2\pi r/\lambda \quad (84)$$

which is a function of both the wavelength and radius of the particle. The quantities  $a_n$  and  $b_n$  are coefficients in the expression for the scattered and attenuated fields. The quantities  $a_n$  and  $b_n$  can be expressed in terms of spherical Bessel functions and Hankel functions of the second kind with arguments  $x$  and complex refractive index  $m$ ,

$$a_n = \frac{\psi_n(x)\psi'_n(\beta) - m\psi_n(\beta)\psi'_n(x)}{\phi_n(x)\psi'_n(\beta) - m\psi_n(\beta)\phi'_n(x)}$$

$$b_n = \frac{m\psi(x)\psi'_n(\beta) - \psi_n(\beta)\psi'_n(x)}{m\phi_n(x)\psi'_n(\beta) - \psi_n(\beta)\phi'_n(x)}$$

where  $\beta = mx$  and  $\phi = \psi + j\Omega$ .

The quantities  $\psi$  and  $\Omega$  are Ricatti-Bessel functions and are defined in terms of half integral order Bessel and Neumann function with argument  $x$ .

$$\psi_n(x) = \left(\frac{\pi x}{2}\right)^{\frac{1}{2}} J_{n+\frac{1}{2}}(x)$$

$$\Omega(x) = -\left(\frac{\pi x}{2}\right)^{\frac{1}{2}} N_{n+\frac{1}{2}}(x)$$

The extinction efficiency factors as given by the exact Mie theory are difficult to compute and even with modern computers, the effort is time consuming. For computational purposes, the approximations worked out by Van de Hulst (Reference 23) and modified by Deirmendjian (Reference 24) are much more convenient to use. Van de Hulst obtained the following formulas for the extinction and absorption efficiency factors.

$$\begin{aligned}
Q_{\text{ext}} = & 2 - 4e^{-\rho \tan \beta} \left(\frac{\cos \beta}{\rho}\right) \sin(\rho - \beta) \\
& - 4e^{-\rho \tan \beta} \left(\frac{\cos \beta}{\rho}\right)^2 \cos(\rho - 2\beta) \\
& + 4\left(\frac{\cos \beta}{\rho}\right)^2 \cos 2\beta
\end{aligned} \tag{85}$$

$$Q_{\text{abs}} = 1 + \frac{e^{-4xn_1}}{2xn_2} + \frac{e^{-4xn_1} - 1}{8x^2n_2^2} \tag{86}$$

where

$$\rho = \frac{4\pi r}{\lambda} (n_1 - 1)$$

$$\tan \beta = \frac{n_2}{n_1 - 1}$$

$$x = \frac{2\pi r}{\lambda}$$

and  $n_1$  and  $n_2$  are the real and imaginary part of the refractive index, respectively. The above expressions were derived with the assumptions  $(n_1 - 1) \ll 1$ ,  $n_2 \ll 1$ , and  $2\pi r/\lambda \gg 1$ . Because of the assumptions in his theory, Van de Hulst approximations overestimate the extinction cross section for small  $\rho$  and underestimate it in varying degrees as  $\rho$  approaches and surpasses the position for the first maximum of  $Q_{\text{ext}}$  at  $\rho = 4.08$ . Deirmendjian (Reference 23) worked out correction factors which when applied to the Van de Hulst equations give a good approximation to the exact Mie equations. Deirmendjian (Reference 24) has shown that the use of his correction factors on the Van de Hulst equations give values that are within 6% of the values obtained from Mie calculations as applied to water particles at wavelength near 10  $\mu\text{m}$ . In view of the uncertainty in drop-size distributions and sphericity of water particles, the corrected Van de Hulst equations are widely used and will be used in this study.

However, the Deirmendjian correction factors have been modified to give better approximations for wavelengths near 10.6  $\mu\text{m}$ . The Van de Hulst equations as modified by Deirmendjian give larger errors for particles with radius smaller than 1.0  $\mu\text{m}$  (48% for  $r = 0.5 \mu\text{m}$ ). The modified Deirmendjian correction factors give answers which are within 1.0% of the exact Mie theory. Deirmendjian's correction factors and the improved Deirmendjian factors for wavelengths near 10.6  $\mu\text{m}$  are discussed in Appendix A. For the case of fogs and precipitation at the 10.6  $\mu\text{m}$  wavelength of interest, the most recent values of  $n_1 = 1.185$  and  $n_2 = 0.0662$  given by Hale and Querry (Reference 25) will be used as opposed to Centenno's (Reference 26) values of  $n_1 = 1.18$  and  $n_2 = 0.08$ .

The power  $\Delta P$  removed from a laser beam by a particle with cross-sectional area  $\pi r^2$  is given by

$$\Delta P = PQ(\lambda, r)\pi r^2 \quad (87)$$

For a unit volume containing  $N$  particles of the same size and composition, the total power removed from the beam becomes

$$\Delta P = PNQ(\lambda, r)\pi r^2 \quad (88)$$

In dealing with atmospheric phenomena, the particles encountered are of varying sizes and composition. Assuming that the particles are of known concentration  $n(r)$  and of the same composition, Equation 88 becomes

$$\sigma_{\text{ext}} = \pi \sum_{i=1}^N n(r_i)Q(\lambda, r_i)r_i^2 \quad (89)$$

where the attenuation ratio  $\Delta P/P$  is known as the extinction coefficient. Denoting the largest and smallest particle radii found in the distribution by  $R_2$  and  $R_1$  respectively, the integral representation of Equation 89 is given by

$$\sigma_{\text{ext}} = \pi \int_{R_1}^{R_2} r_i^2 n(r_i)Q(\lambda, r_i)dr_i \quad (90)$$

$Q(\lambda, r_i)$  is a dimensionless quantity, therefore the units of  $\sigma_{ext}$  are determined by the units of the radius  $r$  and the volume concentration  $n(r)$ . For  $r$  in  $\mu\text{m}$  and  $n(r_i)$  in  $\text{cm}^{-3}$ ,  $\sigma_{ext}$  will have the more standard units of  $\text{km}^{-1}$  when Equations 89 or 90 are multiplied by  $10^{-3}$ .

## 2. AEROSOL PROPERTIES

Extinction of laser radiation by aerosols is the result of both absorption and scattering. To derive accurate results from models, one must know the density and distribution of the size droplets in the propagation path. Aerosol composition varies mostly with time of the year, climate, altitude, and geographical location. For ocean front and other marine type atmospheres, salt spray predominates. Over continental areas, aerosol particles consisting of a mixture of soluble and insoluble materials occur. Formations of mixed particles by coagulation of aerosols produced by industrial processes do occur. The properties of these mixed particles are subject to change with changing atmospheric conditions. A particle can change size or form due to a condensation or evaporation process; thus, it is difficult to formulate a model that holds for all conditions. Many analytical expressions have been formulated to represent actual particle size distributions. These analytical expressions have given way to empirically derived formulation based on knowledge of the composition and properties of the aerosols.

The effect that an aerosol particle has on the propagation of radiation in the atmosphere depends in part on its complex index of refraction

$$m = n_1 - jn_2 \quad (91)$$

This is particularly true for  $\text{CO}_2$  laser radiation propagating in high water vapor concentration where absorption by water particles is determined by the imaginary part of the refractive index  $n_2$ .

The physical composition of continental aerosols varies between the extremes of dry insoluble dust particle (arid soil) and a clear salt soluble particle (industrial process). Junge (Reference 27) has shown that these particles grow with humidity. Measurements (Reference 27) indicate that these mixed particles behave more like droplets of salt solutions with expected refractive indices between that of NaCl and that of H<sub>2</sub>O. The refractive index of dry NaCl is in the vicinity of 1.5 while the real part of the refractive index of H<sub>2</sub>O is approximately 1.2 for wavelengths near 10 μm.

Because raindrops are not particles suspended in the atmosphere, they are not considered aerosols. However, they exhibit atmospheric optical properties to radiation similar to those exhibited by fog particles. For this study, rain drops (precipitation) will be treated as an aerosol.

### 3. SIZE DISTRIBUTION

#### a. Continental Aerosols

One of the earliest formulations proposed to represent continental aerosols is attributed to Junge (Reference 27). This takes the form of a power law and may be represented by

$$n(R) = \frac{C}{2.3} R^{-(\nu + 1)} \quad (92)$$

where R is the particle radius, C is a constant, and  $\nu$  is a parameter with value between 2.5 and 4.0. This distribution characterizes large particles satisfactorily but it is not very good in characterizing smaller particles and fails in the representation of maritime aerosol distributions. The distribution also has a singularity as  $R \rightarrow 0$ . An alternate distribution which avoids this singularity is the regularized (RPL) power law (Reference 28)

$$N(r) = N_0 / [1 + (r/a)^\nu] \quad (93)$$

where  $N(r)$  = number of particles with radii greater than  $r$ ,  $N_0$  is the total number of particles per unit volume, and  $a$  and  $\nu$  are adjustable parameters.

Another expression that adequately describes wet aerosols is based on the gamma function. The distribution given by Zuev (Reference 29) takes the form

$$f(a) = \frac{1}{\Gamma(\mu+1)} \mu^{\mu+1} \frac{a^\mu}{r^{\mu+1}} e^{-\mu a/r} \quad (94)$$

where

- $\Gamma(\mu+1)$  = gamma function
- $\mu$  = parameter
- $r$  = most probable radius
- $a$  = particle radius .

Ward, et al. (Reference 30) examined a number of models and concluded that the RPL model provided the best fit to the examined data including their own.

#### b. Fog Particles

Experimental results have shown that the power law does not describe adequately fog particle distributions. The gamma function may be used to describe fog particle distributions; however, a simpler distribution formulated by Shifrin (Reference 31) has found wider acceptance. This is given by

$$n(R) = AR^\alpha e^{-BR^\gamma} \quad (95)$$

where  $n(R)$  is the volume concentration at the radius ( $R$ ), and  $A$ ,  $B$ ,  $\alpha$ , and  $\gamma$  are positive constants. The parameters  $\alpha$  and  $\gamma$  can be adjusted to fit an observed fog particle size distribution. Having chosen  $\alpha$  and  $\gamma$ , the remaining constants can be uniquely determined by the total number of particles  $N$  per unit volume and by the mode radius  $r_m$  where the concentration is a maximum. Chu and Hogg (Reference 32) modified slightly

Shifrin's distribution by introducing the term  $R = r/r_m$  in Equation 95 to obtain

$$n(r/r_m) = A(r/r_m)^\alpha e^{-B(r/r_m)^\gamma} \quad (96)$$

The constant A can be determined from the integral

$$N = \int_0^\infty n(R) dR, \quad (97)$$

where Equation 85 has been substituted for  $n(R)$ . Letting  $y = BR^\gamma$ , then

$$R = (y/B)^{1/\alpha}$$

$$dR = (1/B)^{1/\alpha} y^{1/\alpha} y^{-1} dy$$

Substitution for R and dR, and regrouping terms, Equation 98 becomes the standard gamma integral

$$\begin{aligned} N &= \frac{AR_m}{\gamma B^{\alpha+1/\gamma}} \int_0^\infty y^{(\alpha+1/\gamma)-1} e^{-y} dy \\ &= \frac{AR_m}{\gamma B^{\alpha+1/\gamma}} \Gamma(\alpha+1/\gamma). \end{aligned} \quad (99)$$

Thus the value of A is found to be

$$A = \frac{\gamma N}{R_m} B^{\alpha+1/\gamma} \frac{1}{\Gamma(\alpha+1/\gamma)} \quad (100)$$

The value of B is determined by taking the derivative of  $n(R)$  and setting it to zero

$$\left. \frac{dn(R)}{dR} \right|_{r=r_m} = AR^{\alpha-1} e^{-BR^\gamma} (\alpha - \gamma BR^\gamma) = 0$$

Thus,  $\alpha = \gamma BR^\gamma$  and using the fact that  $R=1$  for  $r=r_m$  gives

$$B = \frac{\alpha}{\gamma} \quad (101)$$

This particle size distribution has been found to give a good representation for fog particles and other aerosols (References 31, 32). By proper fitting of the parameters  $\alpha$  and  $\gamma$  to the corresponding fog particle size distribution, the observed fog can be properly modelled. Figure 6 illustrates several distributions for selected values  $\alpha$  and  $\gamma$ .

### c. Precipitation

Precipitation models developed have been based on empirical results (References 32-34). Laws and Parsons (Reference 34) found experimentally that the rain drop size distribution is a function of the total precipitation rate. Their results were not shown in the form of a distribution function  $n(a)$  but as a related distribution  $m(a,p)$ , being given by the fraction of the total volume of water striking the ground due to drops of radius  $a$ . Goldstein (Reference 35) gives the relationship between the two distributions as

$$m(a,p) = \frac{n(a) (4\pi/3) v(a) a^3}{4\pi/3 \int_0^{\infty} n(a) v(a) a^3 da} \quad (102)$$

where  $v(a)$  is the terminal velocity of the drops with radius  $a$  in m/sec.

Goldstein determined that the precipitation rate is given by

$$p = 15.1 \int_0^{\infty} n(a) v(a) a^3 da \quad (103)$$

Substituting this expression in Equation 102 one obtains

$$m(a,p) = \frac{15.1 n(a) v(a) a^3}{p} \quad (104)$$

where

$$v(a) = 9.6(1 - e^{-11a}) \quad (105)$$

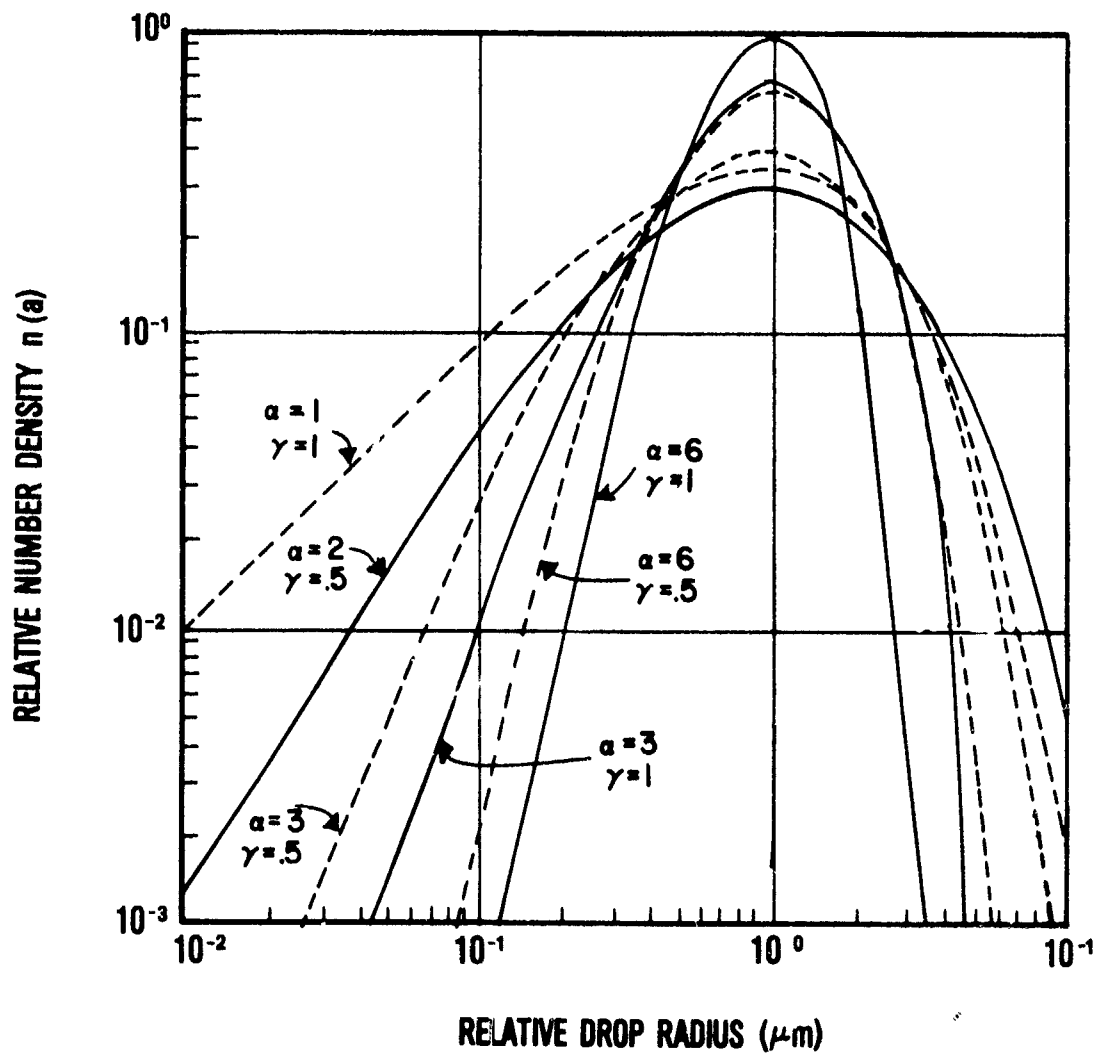


Figure 6. Size Distribution for Fog Model

and  $a$  is in cm. Using Equation 104 to substitute for  $n(a)$  in Equation 90, one obtains

$$\sigma_{\lambda} = p\pi \int_0^{\infty} \frac{Q_E(\lambda, a) m(a, p) da}{15.1 v(a) a}$$

Defining

$$g(a, \lambda) = \frac{\pi Q_E(\lambda, a)}{15.1 v(a) a}, \quad (106)$$

the extinction is given by

$$\sigma_{\lambda} = 0.1p \int_0^{\infty} g(a, \lambda) m(a, p) da \quad (\text{km}^{-1}) \quad (107)$$

Observations by Marshall and Palmer (Reference 36) led to the Marshall-Palmer distribution

$$N_D = N_0 e^{-\Lambda D}, \quad (108)$$

where  $N_D$  = number of drops in a unit volume with diameters in the interval  $D$  and  $D + dD$ ,

$N_0$  = empirically derived constant with value of  $0.08 \text{ cm}^{-4}$ ,

$\Lambda$  = constant related to rainfall rate,  $R$  in units of mm/hr and having a value of  $4.1R^{-0.21} \text{ cm}^{-1}$ .

A comparison of the Marshall-Palmer and the Laws and Parson distributions are plotted in Figure 7 versus experimental observations for three different rain rates. The plots indicate that the Palmer-Marshall distribution does not fit observations for drops of small diameters and that the deviation gets larger with increasing rain rates. However, it should be noted that as the rain rates increase the drop size also increases and the indicated difference in the distribution will be minimized. While the Laws and Parsons formula gives a better fit to experimental results for smaller sizes, it requires knowledge of the additional quantity  $v_i$ . The terminal velocity  $v_i$  can be approximated by (Reference 37)

$$v_i = 1420 D_i^{1/2} \text{ cm/sec} \quad (109)$$

for drops with diameters between 1 and 4 mm. Chen (Reference 38) formulated Laws and Parsons relationship as

$$n_i = \frac{r_i}{v_i v_i} \quad (110)$$

where  $v_i$  is the volume of the particle. For the range of validity of Equation 109, Equation 110 can be approximated by

$$n_i = \frac{r_i^{-2.5}}{8410} \quad (111)$$

It is important to remember that these distributions are empirical equations based on accumulation of highly variable samples. By examination of rainfall data obtained during a two-year period, Geotis (Reference 39) found that at diameters greater than 0.6 mm (the smallest size he could measure), the drop concentration was exponentially distributed. He reported that the exponential in Palmer-Marshall distribution varied with rainfall in an unpredictable manner. He found that  $\lambda = 3.7 D_0$  gave a good fit to the observed dropsize distribution curve, where  $D_0$  is defined as that drop diameter which divides the drop distribution in such a way that half the water content is contained in drops greater than  $D_0$ . The drawback is that  $D_0$  cannot be measured directly.

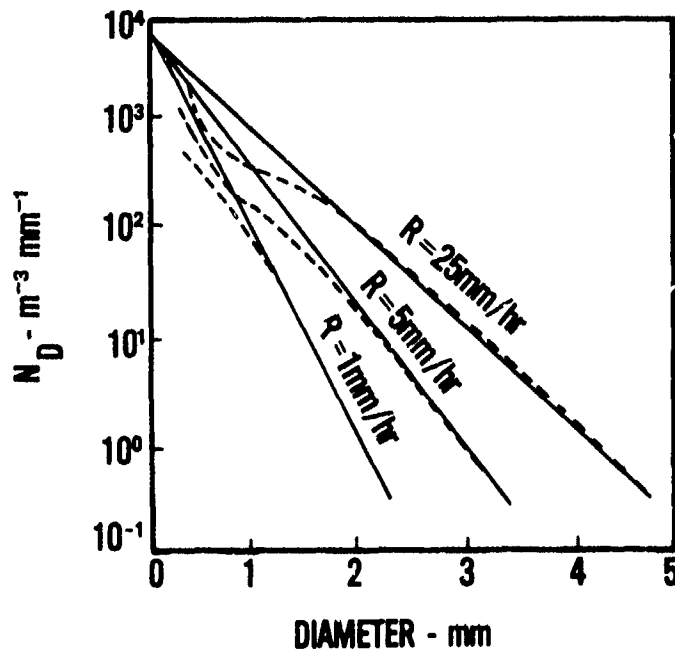


Figure 7. Comparison of the Marshall-Palmer Distribution (Solid Lines) and Observed Results of Laws and Parsons (Broken Lines) for Rain Rates of 1, 5, and 10 mm/hr. Adapted from Battan, Reference 37, p. 41

d. Snow

Snow is a form of precipitation which is difficult to characterize because of the irregular shape of the snow flakes. A form of the Marshall-Palmer distribution given by Equation 108 has been used to characterize snow. The value of the parameter  $D$  refers to the diameter of a sphere of water having the same mass as the original particle. When using the applicable quantities (Reference 40)

$$N_0 = 0.025R^{-0.94} \text{ cm}^{-4}$$

$$\Lambda = 2.29R^{-0.45}$$

in Equation 108, the size distribution for snow particles is given by

$$N_D = 0.025R^{-0.94} \exp(2.29R^{-0.45}) \quad (115)$$

where R is expressed in units  $\text{mm}^{-1}$ .

SECTION V  
SYSTEM DESIGN AND ANALYSIS

1. INTRODUCTION

Measurements performed in an uncontrolled environment such as the atmosphere require special techniques and instrumentation. Where practical, possible sources of error should be eliminated by suitable design of the test apparatus. Where this is not possible (or practical), the design should minimize the error involved. Because the propagation path used crosses a 200 foot taxiway and lies alongside a runway, atmospheric turbulence creates problems which require special attention. This section covers the effects caused by atmospheric turbulence, system design, and analysis.

2. ATMOSPHERIC TURBULENCE

Atmospheric turbulence is identified with fluctuations in air temperature and pressure which causes fluctuations in the transmitting medium index of refraction. Since the pressure (and humidity) change appreciably at a given altitude, most of the refractive index fluctuations arise primarily from temperature fluctuations in the atmosphere, which are produced by the turbulent mixing of hot air with cool air. This mixing occurs in zones or packets called eddies which range in size from the inner scale of turbulence  $l_0$ , to the outer scale of turbulence  $L_0$ .

The outer scale of turbulence  $L_0$  is a quantity associated with the introduction of energy in the turbulence. It is defined as that minimum size of large scales at which turbulent energy is no longer introduced in the field. The inner scale of turbulence is the size of the smaller scale that results in the conversion of energy in the turbulence into heat. The outer scale  $L_0$  varies in size, from tenths of a meter to a few meters near ground level, while the inner scale  $l_0$  is the order of one millimeter near ground level (Reference 41).

$L_0$  and  $l_0$  are also referred to as atmospheric inhomogeneities. It is these inhomogeneities with their varying refractive indexes that causes refraction and diffraction of the optical wavefront.

The index of refraction for the turbulent layer can be written as the mean of the index of refraction  $n$  in air, and a fluctuation  $\Delta n$  about the mean,

$$n_1 = 1 + \Delta n \quad (116)$$

where the refractive index of air has been rounded to  $n = 1$ . The fluctuations are correlated only over short distances and hence produce a general degradation in optical signals propagating through the atmosphere. In more specific terms, the fluctuations form turbulent eddies which cause refraction and diffraction of the optical wavefront. To see this more clearly, consider a plane optical wavefront propagating in air between a receiver and a transmitter as shown in Figure 8. Let the wavefront be incident at an angle  $\theta_0$  with respect to a plane turbulent layer of air of thickness  $L$  whose refractive index is given by Equation 116.

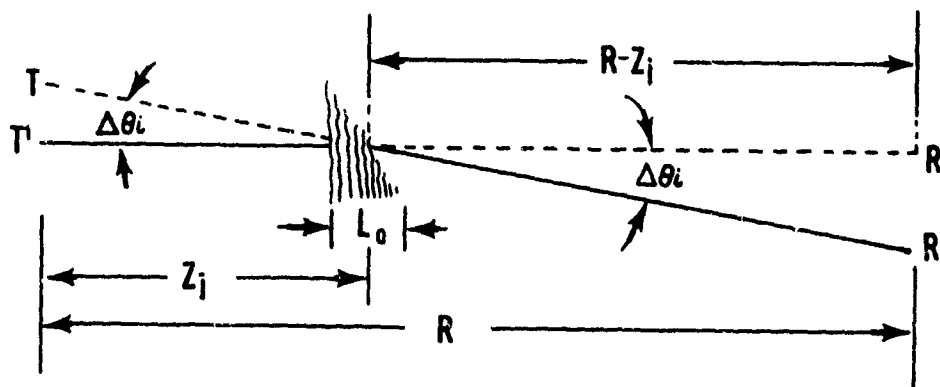


Figure 8. Projection of a Diffracted Laser Beam Due to Turbulent Eddies

After the wavefront enters the turbulent eddy  $L$ , diffraction causes the beam to be deflected at an angle  $\Delta\theta_i$  away from the intended trajectory. The new angle of propagation after entering the turbulent eddy is

$$\theta_i = \theta_o + \Delta\theta_i$$

The coherence length  $L$  is defined as the eddy size over which the index of refraction is approximately constant. By the definition of the coherence length, the turbulent eddy of size  $L_o$  in Figure 8 acts as a dielectric wedge with respect to the optical wavefront rather than as a plate. Therefore, the direction of the optical wavefront after emerging from the turbulent eddy is identical to the direction within the eddy which differs in direction from that of incident radiation. The effects repeat themselves for subsequent eddies along the path so that the overall effect is a summation over the different coherence intervals encountered. Since each angular deviation is uncorrelated with the angular deviation in the previous coherence interval, the total mean squared angular deviation  $\langle\Delta\theta^2\rangle$  is a function of the sum of the individual mean squared angular deviations.

When a laser beam passes through a turbulent atmosphere, its interaction with the eddies produces random variations in amplitude and phase of the signal. This randomness leads to a variety of effects which tend to degrade the performance of a laser system. Although somewhat inter-related, the most dominant effects are beam steering, spot (image) dancing, beam spreading, image blurring, and scintillation.

#### a. Spot Dancing

When the laser beam passes through pockets of air (eddies) in which the refractive index is different from the norm, the entire beam is deviated from its original direction. Depending on the frequency and number of these eddies along the path, the result is a movement of the laser beam in the receiver plane, which in turn causes the image to be focused at different points in the focal plane. Chiba (Reference 42) gives a relation for calculating spot dancing (also known as beam wander).

According to Chiba, the standard deviation of the linear displacement  $\beta_x$  of the laser beam in the receiver plane is given by

$$\beta_x = (1.90 C_n^2 L^3 D_t^{-1/3})^{1/2} \quad (117)$$

where  $D_t$  is the beam size at the transmitter output,  $\lambda$  is the laser wavelength,  $L$  is the distance between transmitter and receiver, and  $C_n$  is the index structure constant which can be obtained from a measurement of the temperature structure constant  $C_t$ , using the relationship (Reference 43)

$$C_n^2 = [79 \left(\frac{P}{T^2}\right) \times 10^{-6}]^2 C_t^2 \quad (118)$$

This quantity does not lend itself to accurate measurements. Estimates derived by Tatarski from experimental data, compared with measurements from Genoud and Goodwin give an order of magnitude agreement (Reference 44). Davies calculated that for turbulence near the ground,  $C_n$  can be approximated by the value corresponding to intermediate turbulence and gives the approximate value of  $4 \times 10^{-8} \text{ m}^{-1/3}$ . For strong turbulence  $C_n = 5 \times 10^{-7} \text{ m}^{-1/3}$ ; thus, it can be seen that there exists a large range of values for  $C_n$  and computations involving this quantity are at best very rough estimates.

#### b. Beam Spreading

Interaction of the laser with the inhomogeneities in the atmosphere results in small angle scattering. The net effect is that localized inhomogeneities produce changes in the divergence of the beam with a resulting spread of the signal energy over a larger area. The long-term spread for a Gaussian beam may be approximated by the relation (Reference 45)

$$\theta_s = \frac{\pi}{k \rho_0} \quad (119)$$

where  $k$  is the wave number and  $\rho_0$  is the lateral coherence length given by

$$\rho_0 = \left[ \frac{1.74 \times 10^{-2} \lambda^2}{C_n^2 L} \right]^{.6} \quad (120)$$

## c. Scintillation

Known also as power fluctuation, scintillation is the effect wherein destructive interference within the beam produced local fluctuations in the amplitude, so that across the beam there appears dark and bright areas compared to the average level of brightness. This leads to fluctuations in the received power which are strongly dependent on the receiving aperture dimensions. Tatarski has treated the subject of power fluctuations quite extensively in his book (Reference 46).

Tatarski postulates that the amplitude variations obey a log normal distribution and derives the following expression for the fluctuation of the logarithmic level of the amplitude

$$\begin{aligned} X_n^2 &= \log (A/A_0)^2 \\ &= .56k^{7/16} \int_0^R C_n^2(r) z^{5/16} dz \end{aligned} \quad (121)$$

which holds when  $L_0 \gg \lambda R \gg \ell_0$ .  $A_0$  is the initial amplitude,  $k$  is the wavenumber,  $\ell_0$  and  $l_0$  are the inner and outer scales of turbulence and  $R$  is the path length. Equation 121 holds for a propagation path of varying altitudes, and it allows for changes in the turbulent structure along the path. For paths which are nearly parallel to the earth's surface along regions where the turbulence structure does not change appreciably, Equation 121 reduces to

$$X_a^2 = .31 C_n^2 k^{7/16} R^{11/16} \quad (122)$$

The fluctuations in the logarithmic level of intensity  $I$  is related to that of amplitude  $A$  by

$$X_I^2 = 4 X_A^2 \quad (123)$$

Tatarski defines the maximum observable scintillation frequency in terms of the correlation interval  $\sqrt{\lambda R}$ . For the case of a receiver with an aperture  $d \ll R$ , the maximum scintillation frequency  $f_s$  is given by

$$f_{\max} = \frac{V_n}{\sqrt{\lambda R}} \quad (124)$$

where  $V_n$  is the wind speed normal to the line of sight between the transmitter and receiver. For  $d \gg \sqrt{\lambda R}$ , the higher spatial frequencies will be discriminated against and the frequency spectrum will be significant up to a frequency approximately expressed by (Reference 47)

$$f = V_n/d \quad (125)$$

#### d. Beam Steering

Beam steering is the deviation of the beam from the intended line of sight. The lateral displacement of the beam has an rms deviation

$$y = R\sigma_\theta/2 \quad (126)$$

along the axis of the receiver plane, where  $\sigma_\theta$  may be approximated by Equation 119 (Reference 48)

$$\sigma_\theta = \pi/k\rho_0$$

Thus,

$$y = R\pi/2k\rho_0$$

$$= R\lambda/4\rho_0 \quad (127)$$

#### e. Image Blurring

Image blurring is defined as the destruction of the phase coherence across the beam, causing the phase to change rapidly with position resulting in a blurring of the image. The angular blur of a point source is Gaussian with zero mean and fluctuation  $\sigma_\theta^2$  given by Equation 119.

## 3. SYSTEM DESIGN

In the design of a laser transmissometer, there are three possible choices for the selection of the receiver aperture size  $D_r$ . The aperture can be less, equal, or greater than the beam diameter  $d$ . The first case ( $D_r < d$ ) requires precise knowledge of the position of the receiving aperture in relation to the beam geometric configuration. Because of the position accuracies required to track a wandering beam, calibration in terms of total power received becomes very difficult and can lead to very large errors. The second case ( $D_r = d$ ) suffers from the same considerations and measurement errors can be worse than the first case due to the turbulence effects discussed earlier. By selecting  $D_r > d$ , most of the turbulence effects can be eliminated. Blurring and beam dancing effects will be present but they can be minimized by proper receiver design.

## a. Gaussian Optics

The Gaussian distribution which describes the fundamental mode of a laser is given by (Reference 49)

$$I(r) = \frac{2P_0}{\pi a^2} e^{-2r^2/a^2} \quad (128)$$

where  $P_0$  is the total output power,  $I(r)$  is the intensity at the distance  $r$  from the beam center and  $a$  is the radius where the intensity falls to  $1/e^2$  or 13.5% of the central intensity. The diffraction produced by passing a Gaussian beam through a circular aperture which truncates the distribution at the  $1/e^2$  points has been treated by Dickson (Reference 50). In the absence of aberrations a lens irradiated by a Gaussian beam will form an image that is dependent on the ratio of lens aperture to beam diameter  $2a$ . As the aperture is increased, the diffraction effects are reduced and as Dickson shows (Reference 50), diffraction effects are entirely eliminated when the aperture diameter is  $4a$ . Because of the high cost of large diffraction limited optics (and system growth), it is the accepted criteria that a well designed system may be truncated at the  $1/e^2$  intensity points. This is achieved with an aperture which is at least 1.4 times the beam width.

The far field beam divergence of a laser beam is given by

$$\theta = \frac{2\lambda}{\pi a} \quad (129)$$

where  $\theta$  is the full angle beam divergence measured at the  $1/e^2$  intensity points and  $a$  is the beam radius before propagation. Due to the long wavelength of a  $CO_2$  laser, the beam divergence is rather large, and the beam diameter will increase accordingly to the relation  $d = L\theta$ . By increasing  $a$  before transmission, a corresponding reduction in  $\theta$  is achieved. This is achieved by the use of a beam expander, which gives a collimation range of

$$L = \frac{\pi a^2}{\lambda} \quad (130)$$

This relation is easily derived from the geometry considerations shown on Figure 9. As the beam propagates, it grows in radius according to the relationship (Reference 51)

$$w = w_0 \left[ 1 + \left( \frac{\lambda L}{\pi w_0^2} \right)^2 \right]^{\frac{1}{2}}$$

where  $w_0$  is the beam radius at its waist.

#### b. Laser Transmissometer

The general layout of the laser transmitter is illustrated on Figure 10 with the beam expander configuration illustrated on Figure 11. The distance from the laser to the first element of the telescope is 170 cm. At this first surface, the beam radius has grown from 2.5 to 3.39 mm, and the minimum aperture to provide truncation at less than the  $1/e^2$  points is 9.50 mm. Using Equation 130, a trade-off analysis between range and magnification yields the selected magnification of 20X. This establishes the minimum size of telescope output aperture, at 190 mm to keep truncation at less than the  $1/e^2$  points. Ignoring diffraction and atmospheric effects, use of Equation 130 gives a beam width of 19 cm at a range of 1874 meters and a beam width of 13.5 cm at the half range point. At the selected range of 1000 meters, the beam width is approximately 14.7 cm.

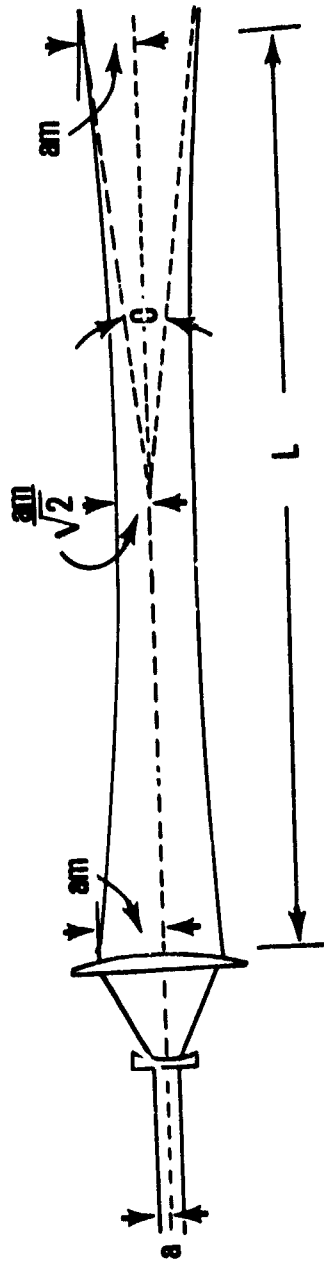
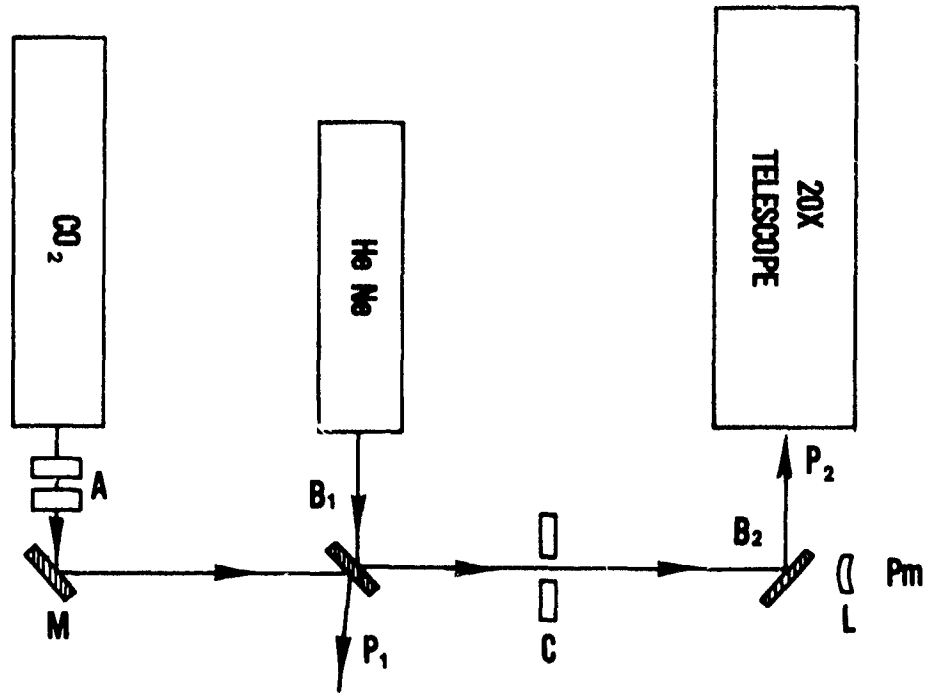


Figure 9. Propagation of a Collimated Gaussian Beam



- M - COPPER MIRROR
- B<sub>1</sub> - ZnSe WEDGE
- C - CHOPPER
- B<sub>2</sub> - BEAM SPLITTER, CdTe
- L - RELAY LENS, Ge
- A - ATTENUATOR

Figure 10. Optical Layout of Laser Transmitter

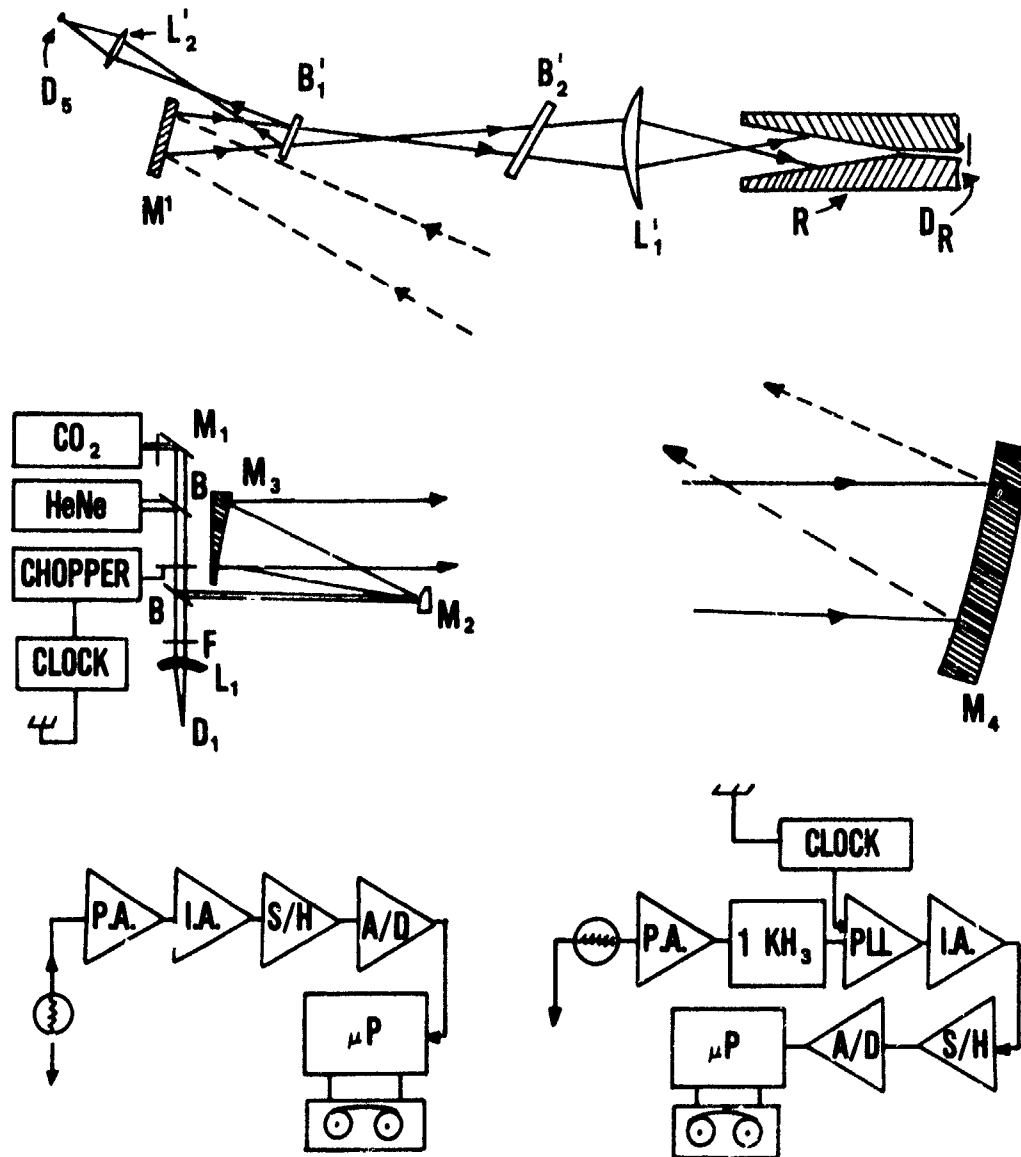


Figure 11. CO<sub>2</sub> Laser Transmissometer

The laser transmitter (Figure 10) consists of a multi-line  $\text{CO}_2$  laser which is mounted coaxially to a HeNe laser. A is an attenuator-polarizer combination used to present a safe level of power to the receiver detector during low extinction conditions. The first component attenuates the signal and the second is used to restrict transmission to the perpendicular component of the E vector. A two-degree wedge is used to axially combine the  $\text{CO}_2$  and HeNe laser outputs. The signals are modulated at a 1kHz rate using a WWVB NBS reference time signal which is also used to phase-lock the receiver to the transmitter.  $B_2$  is a 97% reflective beam splitter which provides a small portion of the signal to the reference detector Pm. A 20X beam expander is used to provide an 8-inch beam at the receiver. The energy at the receiver is collected by a 24-inch f/5 parabolic mirror which is tilted slightly off-axis. The signal is folded and passed through a couple of beam splitters which are used to limit the energy reaching the detector (Figure 11). In addition, the first beam splitter is used to provide a reference signal for calibration of the receiver and to measure the received HeNe whenever desired. Lens L is used to relay the  $\text{CO}_2$  signal into an f/10 solid recollector. This arrangement provides a steady signal to the detector during periods of high turbulence. When properly aligned, signal variation is approximately 1% in periods of extreme turbulence. Pyroelectric detectors are used at both receiver and transmitter. This limits the dynamic range of the system to 72dBs. The signal processing electronics are shown in Figure 11. The signal conditioning and recording are almost identical, except that in the receiver section, a phase-lock amplifier is used to phase-lock the receiver to the transmitter.

The 1kHz modulating signal was selected because of convenience for phase-locking and because it is well beyond the maximum scintillation frequency that could be experienced. Using the most pessimistic case of Equation 124 and a wind velocity of 30 m/hr, the maximum scintillation frequency was found to be 130 Hz.

Weather and particle size data was collected at the receiver end only. To ensure a nearly isotropic atmospheric path, the receiver signal was visually monitored using a digital voltmeter. Stable voltmeter

readings indicated a good probability of a stable atmospheric path, while a varying voltmeter reading indicated an unstable atmospheric path.

There are several factors which must be considered in selecting an optimum aperture size. These are:

1. Optical aberrations
2. Diffraction effects
3. Atmospheric effects

The transmitter telescope uses an off-axis parabola with a spherically corrected first element. This combination yields a virtually aberration free image of the magnified beam. The diffraction effects are eliminated by choosing an aperture at least twice the beam diameter. For a beam diameter of 14.7 cm, the diffractive component of the aperture  $\rho_d$  is 29.4 cm.

As previously mentioned, use of the index structure constant requires a very good knowledge of the types of turbulence encountered. Because the experiment is conducted in an area where high turbulence is a large probability, the value of  $C_n = 5 \times 10^{-7} \text{ m}^{-1/3}$  will be used in this study. This gives a coherence length of

$$\rho_o = \left[ \frac{1.74 \times 10^{-2} \times (10.6)^2 \times 10^{-12}}{10^3 \times 25 \times 10^{-14}} \right]^{.6} = 5.44 \text{ cm}$$

Spot dancing is calculated with the help of Equation 117. Using  $C_n = 5 \times 10^{-7} \text{ m}^{-1/3}$  in Equation 120, the coherence length for an optical path length is 16.3 cm. Spot dancing  $\beta_x$  is found to be

$$\beta_x = (1.90 C_n^2 L^3 D_t^{-1/3})^{1/2} = 2.85 \text{ cm}$$

Using  $\rho_0 = 5.44$  cm in Equation 119, the atmospheric spread is found to be

$$\beta_s = \frac{L\lambda}{z\rho_0}$$

$$= 9.74 \text{ cm}$$

Beam steering has two components which must be accounted for. The first may be termed a short-term component and may be mathematically approximated by Equation 130. This is found to be

$$y = \frac{L\lambda}{4\rho_0}$$

$$= 4.87 \text{ cm}$$

The long-term component is caused by changes in the refractive index of the atmosphere due to temperature variations and atmospheric particulate content. The day to day variations in the refractive index, change the path traversed by the beam and results in the beam falling at a different position in the receiving aperture. This effect could be minimized by using a true off-axis parabola, but because of the cost involved, this is not practical. The only practical solution is to relay all the energy captured by the aperture into the detector. This may be accomplished by realigning the laser transmitter prior to taking measurements so that the beam is at the optical center of the aperture. This beam deviation may be treated as an alignment error of linear displacement  $d = r\theta$ , where  $\theta$  is the refracted angle from the intended optical path. Assuming a maximum value of  $\theta = 100$  microradians, the increase in aperture diameter is 10 cm.

Collecting all the terms involved which contribute to enlargement of the receiver aperture, the minimum diameter is found to be

$$D \geq d + [\rho_d^2 + \beta_x^2 + \beta_s^2 + y^2]^{\frac{1}{2}} \geq 41.5 \text{ cm} \quad (132)$$

The chosen aperture has a 61 cm diameter which satisfies all of the above criteria for a range of up to 2.2 kilometers if the long-term drift  $d$  is compensated before initiating measurements.

#### 4. MEASUREMENT ERRORS

The quantity that is measured directly is the transmittance  $T$ . The extinction is computed from the transmittance value  $T$  and from Equation 63,

$$\sigma_{\lambda} = -1/L \ln T \quad (133)$$

where the path length  $L$  has the value of 1 kilometer and  $\sigma_{\lambda}$  has the units of  $\text{km}^{-1}$ . To obtain  $\sigma_{\lambda}$  in dB/km, one has to multiply the obtained quantity by 4.34. This is shown in Appendix B.

The error involved in the calculations is less than 2% and this is due to the uncertainty in the readout of the calibration device. To minimize this error, the calibrating radiometer was calibrated each time prior to calibration of the transmissometer, and the same instrument was used to calibrate both receiver and transmitter.

For moderate to high extinction conditions, the 2% error in transmittance becomes negligible when computing extinction. This is easily seen by expressing the natural log of  $T$  in a power series and then taking the total differential of  $\sigma_{\lambda}$ .

$$\begin{aligned} d\sigma_{\lambda} &= d[1 - \frac{1}{2}(T - 1) + \text{H.O.T}] dT \\ &= -dT + O(T - 1)^n \end{aligned} \quad (134)$$

Retaining the linear term only and dividing by  $\sigma_{\lambda}$ , one obtains the approximation

$$\left| \frac{d\sigma_{\lambda}}{\sigma_{\lambda}} \right| \approx \left| \frac{-dT}{\ln T} \right| \quad (135)$$

If one assumes a 2% error in the measurement for  $T = .01$ , the error in extinction is in the order of 0.4% while for  $T = 10^{-6}$  the error is in the order of 0.14%. For the high extinction cases where  $T > 10^{-4}$  an error of 10% gives errors in extinction in the order of 1%.

SECTION VI  
DISCUSSION OF RESULTS

1. INTRODUCTION

Results of extinction measurements are presented with measurements supported with particle size distributions where applicable. For clear and summer hazy weather, the measured transmission (or extinction) values are compared with those given by the FASCODE model. The values obtained with the model are of sufficient accuracy to determine the true molecular extinction, but as pointed out in Section III, this model cannot account for aerosol extinction. Clear weather results are presented first, followed in sequence by fog, rain, haze, and snow.

Measurements were made at discrete times at single wavelengths and during very short periods over several lines. With the piezoelectric mounted mirror, it was possible to make transmission measurements over six different wavelengths in approximately 60 to 75 seconds. This short time was necessary to obtain extinction measurements at several wavelengths under the same (or nearly the same) atmospheric conditions.

2. CLEAR WEATHER

Three examples of clear weather measurements are tabulated in Tables 1, 2, and 3. Data in Table 1 is representative of a humid, cold winter day, while the data in Table 2 is representative of a dry winter day. Both measured and calculated values indicate that for low temperatures, transmission is not greatly affected. Table 3 shows measured and calculated transmission values for a hot, humid summer day. For the cold winter days, the transmission losses are dominated by the CO<sub>2</sub> contribution to extinction. For the hot humid days, extinction is dominated by the water vapor continuum. Two points to be observed are that for the cold winter days the measured transmission is approximately 2% lower than that calculated using FASCODE, and for the hot, humid, summer days the measured transmission is slightly higher than that calculated by the FASCODE model. The 2% difference in transmission values for the winter measurements may in reality be less than that. Calculations by McCoy (Reference 52) give

TABLE 1

COMPARISON OF MEASURED AND CALCULATED  
TRANSMISSION FOR CLEAR WEATHER CONDITIONS,  
25 FEBRUARY 1981, 1300 HRS. VISIBILITY WAS  
APPROXIMATELY 18 KM

LINE NO.	$\lambda$ ( $\mu\text{m}$ )	$T_m$ (measured)	$T_c$ (computed)	$\Delta T$
P28	10.675	.914	.925	.011
P26	10.653	.909	.922	.013
P22	10.631	.900	.910	.010
P20	10.591	.895	.906	.011
P18	10.571	.897	.906	.009
R18	10.260	.893	.906	.013
R16	10.275	.888	.900	.012

Temperature = 36°F

Relative Humidity = 82%

Dew Point = 34°F

Pressure = 990 mb

TABLE 2

COMPARISON OF MEASURED AND CALCULATED  
TRANSMISSION FOR CLEAR WEATHER CONDITIONS,  
3 MARCH 1981, 0830 HRS. VISIBILITY WAS  
GREATER THAN 25 KM

LINE NO.	$\lambda$ ( $\mu\text{m}$ )	$T_m$ (measured)	$T_c$ (computed)	$\Delta T$
P28	10.675	.949	.969	.020
P26	10.653	.945	.965	.020
P22	10.611	.935	.957	.022
P20	10.591	.931	.953	.022
P18	10.571	.930	.952	.022
P14	10.532	.927	.951	.024
R18	10.260	.926	.947	.021
R16	10.275	.922	.945	.023

Temperature = 28°F

Relative Humidity = 40%

Dew Point = 17°F

Pressure = 990 mb



an absorption of  $0.06 \text{ km}^{-1}$  for a  $\text{CO}_2$  concentration of 335 parts per million for January type weather. This turns out to be a 94.2% transmission which falls halfway in between the measured and computed values by FASCODE.

### 3. FOG

Over 150 fog distributions were measured during the course of this study. A very large number of these were in the light fog category and of little interest to this study. Size distributions for three of these fogs are shown in Figures 12, 13, and 14. Measured and calculated transmission values corresponding to the distribution of Figure 12 are tabulated in Table 4. Transmission data for size distribution of Figure 13 is tabulated in Table 5, and that of Figure 14 is tabulated in Table 6. The fog of 20 January was very stable and the measured distribution hardly changed at all. The dotted curve corresponds to a size distribution measurement taken 25 minutes later. The extinction obtained from Mie theory yields only a  $0.02 \text{ km}^{-1}$  extinction due to the fog particulates. This is about a 2% loss in transmission. From Table 5 it is seen that the difference between the measured and computed values is approximately 7%; thus, there is a 5% unaccounted difference. A similar observation can be made for the data obtained on 23 January. The contribution to extinction by fog particulates was found to be  $0.008 \text{ km}^{-1}$ . The unaccounted transmission difference is approximately 3%.

Stable, light fog existed all day during February 17th. Computation of the aerosol contribution to extinction at  $10.6 \text{ }\mu\text{m}$  yielded a value of  $0.1 \text{ km}^{-1}$ . This compares well with the difference between the measured and computed extinction of 0.114 (Table 6) at  $10.6 \text{ }\mu\text{m}$ .

Heavy fog conditions were encountered during the 18th and 19th of February 1981. During those two days the extinction exceeded the dynamic range of the system more than half the time during which measurements were taken. To help in the analysis, it was useful to apply the relationship between extinction and the liquid water content in a fog. Chylek (Reference 53) derived a linear relationship of the form

$$\tau = bW \quad (136)$$

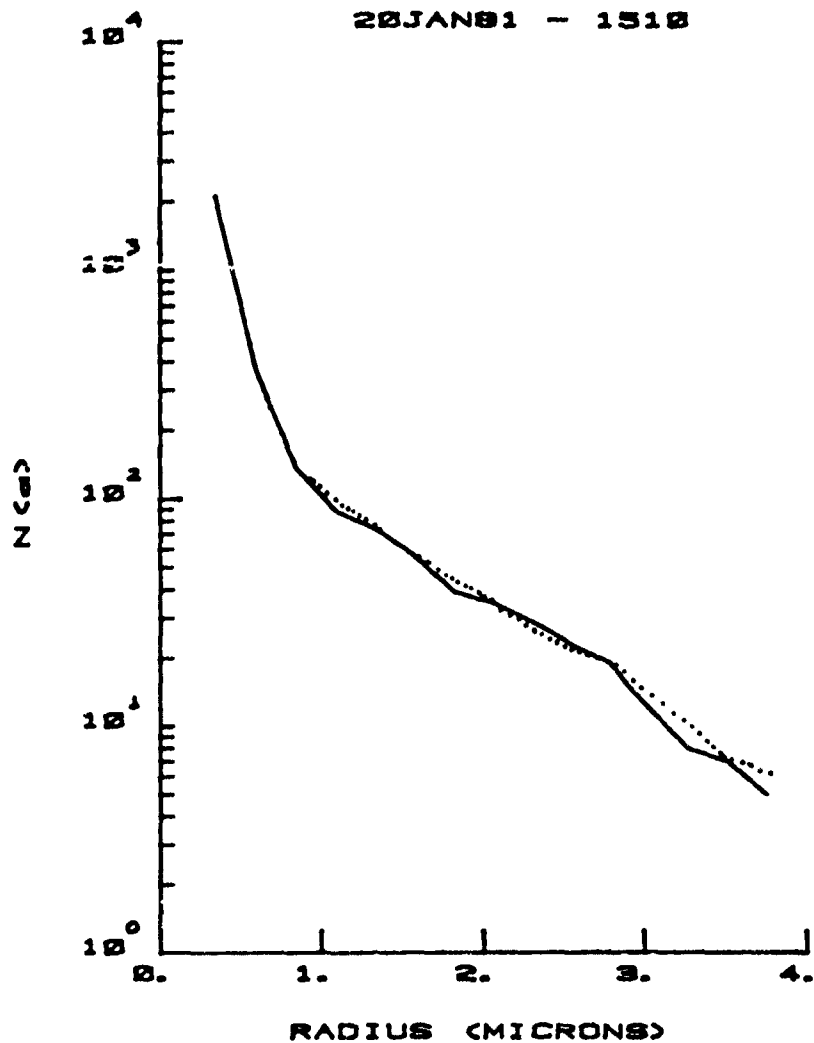


Figure 12. Particle Size Distribution for Light Fog, 20 January 1981

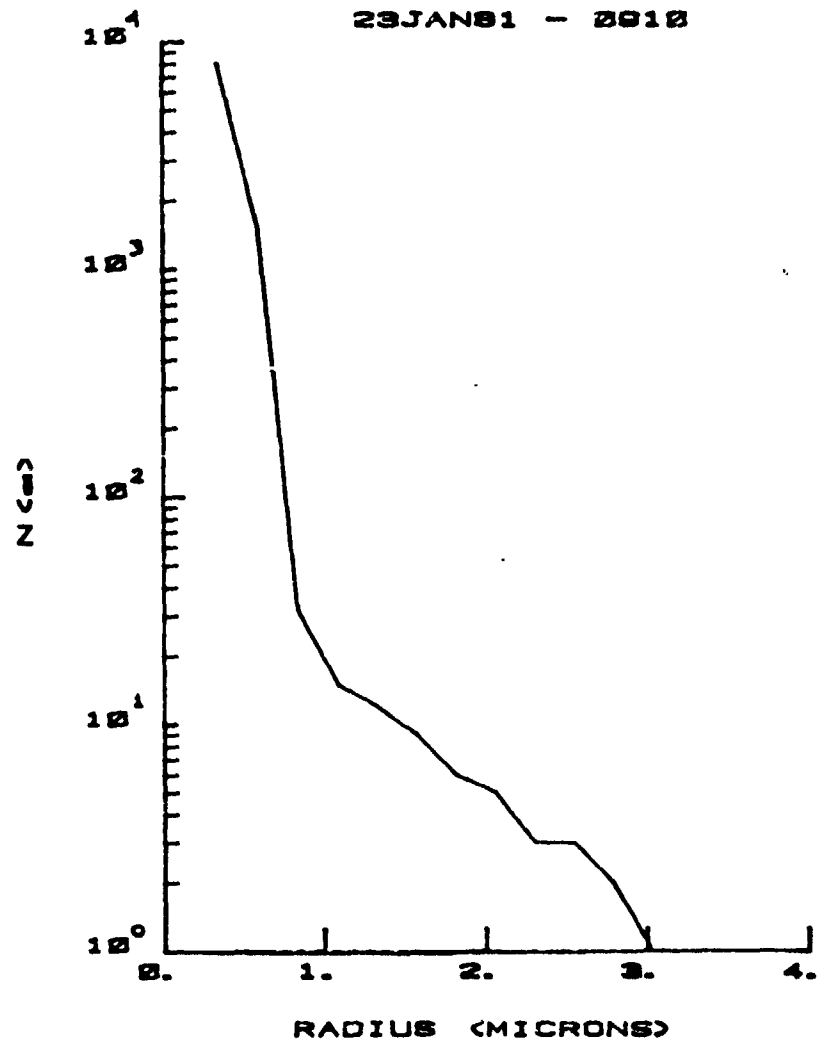


Figure 13. Particle Size Distribution for Light Fog, 23 January 1981

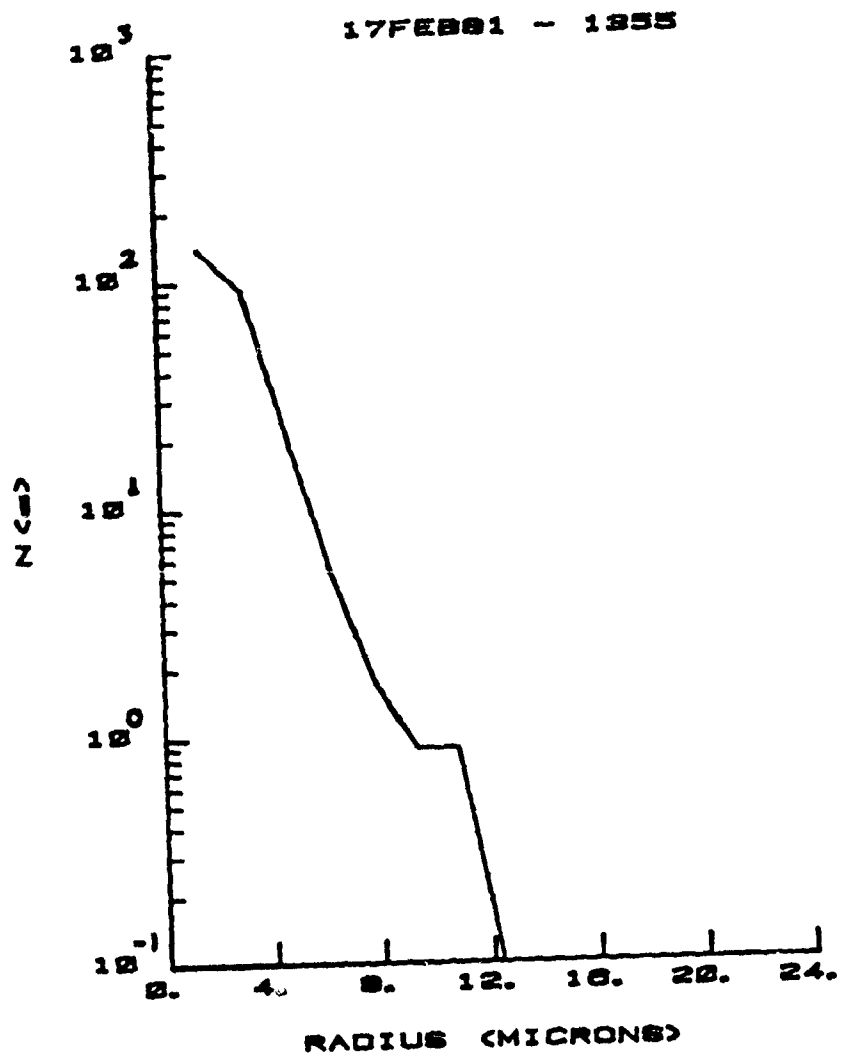


Figure 14. Particle Size Distribution for Light Fog, 17 February 1981

TABLE 4

MEASURED AND CALCULATED TRANSMISSION FOR  
 SEVERAL CO<sub>2</sub> LASER LINES UNDER LIGHT FOG  
 CONDITIONS, 20 JANUARY 1981, 1510 HRS. DATA  
 CORRESPONDS TO FOG DISTRIBUTION OF FIGURE 12

LINE NO.	$\lambda$ ( $\mu\text{m}$ )	$T_m$ (measured)	$T_c$ (computed)	$\Delta T$
P28	10.675	.888	.955	.067
P26	10.653	.878	.945	.067
P20	10.691	.866	.935	.069
P18	10.671	.864	.932	.068
P14	10.532	.861	.930	.069
R18	10.260	.867	.937	.070

Temperature = 36°F

Relative Humidity = 40%

Dew Point = 29°F

Visibility = 4 mi

TABLE 5

MEASURED AND CALCULATED TRANSMISSION FOR  
 SEVERAL CO<sub>2</sub> LASER LINES, 23 JANUARY 1981,  
 0920 HRS. LIGHT STABLE FOG WAS PRESENT  
 DATA CORRESPONDS TO FOG DISTRIBUTION OF  
 FIGURE 13

LINE NO.	$\lambda$ ( $\mu\text{m}$ )	$T_m$ (measured)	$T_c$ (computed)	$\Delta T$
P28	10.675	.892	.938	.046
P26	10.653	.889	.934	.045
P22	10.611	.883	.925	.042
P20	10.591	.880	.920	.040
P18	10.571	.880	.920	.040
R16	10.275	.873	.911	.038
R13	10.260	.877	.916	.039

Temperature = 32.2°F      Relative Humidity = 75%

Dew Point = 26.5°F      Visibility \* 2 km

TABLE 6

MEASURED AND COMPUTED EXTINCTION VALUES  
FOR SEVERAL WAVELENGTH UNDER LIGHT FOG  
CONDITIONS, 17 FEBRUARY 1981, 1440 HRS

LINE NO.	$\lambda$ km <sup>-1</sup>	$\sigma_m$ km <sup>-1</sup>	$\sigma_c$ km <sup>-1</sup>	$\Delta\sigma$ km <sup>-1</sup>
P28	10.675	.291	.172	.119
P26	10.653	.297	.177	.120
P20	10.591	.308	.194	.114
P18	10.571	.304	.198	.119
R18	10.260	.302	.194	.108

Temperature = 53.35°F

Relative Humidity = 96%

Dew Point = 51.85°F

Pressure = 990 mb

where  $b$  is a constant and  $W$  is the liquid water content. Chylek showed this relationship to be independent of the size distribution and also that the relationship holds only for a definite wavelength which is determined by the size of the largest droplets present in a given layer of fog or clouds. Chylek results indicate that the maximum wavelength for which Equation 136 holds is  $11 \mu\text{m}$ , for a distribution in which the larger particles have maximum radii  $r_m$  near  $14 \mu\text{m}$ . For this case the constant  $b$  in Equation 136 has a value of 128. Using the data provided and the derived relationship

$$\tau_w = \frac{3\pi c}{2\rho\lambda} \quad (137)$$

the relationship at  $10.6 \mu\text{m}$  gives

$$\tau_w = 147 W \quad (138)$$

with the larger particles having radii of  $13 \mu\text{m}$ . It is not critical that  $r$  be less than  $r_m$ , but that the larger sizes do not contribute heavily to either  $\sigma$  or  $W$ .

Equation 136 was derived empirically from variable samples and is not exact. However, for the case of heavy extinction, one does not need to be exact, and the approximation it gives provides one with additional information for correlation with extinction obtained through use of Mie calculations.

The liquid water content of a concentration of particles  $N$  of size  $r$ , density  $\rho$ , and volume  $V$  is given by

$$W = \rho V N(r) \quad (139)$$

For a polydispersion of spherical water droplets, the total liquid water content is obtained by integrating Equation 139 over the size range of the particle distribution. Equation 139 then takes the form

$$W = \frac{4}{3} \pi \rho \int_{r_1}^{r_m} N(r) r^3 dr \quad (140)$$

The number distribution was converted to a density distribution by dividing  $N(r)$  by the volume sample and then dividing this value by the sampling time of the measurement. Numerical integration was then performed to obtain  $W$ .

Extinction data for the morning of 18 February 1981 is tabulated in Table 7. Between 0605 and 0655 hours, extinction in the optical path exceeded the dynamic range of the system. The extinction computed from the size distribution and the extinction cross section is tabulated under  $\sigma_c$ . The last two columns give the fog liquid water content in  $\text{gr/m}^3$  and the extinction obtained by use of Equation 138. Comparison of  $\sigma_c$  and  $\sigma_w$  gives an amazingly good correlation between the two quantities. Measurements taken at 0705 and 0715 show a good correlation between  $\sigma_m$  and  $\sigma_c$  indicating that the fog was very uniform at these times. Figures 15 and 16 show several size distribution corresponding to the data tabulated in Table 7. Both of these figures illustrate the bimodal tendency of some of the distributions. Both of these figures show that a small shift in the concentration of large particles can cause a large change in the measured extinction. Distribution for 0610 and 0615 hours appears to be almost identical in size but from Table 7, it can be seen that there is a 31 dB/km difference in extinction between them. Table 8 gives extinction data obtained in medium density fog and Table 9 presents data collected in light density fog. As can be observed, there is not much change in extinction between the difference wavelengths. Whatever differences are observed are mostly due to the dynamic nature of the fog. Figure 17 illustrates the size distribution for the light fog conditions of the data shown in Table 9. Table 10 gives the transmission and extinction values during the fog lifting period for the 18th of February.

February 19th provided an excellent opportunity for fog measurements. Fog would roll in, stabilize, and then move out to be followed by fog with entirely different characteristics. Data for a continuous three and one-half hour period is tabulated in Tables 11 through 13. Size distributions representative of the data tabulated in Table 11 are plotted in Figures 18 and 19. Figure 19 shows the stable nature of the fog between 0545 and 0605 hours. The 0550 distribution corresponds to an extinction of 66.9 dB/km.

TABLE 7

EXTINCTION OF 10.6  $\mu\text{m}$   $\text{CO}_2$  LASER RADIATION.  
 DATA TAKEN FROM 0605 TO 0715, 18 FEB 81.

TIME	$r$ $\mu\text{m}$	$\sigma$ $\text{dB}/\text{km}$	$\sigma_c$ $\text{dB}/\text{km}$	$W$ $\text{gr}/\text{m}^3$	$\sigma_w$ $\text{dB}/\text{km}$
0605	3.53	--	140.8	.2181	139.1
0610	3.52	--	143.4	.2384	152.1
0615	3.64	--	112.6	.1863	118.9
0620	3.75	--	82.0	.1257	80.2
0625	3.84	--	61.0	.0992	63.3
0630	3.65	--	75.4	.1256	80.1
0635	2.92	--	63.2	.1064	67.9
0640	3.30	--	73.8	.1239	79.0
0645	3.29	--	93.4	.1540	98.2
0650	3.40	--	102.4	.1674	106.8
0655	3.20	--	81.1	.1334	85.1
0700	2.61	18.83	22.8	.0396	25.3
0705	2.18	10.28	10.9	.0712	13.5
0710	2.54	16.81	22.8	.0386	24.6
0715	2.26	10.45	10.4	.0201	12.8

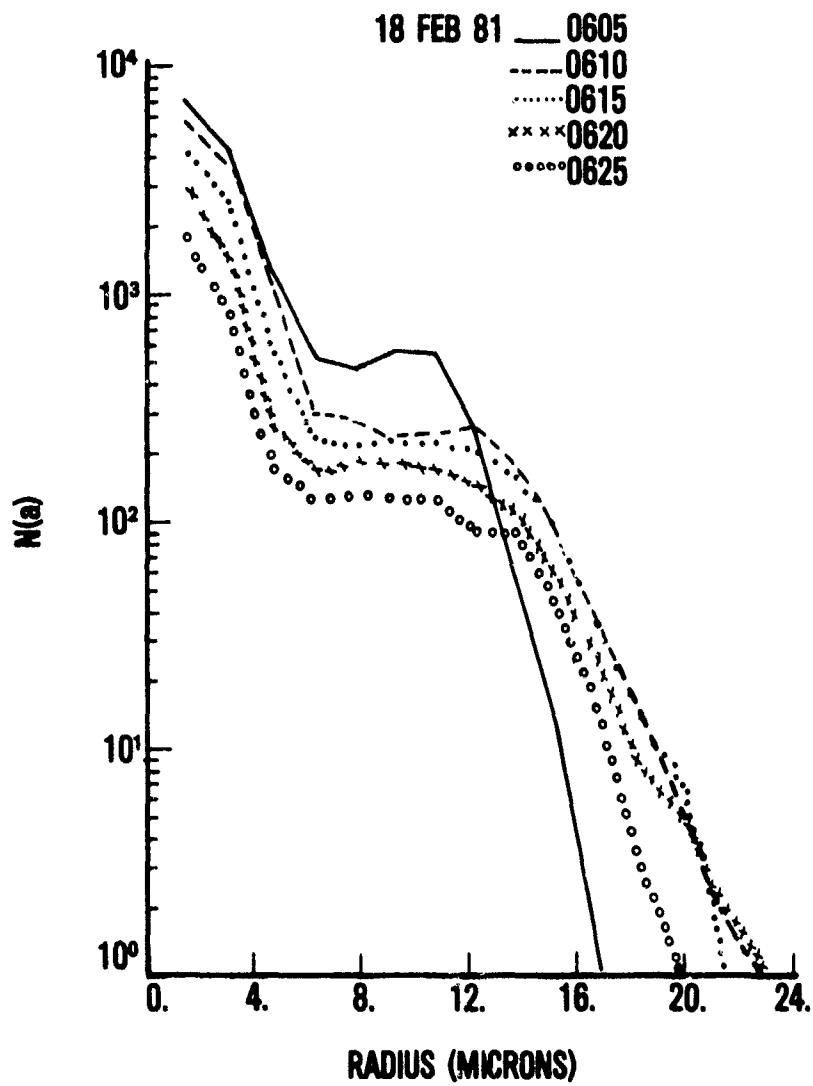


Figure 15. Particle Size Distribution for Dense Fog, 18 February 1981, 0605-0625 hrs

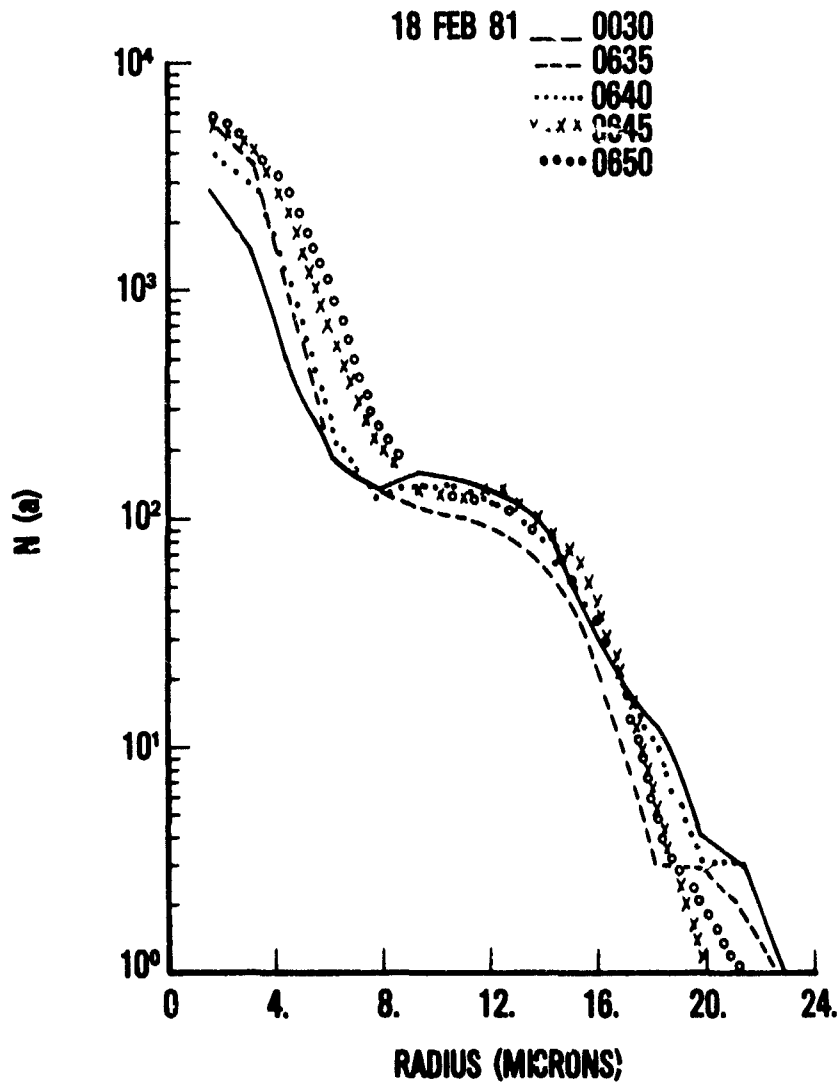


Figure 16. Particle Size Distribution for Dense Fog, 18 February 1981, 0630-0850 hrs

TABLE 8

EXTINCTION OF CO<sub>2</sub> LASER RADIATION IN MEDIUM  
 DENSITY FOG FOR SEVERAL LINES, 18 FEBRUARY  
 1981, 0658-0659 HOURS

$\lambda$ ( $\mu\text{m}$ )	$\sigma_m$ (dB/km)	$\sigma_c$ (dB/km)
P28	10.675	33.3
P26	10.673	33.8
P20	10.591	34.0
P18	10.571	33.9
R18	10.260	35.6
R16	10.275	35.6

Temperature = 55°F

Relative Humidity = 100%

Dew Point = 55°F

Pressure = 990 mb

TABLE 9

EXTINCTION OF CO<sub>2</sub> LASER RADIATION IN LIGHT  
DENSITY FOG FOR SEVERAL WAVELENGTHS,  
18 FEBRUARY 1981, 0715-0716 HOURS

LINE NO.	$\lambda$ ( $\mu\text{m}$ )	$\sigma_m$ (dB/km)
P28	10.675	8.98
P26	10.653	9.28
P20	10.591	10.28
P18	10.571	9.41
R18	10.260	10.44

Temperature = 54°F      Relative Humidity = 100%

Dew Point = 54°F      Pressure = 990 mb

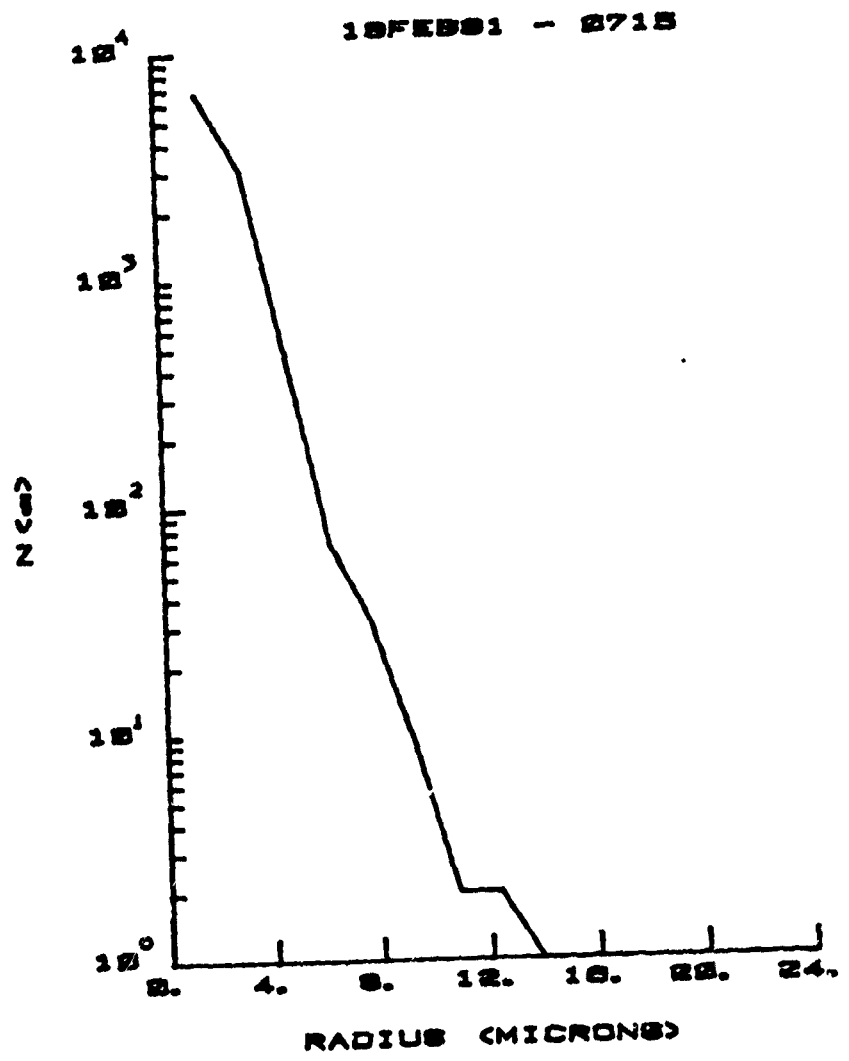


Figure 17. Particle Size Distribution for Medium Density Fog, 18 February 1981, 0715 hrs

TABLE 10  
MEASURED TRANSMISSION AND EXTINCTION DURING  
FOG LIFTING PERIOD, 18 FEBRUARY 1981

TIME	T ( $10^{-2}$ )	$\sigma_m$ (db/km)
0717	16.14	7.92
0718	26.70	5.74
0719	33.70	4.73
0720	41.41	3.83
0721	51.74	2.86
0722	55.94	2.58
0723	64.56	1.90
0724	69.15	1.60
0725	74.02	1.31
0726	76.52	1.16
0727	76.20	1.18

Temperature - 53.8°F

Dew Point = 54°F

Relative Humidity = 99%

Pressure = 990 mb

TABLE 11

EXTINCTION OF CO<sub>2</sub> LASER RADIATION IN  
HEAVY FOG. DATA TAKEN 19 FEB 81

TIME	$r_m$ $\mu m$	$\sigma_m$ dB/cm	$\sigma_c$ dB/cm	$W$ gr/m <sup>3</sup>	$\sigma_w$ dB/cm
0455	3.06	---	74.1	.1231	78.5
0500	2.59	31.5	20.4	.0531	33.9
0505	2.99	52.7	54.2	.0891	56.8
0510	2.66	36.9	29.2	.0505	32.2
0515	2.58	28.3	27.3	.0498	31.8
0520	2.15	17.2	7.0	.0154	9.8
0525	2.35	15.1	4.6	.0087	5.5
0530	3.66	44.3	53.7	.0840	53.6
0535	3.44	31.7	34.8	.0547	34.9
0540	3.81	—	76.7	.1176	75.0
0545	3.99	67.6	66.4	.1015	64.8
0550	3.89	66.9	66.7	.1025	65.4
0555	4.99	--	148.4	.2200	140.4
0600	4.59	--	103.1	.1539	98.2
0605	4.75	--	114.8	.1707	108.9

TABLE 12

EXTINCTION OF CO<sub>2</sub> LASER RADIATION IN HEAVY  
FOG, 19 FEB 81

TIME	$r_m$ $\mu m$	$\sigma_m$ dB/km	$\sigma_c$ dB/km	$W$ gr/m <sup>3</sup>	$\sigma_w$ dB/km
0610	2.81	34.7	31.5	.0548	35
0615	4.74	--	64.1	.09	61.1
0620	3.55	--	55.8	.0865	55.2
0625	3.18	--	49.9	.0795	50.7
0630	3.41	--	64.4	.1001	63.9
0635	3.37	53.9	54.7	.0852	54.4
0640	3.51	52.6	51.9	.0802	51.2
0645	3.94	52.9	54.0	.0828	52.8
0650	3.82	51.6	49.4	.0754	48.1
0655	3.60	53.2	54.5	.0841	53.7
0700	3.11	38.4	40.6	.0641	40.9
0705	3.18	37.9	38.7	.0613	39.1
0710	3.10	37.6	36.6	.0581	37.1

TABLE 13

EXTINCTION OF 10.6  $\mu\text{m}$   $\text{CO}_2$  LASER RADIATION  
IN HEAVY FOG, 19 FEB 81<sup>2</sup>

TIME	$r_m$ $\mu\text{m}$	$\sigma_m$ dB/km	$\sigma_c$ dB/km	$W$ gr/m <sup>3</sup>	$\sigma_w$ dB/km
0715	4.25	--	107.4	.1704	108.7
0720	4.57	--	173.3	.2749	175.4
0725	4.46	--	167.1	.2614	166.8
0730	5.50	--	270.9	.4357	277.9
0735	5.66	--	291.0	.4707	300.2
0740	5.73	--	281.0	.4566	291.3
0745	5.23	--	276.5	.4455	284.2
0750	4.49	--	220.3	.3564	227.4
0755	3.70	--	85.9	.1361	86.8
0800	2.62	32.4	30.2	.0543	34.6
0805	2.54	24.9	23.2	.0424	27.0
0810	2.65	31.8	31.6	.0593	37.8
0815	2.66	50.85	63.1/2	.1155	73.7
0820	2.83	--	87.4	.1523	97.1
0825	3.20	--	92.3	.1590	101.4

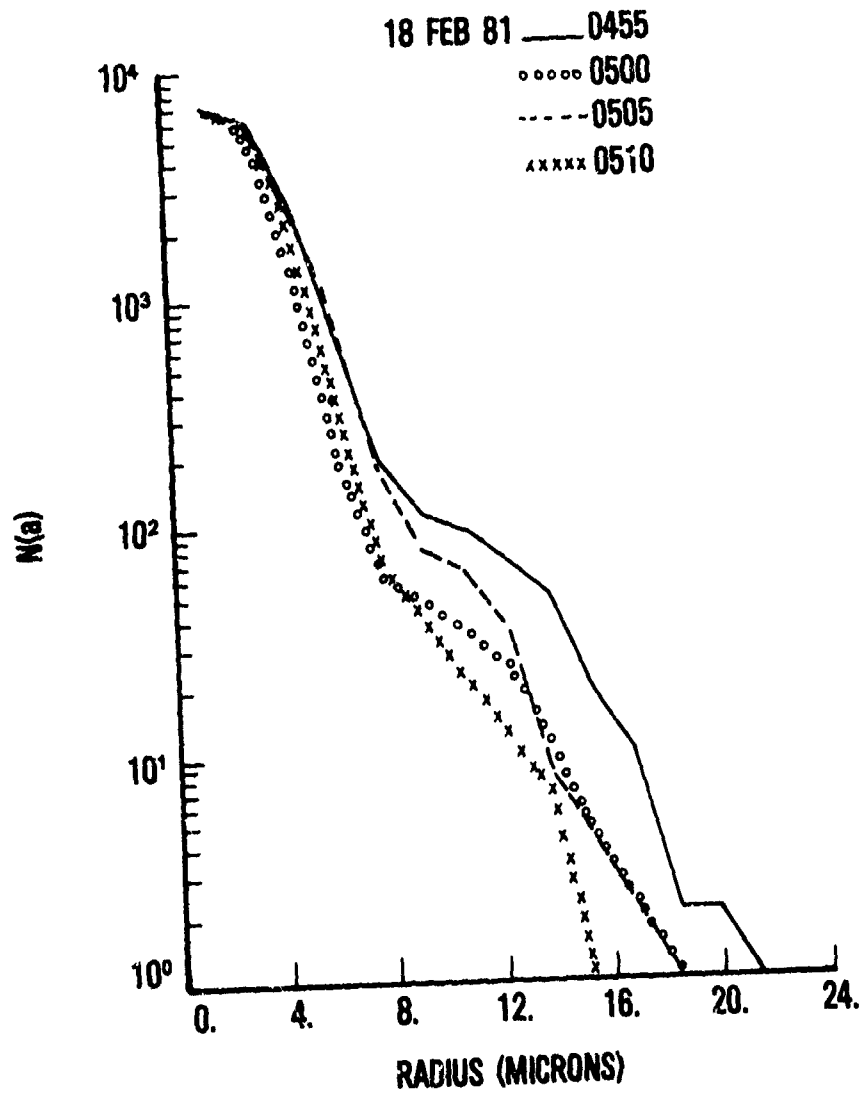


Figure 18. Particle Size Distributions for Dense Fog, 19 February 1981, 0455-0510 hrs

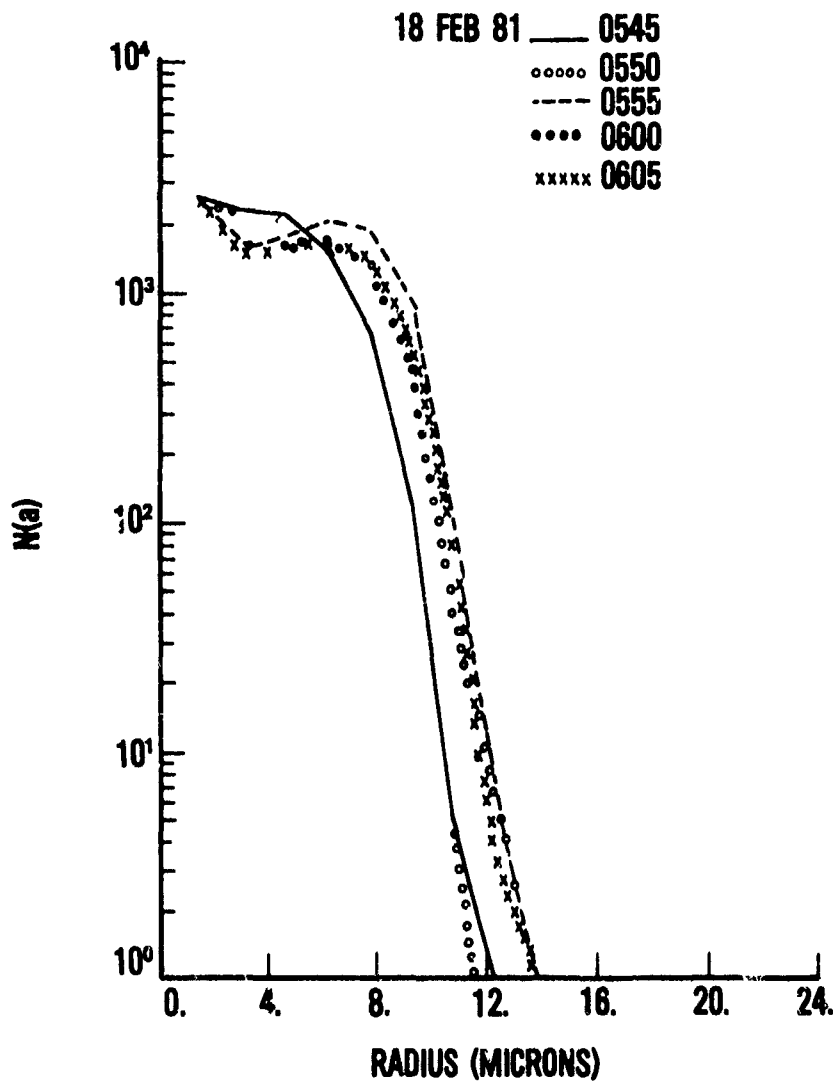


Figure 19. Particle Size Distributions for Dense Fog, 19 February 1981, 0545-0605 hrs

At this time a series of measurements were made for several wavelengths. The data is tabulated in Table 14. Shortly after measuring the R16 line, the signal was lost and was not detectable during the next 40 minutes. The stable nature of the fog between 0620 and 0710 is illustrated in Figure 20. This is reflected by the good correlation between  $\sigma_m$ ,  $\sigma_c$ , and  $\sigma_w$ . Figure 21 presents size distributions taken ten minutes apart. As can be seen from Table 13, the size distributions correspond to extinction of 173.3, 270.9, 281, and 220.3 dB/km. The highest extinction computed during this period was 291 dB/km and occurred at 0735 hours. Size distributions corresponding to extinction data taken between 0805 and 0820 hours are plotted in Figure 22. The fog reached its minimum intensity at 0805 hours and had started to grow in intensity at 0810 hours. The part of the distribution with radius less than six micrometers is almost identical to the same part of the distribution obtained at 0805 hours. The small increase shown in the larger particles between 6 and 23 micrometers is responsible for more than 30% rise in extinction. A similar analogy may be made for the distributions shown for 0815 and 0820 hours. The most interesting feature of Figure 22 is that the mean and maximum radius of the distributions shown are nearly equal in size to each other, yet there is almost a 4 to 1 difference in extinction produced. Variation in extinction with changing fog is documented in Table 15. Data was collected with the R18 line (10.26  $\mu\text{m}$ ). A thirty-one-fold decrease in transmission is observed between 0808 and 0810 hours. Table 16 shows transmission and extinction data for several  $\text{CO}_2$  laser lines in medium density fog. Again, it is seen that extinction in fog is not wavelength dependent even for medium density fogs. The larger increase between the R18 and the R16 is the last line to appear in the measurement sequence, and by then the fog properties have slightly changed along the optical path.

#### 4. RAIN

Rain extinction measurements were obtained for single lines as a function of rain rates over several intervals and for series of lines over very short intervals. Figures 23, 24, and 25 are plots of extinction versus rain rates for the 22nd, 28th, and 29th of April 1981. The solid

TABLE 14

EXTINCTION OF CO<sub>2</sub> LASER RADIATION IN HEAVY  
FOG FOR SEVERAL WAVELENGTHS, 19 FEBRUARY 1981,  
0545-0546

LINE NO.	$\lambda$ ( $\mu\text{m}$ )	$\sigma$ (dB/km)
P28	10.675	68.6
P26	10.653	69.0
P18	10.571	69.8
P14	10.532	69.8
R18	10.260	70.8
R16	10.275	71.7

Temperature = 53.5°F      Relative Humidity = 100%

Dew Point = 53.5°F      Pressure = 990 mb

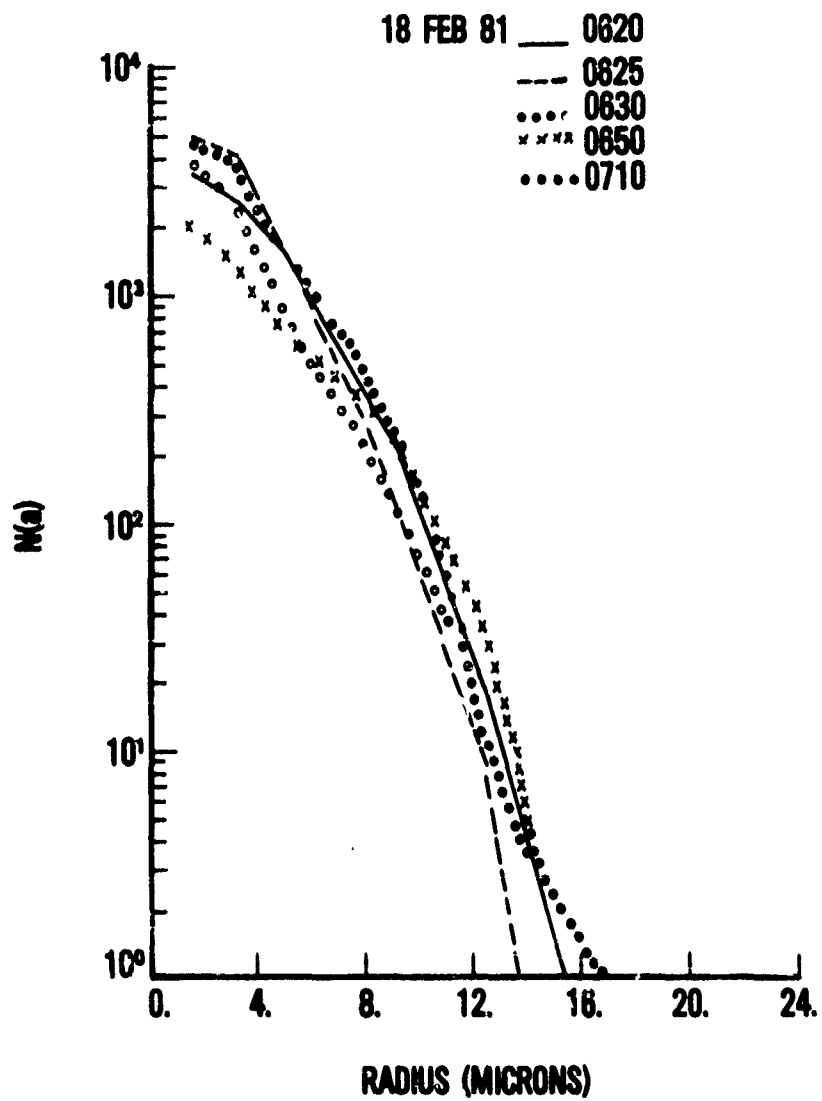


Figure 20. Particle Size Distributions for Dense Fog, 19 February 1981, 0620-0640 hrs

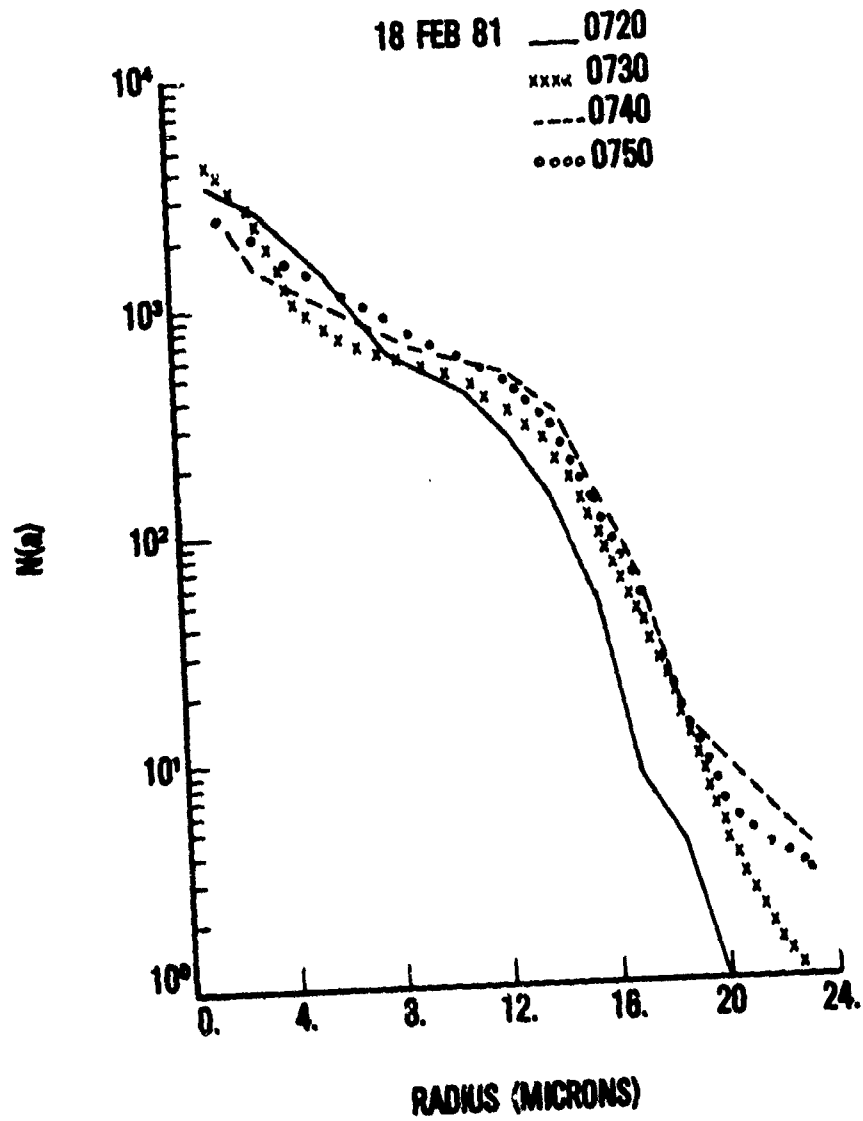


Figure 21. Particle Size Distributions for Extremely Dense Fog, 19 February 1981, 0720-0750 hrs.

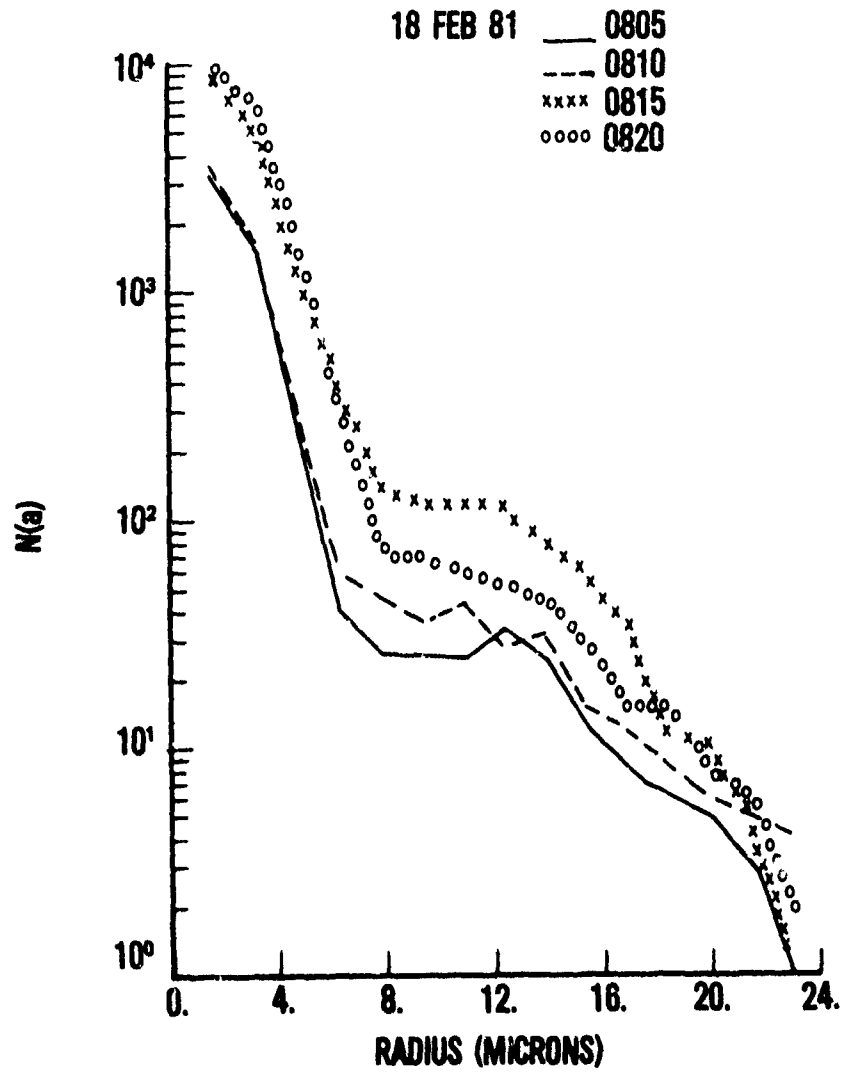


Figure 22. Particle Size Distributions for Selected Fogs, 19 February 1981, 0805-0820 hrs

TABLE 15  
 EXTINCTION OF 10.26  $\mu\text{m}$   $\text{CO}_2$  LASER RADIATION  
 WITH TIME, 19 FEBRUARY 1981

TIME	$\tau$ ( $10^{-3}$ )	$\sigma$ ( $\text{km}^{-1}$ )	$\sigma$ (dB/km)
0801	9.44	4.611	20.0
0802	9.19	4.69	20.4
0803	6.00	5.12	22.2
0804	5.41	5.22	22.7
0804	3.24	5.73	24.9
0805	2.51	5.49	26.0
0806	5.08	5.28	22.9
0807	10.60	4.54	19.7
0808	20.60	3.88	16.9
0809	2.50	5.99	26.0
0810	.66	7.32	31.8

TABLE 16

MEASURED TRANSMISSION AND EXTINCTION FOR  
SEVERAL CO<sub>2</sub> LASER LINES IN MEDIUM DENSITY  
FOG, 19 FEBRUARY 1981, 0811-0812 HOURS

LINE NO.	$\lambda$ ( $\mu\text{m}$ )	T ( $10^{-4}$ )	$\tau$ (dB/km)
P28	10.675	6.89	31.6
P26	10.653	6.68	31.8
P20	10.591	5.72	32.4
P18	10.571	5.46	32.6
P14	10.532	6.84	31.6
R18	10.260	5.95	32.3
R16	10.275	3.72	34.3

Temperature = 52.2°F      Relative Humidity = 100%

Dew Point = 52.2°F      Pressure = 990 mb

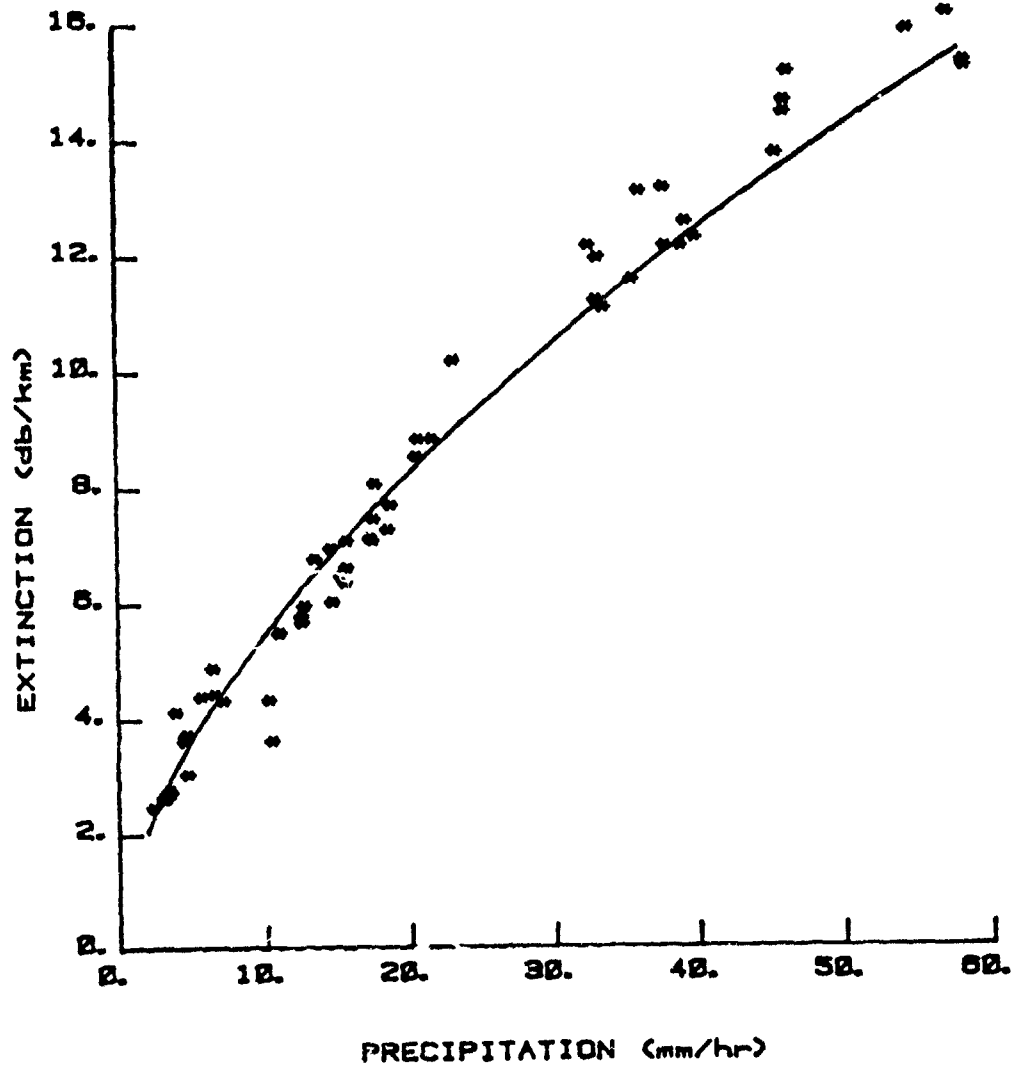


Figure 23. CO<sub>2</sub> Laser Extinction as a Function of Precipitation Rate for 10.6 μm Laser Radiation, 22 April 1981

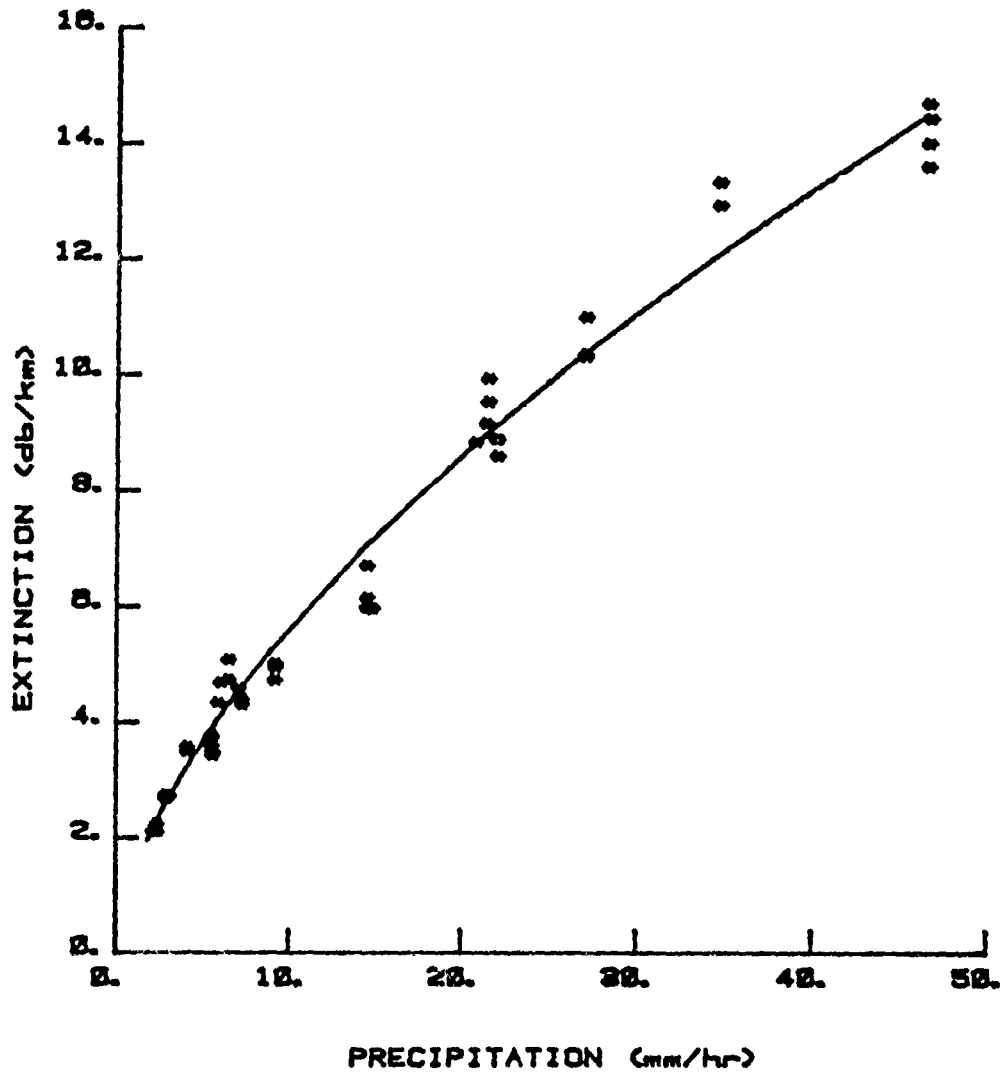


Figure 24. CO<sub>2</sub> Laser Extinction as a Function of Precipitation Rate for 10.6  $\mu$ m Laser Radiation 28 April 1981

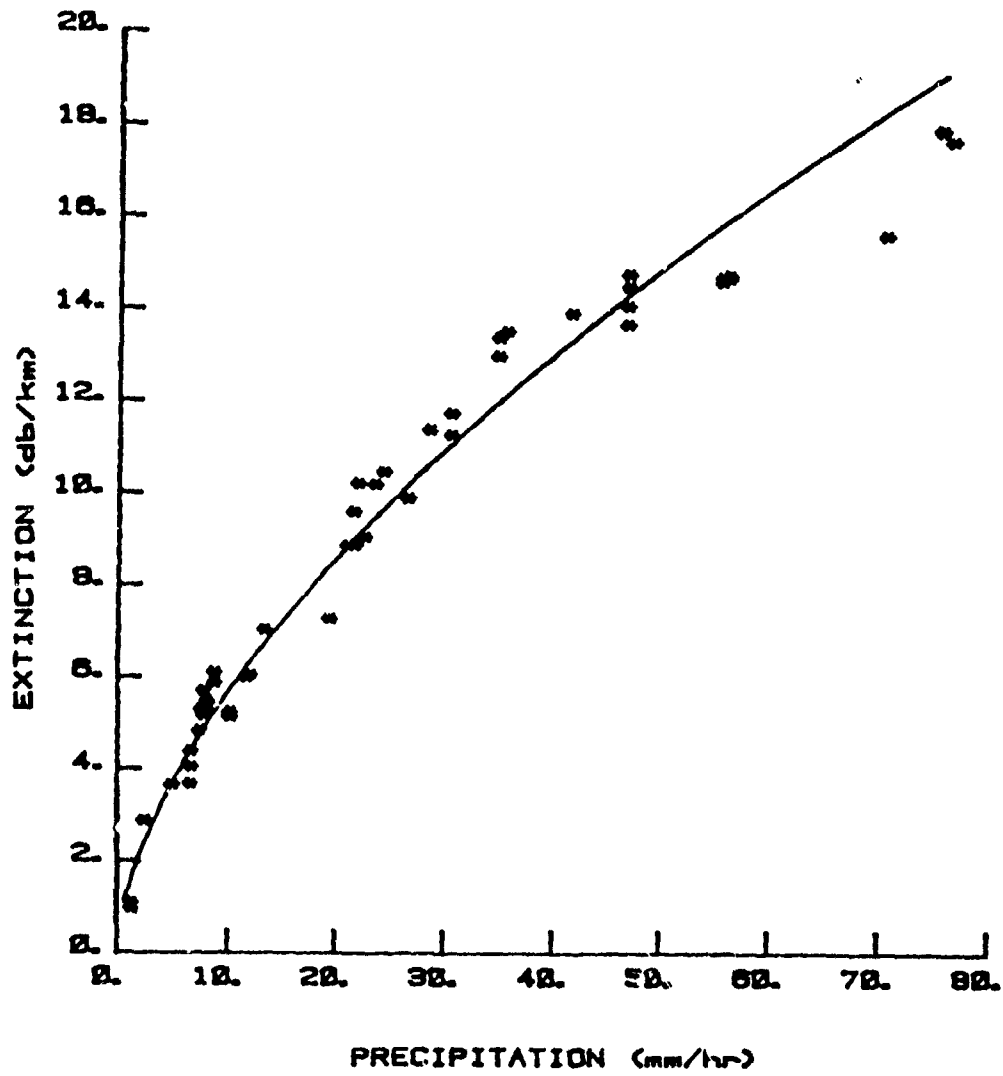


Figure 25. CO<sub>2</sub> Laser Extinction as a Function of Precipitation Rate for 10.6  $\mu$ m Laser Radiation, 29 April 1981

lines are a best fit model obtained by applying a nonlinear regression scheme to the measured data. Data obtained for April 22nd contains extinction values for rain rates up to 58 mm/hr, data for April 28th contains extinction values for data up to 46 mm/hr, and data for April 29th contains extinction values for data up to 75 mm/hr. The total number of points shown can be misleading, since points with the same coordinates will fall on top of each other. For example, in the data shown in Figure 25, five extinction values are plotted for rain rates near 75 mm/hr, yet only two data points are discernible at this value. The data illustrated on each of the plots was accumulated over several hours of measurement. Dynamic situations such as the moving in and moving out of rain showers were observed but not recorded. Data was only recorded when the monitored signal indicated a semi-stable optical path between transmitter and receiver.

The data obtained for April 29th contain the highest rain rates and also the maximum number of measured points (62 points). A best fit curve to the measured data gave the relationship

$$\sigma = 1.433P^{0.596} \text{ dB/km} \quad (141)$$

where P is the precipitation rate in mm/hr. The data for 22nd and 28th April were combined with data for the 29th and the result is plotted in Figure 26. Application of a nonlinear regression scheme yielded the equation

$$\sigma = 1.4P^{0.6} \text{ dB/km} \quad (142)$$

The same regression scheme was applied to rain extinction data published by Chen (Reference 54) and by Rensch and Long (Reference 55). The resulting curves are plotted alongside the curve given by Equation 142. Chen's calculations were obtained from data derived from laws and Parsons rainfall measurements. The rain rates were derived from measurements of drop size and drop terminal velocity (Reference 56). These quantities do not lend themselves to easy measurements. The relationship derived from Chen's results is given by

$$\sigma_{\lambda} = 1.085P^{0.659} \text{ dB/km} \quad (143)$$

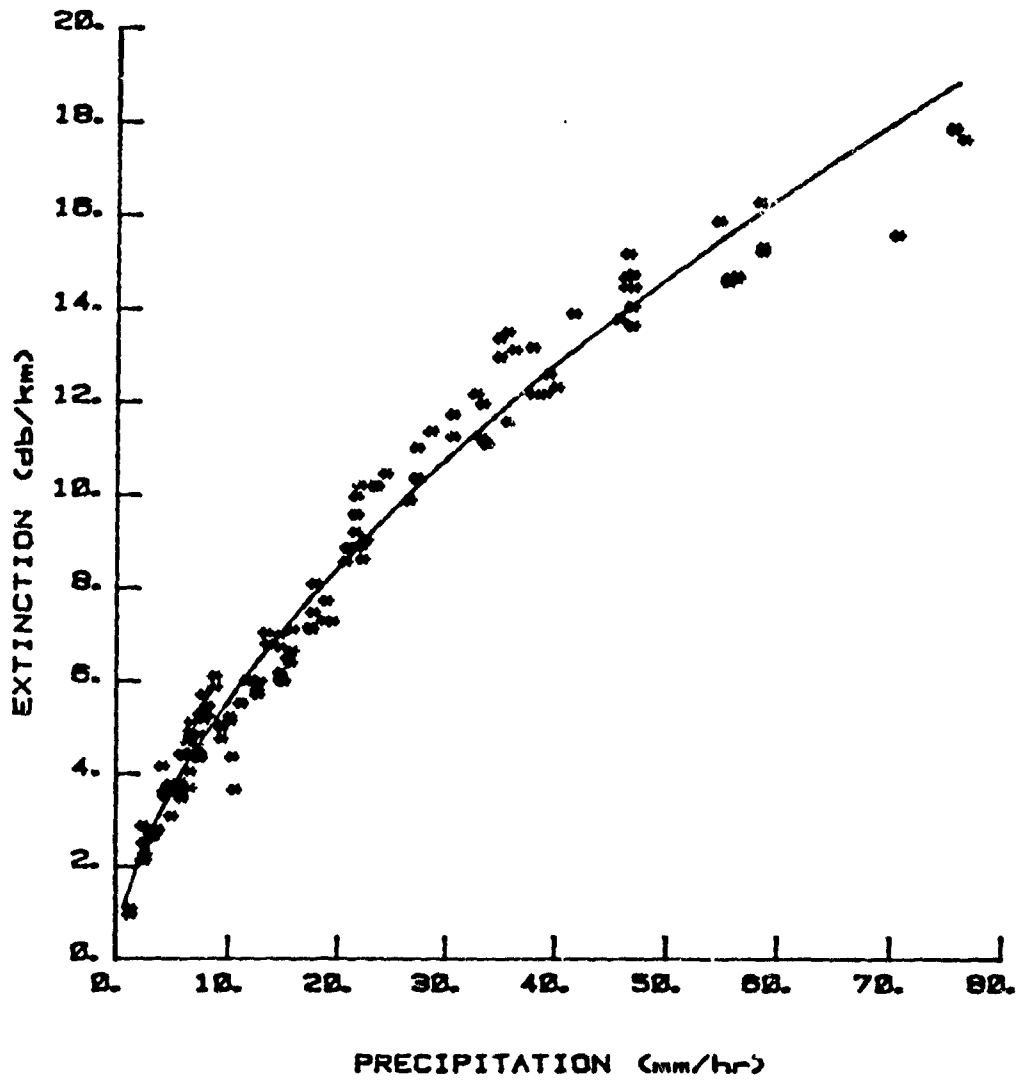


Figure 26. Extinction of CO<sub>2</sub> Laser Radiation as a Function of Precipitation Rate. Data Includes All Data Points from Figures 23, 24, and 25

while that derived from Rensch and Long's results is given by

$$\sigma_{\lambda} = 1.84P^{0.501} \text{ dB/km} \quad (144)$$

Equation 143 was derived from data with rain rates up to 50 mm/hr. The extension to 75 mm/hr was done by the computer, based on the model given by Equation 143. Data from Rensch and Long was obtained from direct precipitation measurements. Their results follow nicely those of Chen's up to rain rates of 25 mm/hr, but then it begins to drop off. Extinction values as a function of rain rates for several wavelengths are tabulated in Table 18 for a rain rate of 1.82 mm/hr for data taken on April 22nd and in Table 19 for rain rates of 1.8, 8.5, and 12.0 mm/hr for data taken on April 29th. Whatever differences are observed are due to the differences in molecular contributions and to changes in the atmospheric path during the time of measurement.

## 5. HAZE

Due to the uncertainty in the aerosol refractive index, extinction calculations yield very uncertain results. Depending on the relative humidity, dry aerosols can grow up to ten times their normal size (Reference 57). The size distribution given by Junge's model, with the calculated growth rate in humidity is shown in Figure 28. Three separate distributions are shown for three different type atmospheres. Curve 1 is for a continental atmosphere, Curve 2 for an oceanic atmosphere, and Curve 3 is for the average sea spray (NaCl). For continental aerosols, it is very obvious that as the particle grows in size, its refractive index changes. For water soluble aerosols, the refractive index has been measured to be approximate to that of NaCl (Reference 58). As the particle grows with humidity, the refractive index varies in values to that in between NaCl and H<sub>2</sub>O. Therefore, computations of extinction using Mie Scattering theory yield very rough approximations unless the exact value of the aerosol refractive index is known. This is illustrated in Tables 19 and 20. Table 19 corresponds to the aerosol distribution shown in Figure 29 and Table 20 corresponds to the aerosol distribution shown in Figure 30. The aerosol extinction was computed using a refractive index approaching that of NaCl ( $n = 1.45 - .154j$ ) and that of H<sub>2</sub>O ( $n = 1.185 - .0662j$ ). Comparing the extinction due to water soluble aerosols ( $\sigma_s$ )

TABLE 17

EXTINCTION OF CO<sub>2</sub> LASER LINES FOR A CONSTANT  
RAIN RATE OF 1.82 mm/HR, 22 APRIL, 1935 HOURS

LINE NO.	$\lambda$ ( $\mu\text{m}$ )	$\sigma$ (dB/km)
P28	10.675	2.78
P22	10.611	2.72
P20	10.591	2.67
P18	10.571	2.69
P14	10.532	2.68
R16	10.275	2.82
R18	10.260	2.96

Temperature = 50°F

Relative Humidity = 99%

Dew Point = 59.5°F

Pressure = 990 mb

TABLE 18

EXTINCTION OF SEVERAL CO<sub>2</sub> LASER LINES FOR  
 CONSTANT RAIN RATES OF 1.8, 8.5, and 12 mm/HR,  
 20 APRIL 1981

LINE NO	$\lambda$ $\mu\text{m}$	EXTINCTION		
		P = 1.82	P = 8.5	P = 12
P28	10.675	2.78	5.65	5.86
P22	10.611	2.74	5.47	6.21
P20	10.591	2.69	5.69	6.18
P18	10.571	2.61	5.91	6.12
P14	10.532	2.65	5.73	5.99
R16	10.275	--	5.73	5.73
R18	10.260	3.04	--	6.30

TABLE 19

COMPARISON OF AEROSOL EXTINCTION HAVING AN ASSUMED COMPLEX INDEX OF  $H_2O$  AND AN ASSUMED COMPLEX INDEX OF  $NaCl$  (DATA TAKEN 27 JULY 1981)

$r_m$ $\mu m$	$\sigma_w$ $km^{-1}$	$\sigma_s$ $km^{-1}$	$\sigma_m$ $km^{-1}$	$\sigma_F$ $km^{-1}$	$\Delta\sigma$ $km^{-1}$
.46	.088	.242	.585	.533	.052
.49	.090	.247	.588	.533	.058
.46	.115	.316	.588	.533	.058

Temperature = 73°F

Relative Humidity = 100%

Dew Point = 69.5°F

Absolute Humidity = 17.5  
gr/m<sup>3</sup>

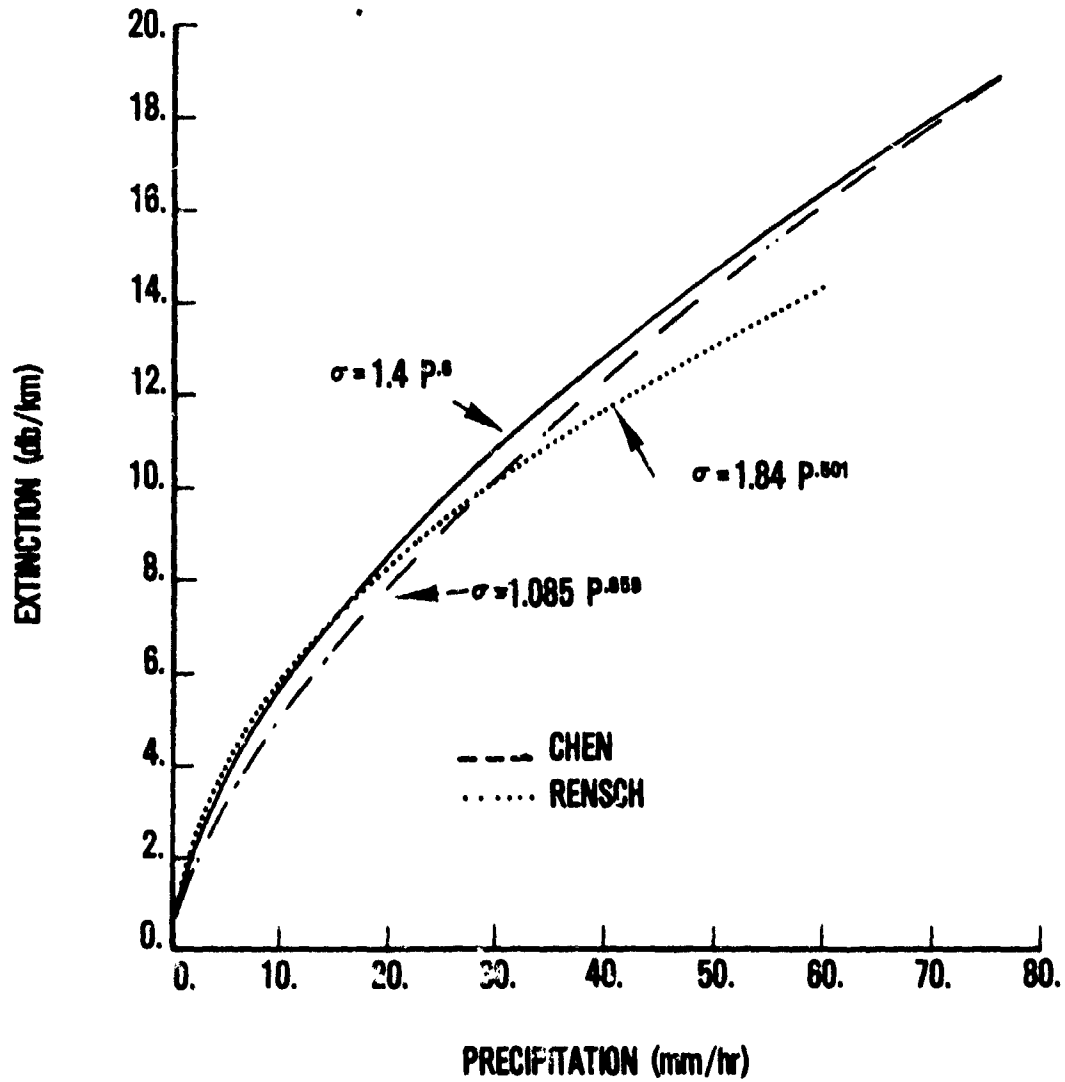


Figure 27. Best Fit Models for Data on Figure 26, Laws and Parscns as Reported by Chen, and Measurements Conducted by Rensch

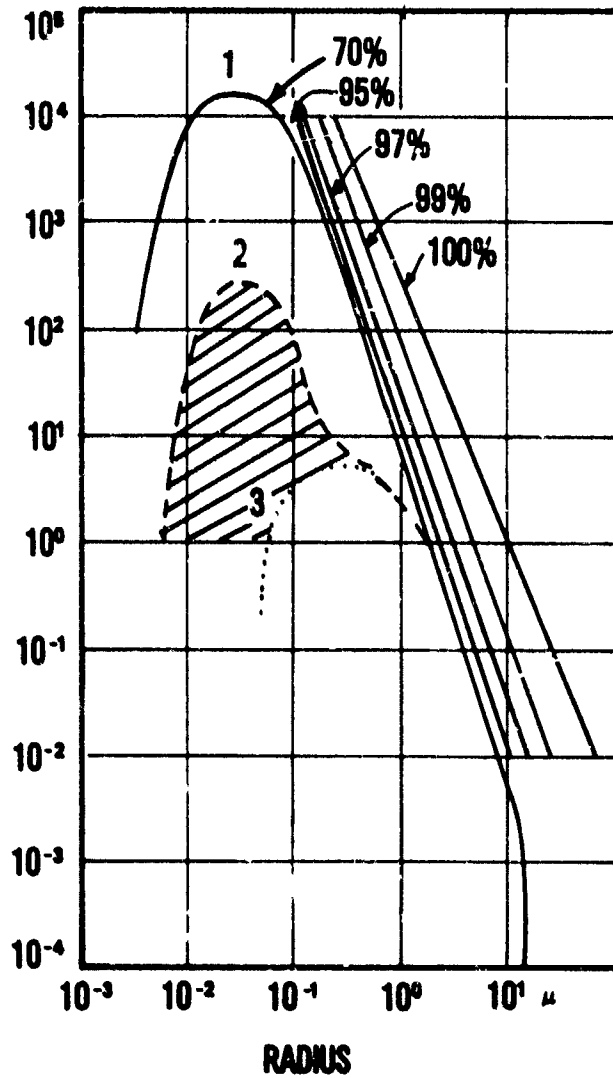


Figure 28. Model Size Distribution for Atmospheric Aerosols, Adapted from Reference 27, p. 124  
 The hatched area between Curves 2 and 3 represents the non-sea spray component over the ocean. The straight lines indicate the shift of the continental log radius number distributions curve due to particle growth by humidity for mixed particles of about 20% soluble material.

TABLE 20

COMPARISON OF AEROSOL EXTINCTION HAVING AN ASSUMED COMPLEX INDEX OF  $H_2O$  AND AN ASSUMED COMPLEX INDEX OF NaCl (DATA TAKEN 5 AUGUST 1981)

$r_m$ $\mu m$	$\sigma_{w_1}$ $km^{-1}$	$\sigma_s$ $km^{-1}$	$\sigma_m$ $km^{-1}$	$\sigma_F$ $km^{-1}$	$\Delta \sigma$ $km^{-1}$
.43	.049	.135	.536	.498	.038
.42	.042	.132	.535	.498	.037
.42	.032	.096	.531	.498	.033

Temperature = 68.4°F

Relative Humidity = 88.8%

Dew Point = 68.4°F

Absolute Humidity = 18.8  
gr/m<sup>3</sup>

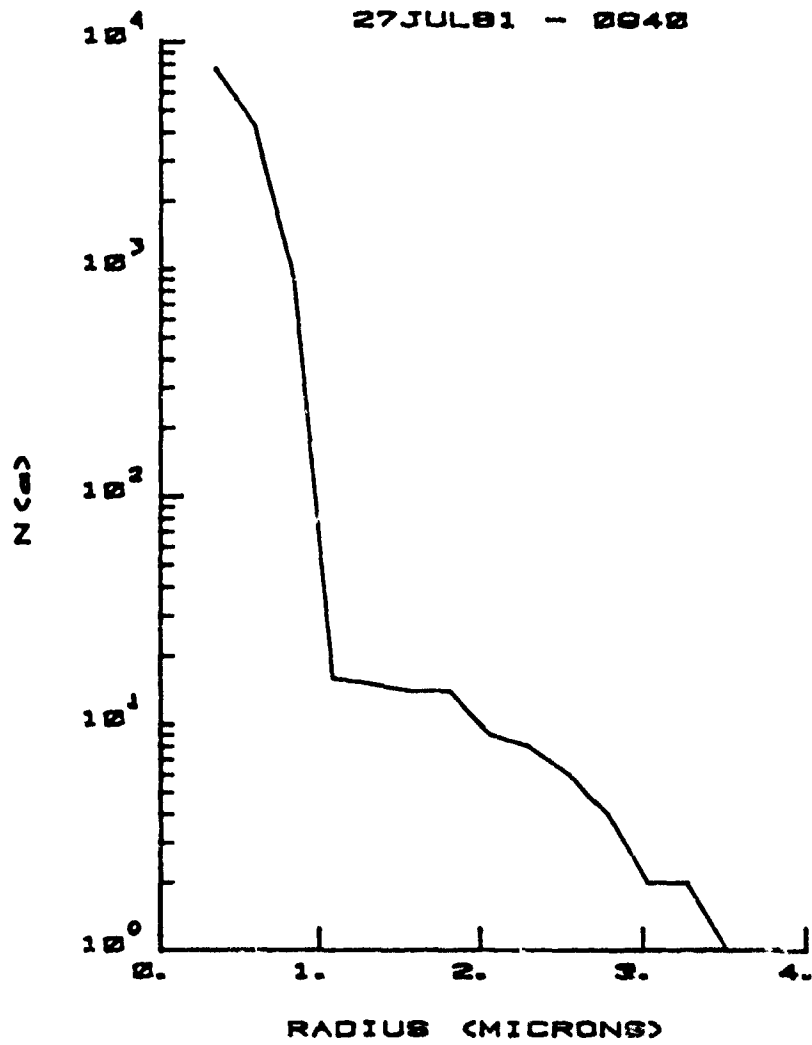


Figure 29. Aerosol Size Distributions, Hazy Weather, 27 July 1981

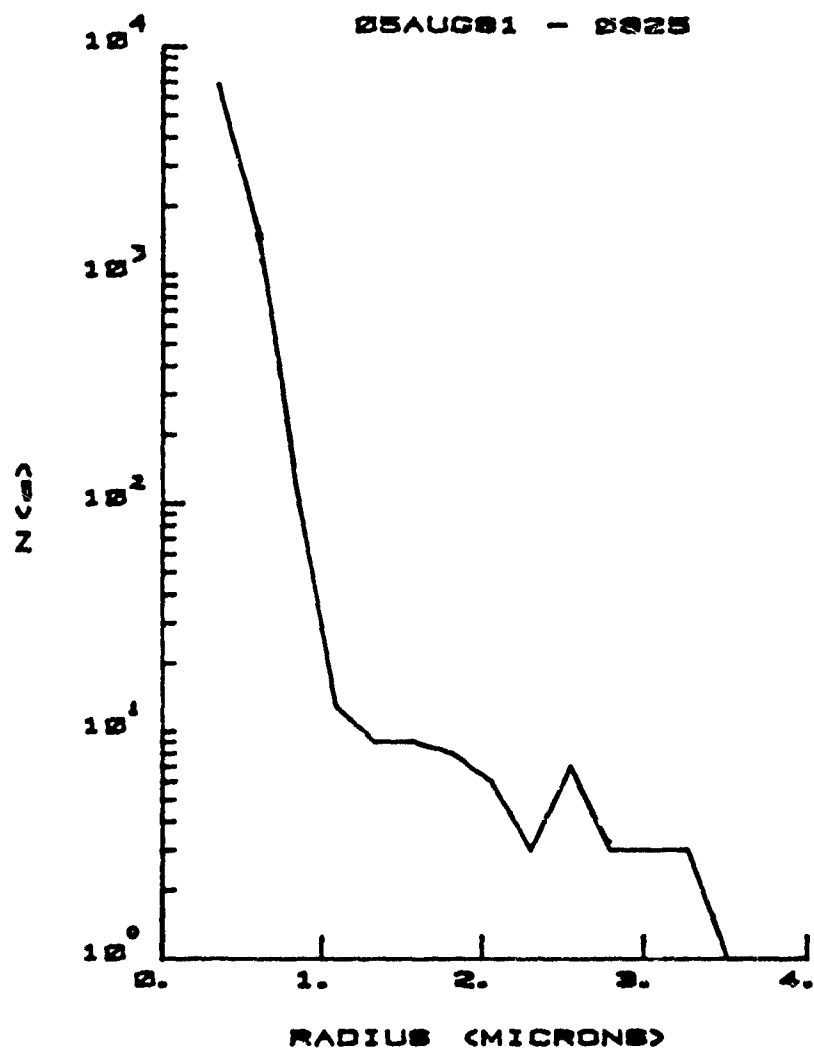


Figure 30. Aerosol Size Distributions, Hazy Weather, 5 August 1981

to that of water aerosols ( $\sigma_w$ ), it is seen that a difference in extinction of 2.7 to 1, or greater, exists in all cases. The aerosol extinction values were computed for a wavelength of 10.6 microns. The difference between the molecular extinction and the measured extinction is given by  $\Delta\sigma$ .

Two factors must be remembered in this comparison. The most important one is that a very few number of large particles (4 or 5) can unduly influence the aerosol extinction calculated. This is clearly shown in Table 21. If the number of particles measured with radius 3.373  $\mu\text{m}$  would have been five instead of one, the extinction for that size radius would be 0.009 instead of 0.0018. The missing of only two particles of radius 3.62  $\mu\text{m}$  results in the omission of 0.045 from the aerosol extinction computed. As can be seen from Table 21, particles with size radius less than 0.35  $\mu\text{m}$  do not contribute significantly to the aerosol extinction. Although the lower number density has a larger number of particles, the significant difference to the contribution of extinction lies almost entirely to the small increase on the density of particles with mean radii of 0.612 and 0.866 microns. The second factor is due to the error uncertainty of the particle measuring system in measuring sizes at the low range of the instrument. A third possible source of difference could be in the computed value of  $\sigma_m$  given by the FASCODE model. As mentioned earlier in Section III, the molecular extinction on humid, summer days is due mostly to the contribution of the water vapor continuum. The exactness and source of the contribution of the water vapor continuum is still being debated.

Measured transmission values are compared with calculated values for several wavelengths in Tables 22 and 23. Aerosol size distributions corresponding to extinction data of Tables 24 and 25 are plotted in Figures 29 and 30. The difference in transmission for the  $P_{20}$  line is 0.039 for the 0940, July 27th measurement. However, the loss in transmission due to aerosol extinction ( $\sigma_a = .09$ ) is approximately 0.10 and this leaves a factor of 0.06 unaccounted for. A plot of the FASCODE output corresponding to the data tabulated in Table 23 is shown in Figure 31.

TABLE 21

COMPUTATION OF EXTINCTION FOR PARTICLES OF  
RADIUS  $r(I)$  AND DENSITY  $dN(r)/dr$  (5 AUGUST  
1981, 0800 HOURS)

$r(I)$	$N(I)$	$dN(r)/dr$	$\sigma(I)$
.353	8132	71.900	.0010
.612	2409	21.300	.0249
.866	363	3.210	.0093
1.118	13	.115	.0005
1.369	7	.062	.0005
1.620	6	.053	.0008
1.871	5	.044	.0011
2.121	4	.035	.0014
2.372	4	.035	.0021
2.622	3	.027	.0022
2.872	2	.018	.0020
3.122	1	.009	.0013
3.373	1	.009	.0018

TABLE 22

MEASURED AND COMPUTED TRANSMISSION FOR  
SEVERAL CO<sub>2</sub> LASER LINES IN HOT, HUMID,  
HAZY WEATHER, 27 JULY 1981, 0940 HOURS

LINE NO.	$\lambda$ $\mu\text{m}$	$T_m$ (measured)	$T_c$ (computed)	$\Delta T$
P28	10.675	.571	.607	.036
P26	10.653	.566	.602	.036
P22	10.611	.556	.590	.034
P20	10.591	.548	.587	.039
P18	10.571	.554	.590	.036
R16	10.275	.561	.595	.034
R18	10.260	.573	.608	.035

Temperature = 20.21°C      Relative Humidity = 100%

Dew Point = 20.21°C      Absolute Humidity = 17.5  
gr/m<sup>3</sup>



TABLE 24

TRANSMISSION IN SNOW FOR SEVERAL CO<sub>2</sub> LINES.  
 MISSING DATA DUE TO THE INABILITY TO OBTAIN  
 STABLE LINES IN THE SHORT TIME REQUIRED

LINE	$\lambda$	T <sub>1</sub>	T <sub>2</sub>	T <sub>3</sub>
P28	10.675	.122	.051	--
P26	10.673	.122	.051	.225
P24	10.632	--	--	--
P22	10.611	--	--	--
P20	10.591	.119	.049	.186
P18	10.571	.120	.049	.189
P14	10.532	.118	.047	.187
R18	10.260	.116	.048	.190
R16	--	--	.044	.173

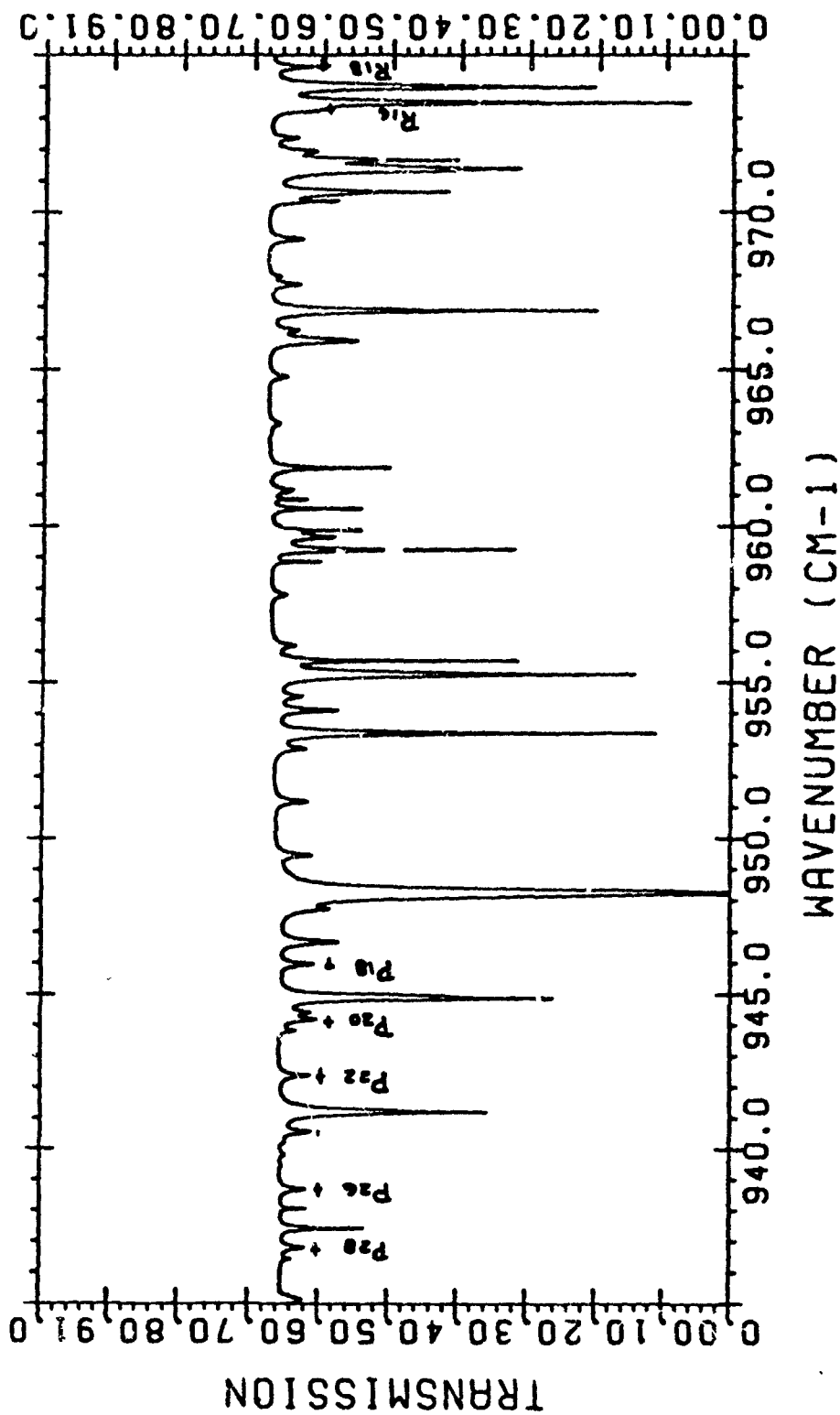


Figure 31. Plot of FASCODE Output for Weather Conditions of T = 22.75°C, Dew Point = 20.8°C, and Relative Humidity = 88.8%. The Markers Indicate Values Measured Under Heavy Haze Conditions

58-24-85-1-6

6. SNOW

No reliable means exist at our facility for categorizing snow. Although visibility is not a good tool for this purpose, it is the only one at our disposal. Three sequences of transmission measurements through snow are shown in Table 24. The three transmissions,  $T_1$ ,  $T_2$ , and  $T_3$  correspond to approximate visibilities of 1.5, 1.2, and 1.7 km, respectively. All three were taken under what was considered light snowfall condition.

## SECTION VII

## CONCLUSIONS

Results show that extinction of  $\text{CO}_2$  laser radiation in dense fog may be determined to a good approximation by the relation  $\sigma = 147W$ , where  $W$  is the liquid water content of the fog distribution. With few exceptions, results obtained by use of this approximation give results which are within 7% of results obtained by use of Mie Scattering theory. The approximation seems to be good for extinction values greater than 9 dB/km.

Extinction by dense fog can easily exceed the dynamic range of the measuring instrument. The probability of this occurring is better than 0.5. Use of higher sensitivity detectors does not appreciably change this number when dealing with extinction in excess of 70 dB/km.

Extinction by rain with precipitation rates up to 75 mm/hr was measured. Application of an empirically derived model gives good results with data obtained by other workers. The derived model can be used to obtain extinction from knowledge of the precipitation rate without need for measuring the rain drop size and terminal velocity. Measured extinction in heavy rainfall was found to be an order of magnitude less than measured extinction in heavy fog.

Extinction by summer aerosols is difficult to calculate due to the uncertainty on the composition of the aerosols. An upper and a lower bound on the aerosol extinction has been calculated using the complex index of NaCl and  $\text{H}_2\text{O}$ , respectively.

Comparison of measured distributions to those given by models reveals that these models are only applicable for those cases where smooth continuous distributions are measured. Unfortunately, this type of distribution was seldom observed, and in most instances, smoothing approximations can only be applied to less than 25% of the measured distributions. No smooth haze distributions were observed. This indicates that models for size distributions can give serious errors when used in computing aerosol extinction and should be used cautiously.

Extinction measurements for  $\text{CO}_2$  laser propagation under adverse weather clearly points out that extinction is at best a very weak function of wavelength. This can be seen by looking at the extinction cross section  $Q(x)$  that depends on the ratio of  $\lambda/r$  of the Mie size parameter  $x = 2\pi\lambda/r$ . For  $\text{CO}_2$  laser wavelengths, the departure from  $10.6 \mu\text{m}$  is not that significant in terms of wavelength ( $\pm 0.4 \mu\text{m}$ ), but the true wavelength dependence of the extinction coefficient has to be examined in terms of the complex refractive index of water. For clouds with a mode radius of  $4.0 \mu\text{m}$ , Deirmendjian gives the extinction at  $10.0 \mu\text{m}$  to be  $11.18 \text{ km}^{-1}$  and  $10.10 \text{ km}^{-1}$  at  $11.5 \mu\text{m}$  (see p. 189 of Reference 34). This is approximately a  $\pm 5\%$  deviation from the  $10.6 \mu\text{m}$   $\text{CO}_2$  wavelength of interest.

A final conclusion is that a  $\text{CO}_2$  laser radar with a 3 dB/km performance has very limited utility in fog (except for light winter fogs), may be used in rain with precipitation rates of 25 mm/hr at ranges of 1 kilometer or less, and has little utility in snow except for very light snowfall conditions.

## APPENDIX A

CORRECTION FACTORS TO THE VAN de Hulst  
APPROXIMATIONS TO THE MIE EXTINCTION FORMULA

The Deirmendjian correction factors to the Van de Hulst approximations are given by (see Reference 21, page 30).

$$D_1 = \frac{(n_1 - 1)^2}{1.632n_1} (S + 1) + \frac{0.2\rho - n_1 + 1}{(n_1 - 1)S}, \quad \rho \leq 5(n_1 - 1) \quad (\text{A-1})$$

$$D_2 = \frac{n_1 - 1}{8.16n_1} (S + 1)\rho, \quad 5(n_1 - 1) \leq \rho \leq \frac{4.08}{1 + 3\tan\beta} \quad (\text{A-2})$$

$$D_3 = \frac{(n_1 - 1)(S + 1)}{2n_1(1 + 3\tan\beta)}, \quad \frac{4.08}{1 + 3\tan\beta} \leq \rho \leq \frac{4.08}{1 + \tan\beta} \quad (\text{A-3})$$

$$D_4 = \frac{2.04(n_1 - 1)(S + 1)}{n_1 S}, \quad \rho > \frac{4.08}{1 + \tan\beta} \quad (\text{A-4})$$

where

$$S = 1 + 4\tan\beta + 3\tan^2\beta \quad (\text{A-5})$$

PRECEDING PAGE MUST BE FILMED

$$\rho = 4\pi r / \lambda (n_1 - 1) \quad (\text{A-6})$$

$$\beta = \tan^{-1} [n_1 / (n_2 - 1)] \quad (\text{A-7})$$

$$x = 2\pi r / (n_1 - 1) \quad (\text{A-8})$$

For  $n_1 = 1.185$ ,  $n_2 = .0662$  and  $\lambda = 10.6$  microns, Equations A-5 through A-8 reduce to

$$S = 2.816$$

$$\rho = 0.2193r$$

$$\beta = 0.358$$

$$x = 0.0785r$$

where the radius  $r$  is expressed in microns. Using the above values, it is found that the correction factors and their ranges are,

$$D_1 = 0.0675 + 1.92(.0439r - 0.185) \quad r \leq 4.21 \quad (\text{A-9})$$

$$D_2 = 0.161r \quad 4.21 < r \leq 8.97 \quad (\text{A-10})$$

$$D_3 = .1434 \quad 8.97 < r \leq 13.7 \quad (\text{A-11})$$

$$D_4 = .5158/r \quad r > 13.7 \quad (\text{A-12})$$

The extinction value is obtained from

Use of Equations A-10 through A-12 in conjunction with Equation 85 gives extinction values which are within 6% of exact values obtained from Mie formula calculations. For  $r = 0.577$  microns, use of  $D_1$  gives an error of 37%, and at the upper end of its useful approximation it gives a 6.1% error for  $r = 3.51$  microns.

$$Q_e = Q_e(1 + D) \quad (\text{A-13})$$

In order to reduce the error, the Deirmendjian correction factors were modified to give better approximations when used with the Van de Hulst equation for extinction. To achieve this, it was necessary to break down the approximation factors in the range  $0 < r \leq 4.0$  into two different factors with ranges  $0 < r < 1$  and  $1 \leq r < 4.0$ . The correction factors and their useful range are given below, where every attempt was made to retain the original form of the Deirmendjian factors.

$$D_0 = \frac{(n_1 - 1)^2 (S + 4.6)}{1.44n_1 r^2} - \frac{(n_1 - 1) - \rho r^{-\frac{1}{2}}}{5(n_1 - 1)S} \quad r < 1 \quad (\text{A-14})$$

$$D_1 = \frac{(n_1 - 1)^2 (S + 1)r^{\frac{1}{2}}}{3.673n_1} + \frac{.137\rho r^4 - (n_1 - 1)}{(\ln r)^{\frac{1}{2}}} \quad 1 \leq r < 4.0 \quad (\text{A-15})$$

$$D_2 = \frac{(n_1 - 1)(S + 1)\rho r^2}{8.165n_1} \quad 4.0 \leq r \leq 7.0 \quad (\text{A-16})$$

$$D_3 = \frac{1.794(n_1 - 1)}{(1 + 3 \tan \beta)} \quad 7.0 \leq r \leq 13.7 \quad (\text{A-17})$$

$$D_4 = \frac{1.89(n_1 - 1)(S + 1)}{n_1 S \ln r} \quad r \geq 13.7 \quad (\text{A-18})$$

AFWAL-TR-81-1280

Use of these factors in conjunction with Equation A-13, give extinction values which are within 1% of values obtained from exact Mie calculations.

## APPENDIX B

## CONVERSION OF EXTINCTION UNITS

From  $\text{km}^{-1}$  to dB/km

The extinction coefficient  $\sigma_\lambda$  can also be expressed in decibels (dB) by use of the standard definition

$$\begin{aligned} \text{dB} &= 10 \log (I_0/I) \\ &= 10 \log (1/T) \\ &= 10 \log O \end{aligned} \quad (\text{B-1})$$

where  $O$  is the opacity of the medium. The optical density of the medium is related to opacity by the relation

$$D = \log (1/T) \quad (\text{B-2})$$

or

$$T = 10^{-D} \quad (\text{B-3})$$

Substituting Equation B-2 in Equation B-1 one obtains the relation

$$\text{dB} = 10D$$

or

$$D = .1\text{dB} \quad (\text{B-4})$$

Using a unit path length (extinction coefficient has units of  $\text{km}^{-1}$ ), the atmospheric transmittance is given by

$$T = e^{-\sigma_\lambda} \quad (\text{B-5})$$

Comparing Equation B-3 and Equation B-5 one sees that

$$e^{\sigma_\lambda} = 10^D \quad (\text{B-6})$$

Taking logs of both sides of Equation B-6 one obtains,

$$\begin{aligned}\sigma_{\lambda} &= D \ln 10 \\ &= 2.302585 D \quad (B-7)\end{aligned}$$

Substitution of Equation B-4 in Equation B-7 yields

$$\sigma_{\lambda} = 0.230585 \text{ db} \quad (B-8)$$

The attenuation loss per kilometer is easily obtained from Equation B-8

$$\sigma (\text{dB/km}) = 4.3367936 \sigma_{\lambda} (\text{km}^{-1}) \quad (B-9)$$

## APPENDIX C

## TEST SITE

Because of safety considerations, the propagation path had to be located in a controlled area with a requirement for beam termination on the ground in case the laser beam missed the receiving van. The site chosen was adjacent to an old runway on Area B, Wright-Patterson AFB (Figure C-1). The receiver was positioned off the runway so as to eliminate the thermal heat emanated from the cement structure. Because the wind normally blows from the southeast, the heat from the runway would often be carried into the optical path creating extreme turbulence fluctuations which had to be dealt with (see Section V). Because of the isolated site, diesel power generators were used. These generators were very unreliable, and at times impossible to start when the temperature fell below the freezing point. Since the generators could not be left running continuously, the heaters in the receiver van were normally off. This resulted in condensation forming on the 24-inch mirror whenever the dew point was high and the mirror was colder than the surrounding air. Whenever this happened, it was necessary to wait a few days until the mirror temperature rose higher than the surrounding air temperature before cleaning of the mirror was possible. Eventually, gas heaters were installed and the problem resolved.

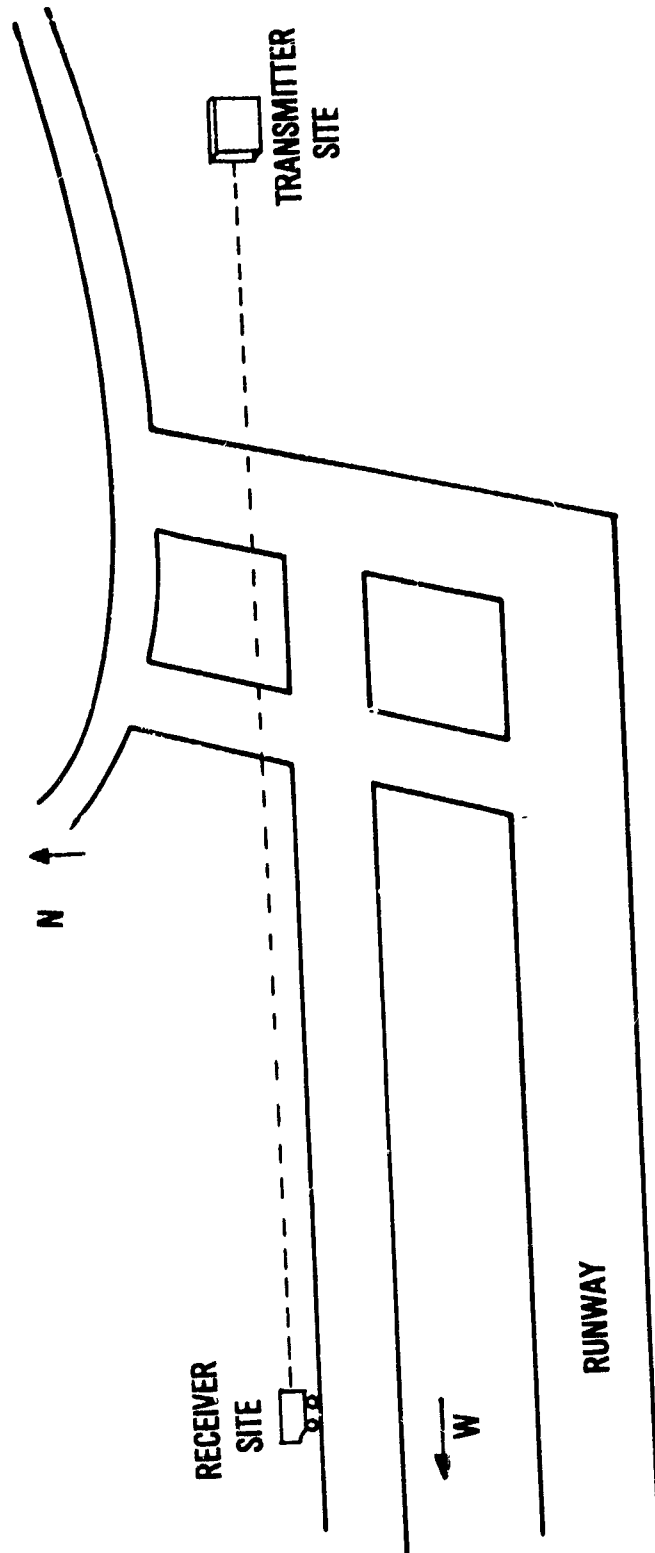


Figure C-1. Test Site for CO<sub>2</sub> Laser Extinction Measurements

## REFERENCES

1. E. B. Wilson, J. C. Cross, and J. C. Decius, Molecular Vibrations: Theory of Infrared and Raman Vibrational Spectra, McGraw-Hill Book Company, 1955, pp. 273-284.
2. L. Pauling and E. B. Wilson, Introduction to Quantum Mechanics, McGraw-Hill Book Company, Inc., New York, 1935, pp. 282-290.
3. H. H. Nielsen, Physical Review, Volume 60, 1941, p. 806.
4. B. T. Darling and D. M. Dennison, Physical Review, 1939, pp. 128-129.
5. D. M. Dennison, Physical Review, Volume 12, No. 3, 1940, pp. 175-213.
6. G. H. Herzberg, Infrared and Raman Spectra, D. Van Nostrand Company, Inc., New York, 1945, pp. 45-50.
7. S.C. Wang, Physical Review, Volume 34, 1929, p. 243.
8. R. E. Meredith, T. Chang, F. G. Smith, and D. R. Woods, Investigations in Support of High Energy Laser Technology, Science Applications, Inc., Technical Report SAI-75-001-AA.
9. Adel and D. M. Dennison, Physical Review, Volume 43, 1935, p. 716.
10. R. A. McClatchey, W. S. Benedict, S. A. Clough, et al., AFCRL Atmospheric Absorption Line Parameters Compilation, Report AFCRL-TR-73-0096, Air Force Cambridge Research Laboratories, Bedford, Mass, 26 January 1973.
11. V. E. Zuev Radiation of Visible and Infrared Radiation in the Atmosphere, Israel Program for Scientific Translations, John Wiley & Sons, Inc., New York, 1974.
12. D. Anding, Band Model Methods for Computing Atmospheric Molecular Absorption, Report No. 7142-21-T, Willow Run Laboratories, The University of Michigan, Ann Arbor Michigan, 1967.
13. G. Townes and R. Schawlow, Microwave Spectroscopy. McGraw-Hill Book Company, Inc., 1955, p. 342.
14. P. S. Varanasi, S. Chou, and S. S. Penner, Journal Quantum Spectroscopy and Radiative Transfer, Volume 8 (1968), p. 1537.
15. K. Bignell, F. Saiedy, and P. Sheppard, "On the Atmospheric Infrared Continuum," Journal of the Optical Society of America, Vol. 53, No. 4 (April 1963), p. 466.

## REFERENCES (Cont'd)

16. K. Bignell, "The Water-Vapor Infrared Continuum," Quarterly Journal of the Royal Meteorological Society, Volume 96 (1970), pp. 340-403.
17. V. N. Arefev and V. I. Dianov-Klokov, "Attenuation of 10.6  $\mu\text{m}$  Radiation by Water Vapor and the Role of ( $\text{H}_2\text{O}_2$ ) Dimers," Journal of the Optical Society of America (May 1977), pp. 488-492.
18. J. McCoy, D. Rensch, and R. Long, "Water Vapor Continuum Absorption of Carbon Dioxide Laser Radiation near 10  $\mu\text{m}$ ," Applied Optics, Volume 8, No. 7 (July 1969), pp. 1471-1478.
19. J. C. Peterson, M. D. Thomas, R. J. Nordstrom, et al., "Water Vapor-Nitrogen Absorption at  $\text{CO}_2$  Laser Frequencies," Applied Optics Volume 18, No. 6 (March 1979), pp. 834-840.
20. R. E. Roberts, J. E. Selby, and L. M. Biberman, "Infrared Continuum Absorption by Atmospheric Water Vapor," Applied Optics, Volume 15, No. 9 (September 1976), pp. 2085-2090.
21. S. A. Clough, H. J. Smith, D. J. Dube, et al., FASCODE-Fast Atmospheric Signature Code, Report AFGL-TR-78-0081, 1978.
22. D. Deirmendjian, Electromagnetic Scattering on Spherical Polydispersions, Elsevier Press, New York, 1969, pp. 28-35.
23. H. C. Van de Hulst, Light Scattering by Small Particles, John Wiley and Sons, Inc., New York, 1957.
24. D. Deirmendjian, "Atmospheric Extinction of Infrared Radiation," Quarterly Journal of the Royal Meteorological Society, Volume 86 (1960), pp. 377-381.
25. G. Hale and M. Querry, "Optical Constants of Water in the 200 nm to 200  $\mu\text{m}$  Wavelength Region," Applied Optics, Volume 12 (1973), pp. 555-563.
26. M. Centeno, "The Index of Liquid Water in the Near Infrared Spectrum," Journal of the Optical Society of America, Volume 31 (March 1941), pp. 244-247.
27. C. E. Junge, Air Chemistry and Radioactivity, Academic Press, New York, 1963.
28. G. Ward, K. M. Cushing, R. D. McPeters, and A. Green, "Atmospheric Aerosol Index of Refraction and Size-Altitude Distribution from Bistatic Laser Scattering and Solar Auerole Measurements," Applied Optics, Volume 12, No. 11 (1973), pp. 2585-2592.

## REFERENCES (Cont'd)

29. V. E. Zuev, loc. cit. p. 170.
30. G. Ward, K. M. Cushing, R. D. Peters, and A. E. Green, loc. cit.
31. D. Deirmendjian, "Scattering and Polarization Properties of Water Clouds and Haze in the Visible and Infrared," Applied Optics, Volume 3, No. 2 (February 1964), pp. 187-195.
32. T. S. Chu and D. C. Hogg, "Effects of Precipitation on Propagation of 0.63, 3.5, and 10.6 Microns," The Bell System Technical Journal (May-June 1968), pp. 723-759.
33. D. B. Rensch and R. K. Long, "Comparative Studies of Extinction and Backscattering by Aerosols, Fog, and Rain at 10.6  $\mu\text{m}$  and 0.63  $\mu\text{m}$ ," Applied Optics, Volume 9, No. 7 (July 1970), pp. 1563-1573.
34. J. O. Laws and A. Parsons, "The Relation of Raindrop Size to Intensity," Transactions American Geophysical Union, Volume 24 (1943), pp. 452-460.
35. H. Goldstein, Propagation of Short Radio Waves Chapter 8, Edited by D. E. Kerr, McGraw-Hill Book Co., New York, 1951.
36. J. S. Marshall and W. M. Palmer, "The Distribution of Raindrops with Size," Journal of Meteorology, Volume 5 (1948), p. 165.
37. L. J. Battan, Radar Observation of the Atmosphere, The University of Chicago Press, Chicago, 1973, p. 41.
38. C. C. Chen, "Attenuation of Electromagnetic Radiation by Haze, Fog, Clouds, and Rain," Report R-1694-PR, The Rand Corporation (April 1975), p. 5.
39. L. H. Battan, loc. cit., p. 86.
40. K. L. Gunn and J. S. Marshall, "The Distribution with Size of Aggregate Snowflakes," Journal of Meteorology, Volume 15 (1958), pp. 452-456.
41. S. Jacobs, M. Sargent, and M. Scully, High Energy Lasers and Their Applications, Addison Wesley Publishing Co., Reading Ma., 1974, pp. 181-182.
42. T. Chiba, "Spot Dancing of a Laser Beam Propagated through the Turbulent Atmosphere," Applied Optics, Volume 10 (November 1971) pp. 2456-2461.
43. S. Jacobs, M. Sargent, and M. Scully, loc. cit., p. 179.

## REFERENCES (Cont'd)

44. J. Davies, "Consideration of Atmospheric Turbulence in Laser Systems Design," Proceedings on the Conference of Atmospheric Limitations to Optical Propagation, NBS, Boulder, Colorado (March 1965).
45. J. Davies, loc. cit.
46. V. I. Tatarski, Wave Propagation in a Turbulent Medium, McGraw-Hill Book Company, Inc., New York, 1961.
47. V. I. Tatarski, loc. cit.
48. J. Davies, loc. cit.
49. T. S. Fahlen, "CO<sub>2</sub> Laser Design Procedure," Applied Optics, Volume 12 (October 1973), pp. 2381-2390.
50. L. D. Dickson, "Characteristics of a Propagating Gaussian Beam," Applied Optics, Volume 9 (August 1970), pp. 1854-1861.
51. A. F. Harvey, Coherent Light, John Wesley & Sons, Ltd., London, 1970, p. 150.
52. J. H. McCoy, Atmospheric Absorption of Carbon Dioxide Laser Radiation Near 10 Microns, Report 2476-2, 10 September 1968, Electroscience Laboratory, Ohio State University, p. 104.
53. P. Chylek, "Extinction and Liquid Water Content of Fogs and Clouds," Journal of the Atmospheric Sciences, Volume 35 (February 1978), Volume 35 (February 1978), pp. 296-300.
54. C. C. Chen, loc. cit.
55. D. Rensch and R. K. Long, loc. cit.
56. C. C. Chen, A Correction for Middleton's Visible and Infrared Radiation Extinction Coefficients Due to Rain, Report R-1523-PR, The Rand Corporation, August 1974, pp. 5-8.
57. C. E. Junge, loc. cit.
58. F. E. Volz, "Infrared Refractive Index of Atmospheric Aerosol Substances," Applied Optics, Volume 11, No. 4 (April 1972), p. 756.